2014

bio-inspired attitude control of micro air vehicles using rich information from airflow sensors

He Shen
University of Central Florida

BIO-INSPIRED ATTITUDE CONTROL OF MICRO AIR VEHICLES USING RICH INFORMATION FROM AIRFLOW SENSORS

by

HE SHEN
B.S. Northwestern Polytechnical University, China, 2008
M.S. Northwestern Polytechnical University, China, 2010
M.S. University of Central Florida, USA, 2013

A dissertation submitted in partial fulfillment of the requirements
for the degree of Doctor of Philosophy
in the Department of Mechanical & Aerospace Engineering
in the College of Engineering & Computer Science
at the University of Central Florida
Orlando, Florida

Spring Term
2014

Major Professor: Yunjun Xu

ABSTRACT

Biological phenomena found in nature can be learned and customized to obtain innovative engineering solutions. In recent years, biologists found that birds and bats use their mechanoreceptors to sense the airflow information and use this information directly to achieve their agile flight performance. Inspired by this phenomenon, an attitude control system for micro air vehicles using rich amount of airflow sensor information is proposed, designed and tested. The dissertation discusses our research findings on this topic. First, we quantified the errors between the calculated and measured lift and moment profiles using a limited number of micro pressure sensors over a straight wing. Then, we designed a robust pitching controller using 20 micro pressure sensors and tested the closed-loop performance in a simulated environment. Additionally, a straight wing was designed for the pressure sensor based pitching control with twelve pressure sensors, which was then tested in our low-speed wind tunnel. The closed-loop pitching control system can track the commanded angle of attack with a rising time around two seconds and an overshoot around 10%. Third, we extended the idea to the three-axis attitude control scenarios, where both of the pressure and shear stress information are considered in the simulation. Finally, a fault tolerant controller with a guaranteed asymptotically stability is proposed to deal with sensor failures and calculation errors. The results show that the proposed fault tolerant controller is robust, adaptive, and can guarantee an asymptotically stable performance even in case that 50% of the airflow sensors fail in flight.

ACKNOWLEDGMENTS

First of all, I would like to thank my advisor Dr. Yunjun Xu for his academic insight, and continuous support of my doctoral research and study. Without his wise guidance, I could not have finished my dissertation. I would also like to thank the rest of my committee members: Dr. Kuo-chi Lin, Dr. Jeffrey Kauffman, and Dr. Linan An for their insightful comments on my research and valuable suggestions on my future career. I would also like give special thanks to Dr. Chengying Xu at Florida State University for her suggestions during my candidacy exam.

I dedicate this dissertation to my family, thanks for their immense love and encouragement in my whole life. Special thanks are given to my sister for her caring of our parents during the time I am not around. I also would like to give my special thanks to my wife Ni Li, for her tremendous love, support and encouragement in the past five years. My life is fulfilled with happiness with her around every day.

Finally, I also want to thank my labmates: Charles Remeikas, Brad Sease, Kenneth Thompson, Pradens Pierre-Louis, Puneet Vishwakarma, Jacob Belli, and Robert Sivilli, for their helps on my research. Thanks are also given to the undergraduate students who have worked with me during their senior designs. I also would like to give my appreciation to the closest friends, Jinling Liu, Dan Chen, Yaohan Chen, Xueping Yang, for their encouragement.

TABLE OF CONTENTS

LIST OF FIGURES

LIST OF TABLES

CHAPTER ONE: INTRODUCTION

Background

Micro Air Vehicles (MAVs) are small, lightweight flying robots that operate at low speeds and low Reynolds numbers. In particular, they usually have wing spans of less than 15 cm, weigh less than 100 grams, and fly a speed of less than 25 m/s [1]. They are suitable for applications such as information collection, object detection, cave exploring, and boarder surveillance, especially when the environments are either hazardous for human or inaccessible for larger flying vehicles [1, 2]. Typical applications for these MAVs include border surveillance [3], power-line inspection [4], home security [5] , and serving as a temporary antenna [6].

However, due to the significant size reduction, low aspect ratio, and low flight speed, it is challenging for MAVs to fly autonomously while maintaining satisfactory stability and maneuverability. The challenges come from the both the design and control. From the system design perspective, the challenges mainly come from hardware system miniaturization under the constraints of volume, weight and power requirements. From the flight control perspective, the challenges mainly come from the following four aspects. First, many of the current MAVs are designed with unconventional configurations [7], while the flight control system designers haven't taken this change into consideration. Customized flight control methods for uncongenially designed MAVs are still lacking. Second, they operate in a very low and sensitive Reynolds number regime (normally below 100,000), where aerodynamics are not well understood yet [8]. Third, because of their small moment of inertia, MAVs are very sensitive to flow disturbances [9]. Fourth, theories for dynamic modeling of MAVs are not natural, since

many assumptions used in analyzing larger aerial vehicles, such as inviscid fluid, can no longer be used in analyzing MAVs [10]. Finally, the ability to predict the flow field precisely in low Reynolds number flight is still lacking [8].

Motivation

Compared with existing MAVs, birds and bats can achieve remarkable flight performances in terms of stability, maneuverability, and energy efficiency. For examples, a wandering albatross can fly for hours or even days without flapping its wings [11]; a barn swallow can achieve a roll rate higher than 5,000 degrees per second [11]; and bats can reverse their flight directions at a full speed in a distance less than half of its wingspan [12]. So, it is necessary to study how birds and bats cope with the complex flow and benefit our MAVs' design and flight control.

It has been shown that all these outstanding flying characteristics are due to the fact that birds and bats can effectively interact with their surrounding flow environments. Birds exploit the pressure and shear information using mechanoreceptors on or around follicles to deal with complex flow to achieve thermal soaring, ridge soaring, and formation flying [13][14]. Bats use mechanoreceptors to fly with high maneuverability [15]. There is another study shows that eagles can feel even the smallest changes in the air pressure to help them cope with the changing weather and seasons [16]. This remarkable sensing capability, i.e. measuring not only rigid body motion but also flow information, assists birds in performing their skillful and graceful maneuvers, which is not seen in today's MAVs.

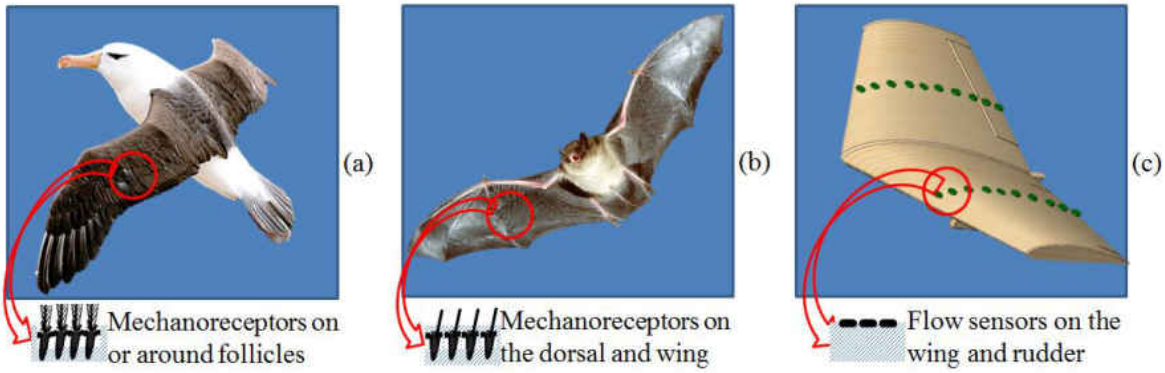

Figure 1 Bio-inspired flight control mechanism for an MAV

Inspired by these phenomena observed in nature, an MAV attitude control system using the real-time flow information is proposed. Figure 1 shows the similarities of the proposed flight control method and that of birds and bats. Different from the traditional designs, this MAV has numerous air flow sensors (which can measure the real-time pressure and shear information) all over its surfaces. These sensors enable the MAV to have the capability of detecting the flow information and provide additional information for flight control. The new design is expected to help MAVs to achieve more stable, maneuverable and energy efficient flight.

Literature Reviews

Since the 1990s, MAV-related research has become a very hot topic. From the design perspective, the flying wing configuration is adopted by more and more MAVs, since this configuration has lower interference drag but wider dynamic range compared to the wing-fuselage configuration [3]. Successful examples include the Black Widow [17], MicroSTAR [18], Trochoid, MicroDot [19], MITE series [20], HOMA [21], etc.

From the major sensing device perspective, vision based systems are widely used as the primary sensing and navigation devices in MAVs [22-24] because of their low cost, light weight,

and capability of detecting their surrounding environment [25]. However, the limited vision range under unpredictable weather conditions, such as fog or clouds, and the high computational cost associated with vision/video processing algorithms makes it challenging to achieve agile motion. Other devices such as inertial measurement unit (IMU) [26, 27], infrared sensors [28], and GPS [29] have also been used to provide rigid body motion information of aircraft. Another innovative design is based on the principle of blackbody radiation [30], in which MAVs can sense the difference between the heat radiated from the ground and the sky, to find the horizon line. This design is fairly simple and cost effective, yet the true horizon can be obscured by other blackbody objects, such as high rise buildings or mountains.

Form the aerodynamic modeling and control perspectives, the methods used for MAVs are more or less from those for bigger airplanes. The aerodynamic models developed with the attitude information usually use the moment coefficients to indirectly describe the aerodynamic moment, which is not accurate enough in the complex wind conditions. However, many of the theories for bigger airplanes cannot be applied to MAVs directly.

Up to now, there has some researches done using flow information for other purposes. There has been research conducted in using either pressure or shear sensors to measure the angle of attack and leading edge flow separations for large size unmanned aerial vehicles [31-33]. The flow information has also been used in large aerial vehicles' health monitoring systems [34]. In [35], the pressure information measured at a few carefully selected locations on a model aircraft is used for controlling the lift distribution; while in [36] hair sensors are used to help the vision system to measure the velocity information of the MAV.

Methodology

It's well understood that the aerodynamic performance of MAVs is determined by the pressure acting on their surfaces [37]. However, to date, pressure information has not been widely used in flight control of MAVs. Taking a cue from the phenomenon observed in biological systems, a pressure and shear information based attitude control method is proposed for MAVs. Like the mechanoreceptors or follicle systems found in birds, micro pressure sensors are embedded on the surfaces of the wing to measure the real-time flow information. The actual pressure profile will be obtained by interpolating the discrete pressure data measured from the sensor array. With the flow information obtained, the aerodynamic forces and moments acting on the MAVs can be roughly calculated, which potentially provides more information for better attitude control performance.

CHAPTER TWO: PITCHING CONTROL

This chapter will discuss the pitching control using pressure information and the majority of the content of this chapter is based on my paper [50]. The contributions of this chapter are: (1) a new mathematical model that captures the relationships between the pressure profile, the control surface deflection, and the flight state is derived with shear stress, skin friction drag, and wingtip vortex effect regarded as un-modeled dynamics or uncertainties in the controller design; (2) compared to the rigid body motion sensors, the actual flow information will be directly measured and used for control; and (3) some practical issues in incorporating micro pressure sensors on the MAV wing surfaces are discussed.

The rest of this chapter is organized as follows: Firstly, the pressure sensor distribution and the aerodynamic force calculations are given. Secondly, a new pure pitch motion governing equation is derived, based on which a nonlinear robust controller is designed using the pressure profile. Finally, wind tunnel experiments are conducted to validate the lift calculation, and the pitch control of the MAV using the pressure information is demonstrated through simulation.

Pressure Driven Aerodynamics

To capture the real-time flow information, an array of micro pressure sensors is placed on both the upper and the lower surfaces of the MAV wing. The following four criteria are considered in the layout design of the sensors via a trial and error approach: (1) the error between the actual force and the one calculated through the curve-fitted pressure profile using the discrete pressure information should be small; (2) the location where a sensor can be placed should be accessible; (3) the size, weight, power consumption, and number of cables required of the

sensors need to be small; and (4) the structural integrity of the wing surface should not be affected by the embedded pressure sensors and the drag should not be noticeably increased. The detailed information about the layout of the pressure sensors is shown in the "Wind Tunnel Experiment and Simulation Results" section.

The micro pressure sensor used in the current design is shown in Figure 2.

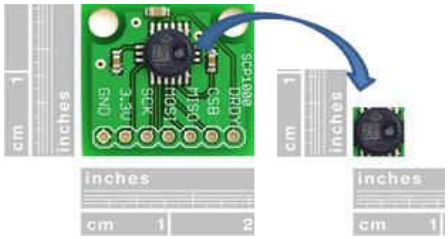

Features:

- **Measuring range: 30-120 kPa**
- Resolution: 1.5 Pa
- Size: Diameter 6.1 mm, Height 1.7 mm
- Weight: 0.4 g (2 g with the breakout board)
- Power: 2.7V, <10μA

Figure 2 Pressure sensor SCP1000 and the breakout board

Based on numerous tests of these sensors under a static wind condition, it is found that the sensor readings are stable but with small bias errors. The following equation is used to correct the bias of the raw pressure data

$$\hat{p}_i(\alpha,\delta_e,V_\infty) = p_i^r(\alpha,\delta_e,V_\infty) + p_i^c,\ i=1,2,\cdots,n \tag{1}$$

where $\hat{p}_i$ is the pressure data from the i^{th} sensor with the bias error corrected, p_i^r is the raw pressure data directly measured from the i^{th} sensor, and p_i^c is the constant bias associated with the i^{th} sensor. n is the number of pressure sensors embedded on the wing surfaces. Both $\hat{p}_i$ and p_i^r are functions of the angle of attack α, elevon deflection angle δ_e, and free stream speed V_∞.

The constant bias of the pressure p_i^c can be found by calculating the difference between the measurements under static wind conditions of sensor i and the average of that from all the

sensors, which can be expressed as

$$p_i^c = \bar{p}^s - p_i^s, \ i = 1, 2, \cdots, n \tag{2}$$

where p_i^s is the raw measurement under the static wind condition, and $\bar{p}^s$ is the average of the raw measurements under the static wind condition and calculated by

$$\bar{p}^s = \frac{1}{n} \sum_{i=1}^{n} p_i^s \tag{3}$$

In order to get more accurate pressure data p_i and reduce the noise associated with the bias-corrected pressure data $\hat{p}_i$, a moving average filter is applied as

$$p_i(k) = \frac{1}{m} \sum_{j=0}^{m-1} \hat{p}_i(k-j), \quad i = 1, 2, \cdots, n \tag{4}$$

where $p_i(k)$ is the filtered pressure data for the i^{th} sensor at time k, and m is the width of the filter. To calculate the aerodynamic force, moment, and center of pressure, the monotone piecewise cubic interpolation method [38] is applied to generate the pressure profiles on wing surfaces, p_u and p_l, using the discrete pressure data p_i, $i = 1, 2, ..., n$.

Figure 3 shows the schematic of a wing, in which L, D, and T are the lift, drag, and thrust, respectively. α is the angle of attack, δ_e is the angle of the elevon, c is the chord length, and b is the wing span. “LE”, “TE”, “CP”, and “CG” are the abbreviations for the leading edge, trailing edge, center of pressure, and center of gravity, respectively.

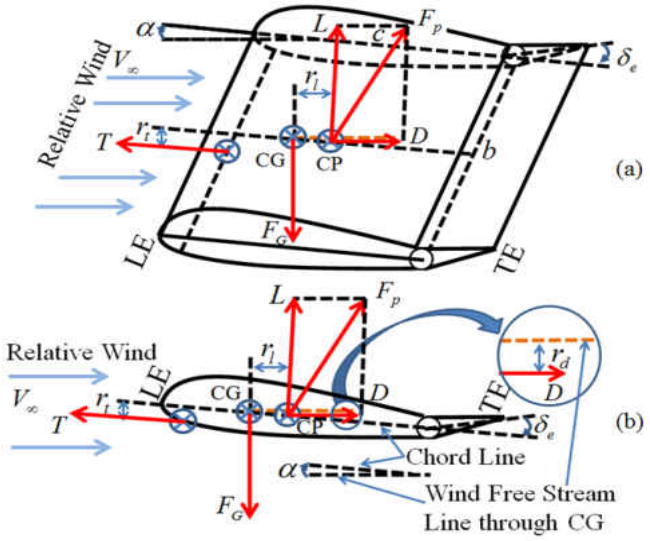

Figure 3 Aerodynamic forces on a MAV wing: (a) 3D view and (b) side view

The pressure distribution on an airfoil is sketched in Figure 4. For a typical wing, the normal pressure is significantly larger than the shear by at least two orders of magnitude [39]. Therefore the pressure force per unit span f_p is nearly perpendicular to the surface, and can be approximated by

$$f_p = \int_{LE}^{TE} p_l ds_l - \int_{LE}^{TE} p_u ds_u \approx \int_0^c (p_l - p_u) dx \tag{5}$$

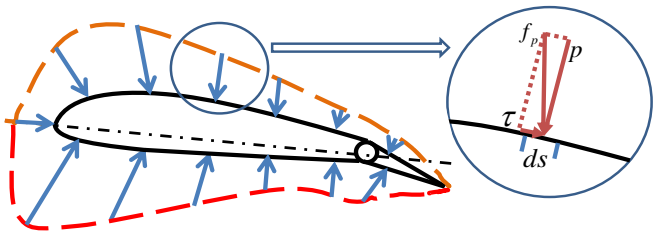

Figure 4 Pressure distribution on an airfoil with the elevon deflected

In reality, the pressure distribution near the wing tips will be different from that of the middle section; however, for simplicity, the wingtip vortex effect on the pressure distribution is regarded as un-modeled dynamics. Therefore it is assumed that the pressure is uniformly

distributed along the *y* axis, and the total pressure force F_p can be approximated by integrating the normal pressure over the wing surface as

$$F_p = \int_0^b \int_0^c \left(p_l - p_u \right) dxdy \triangleq \int_0^b \int_0^c p\left(\alpha, \delta_e, V_\infty, x\right) dxdy \tag{6}$$

Separating the total pressure force on the vertical and horizontal directions, the lift and form drag can be calculated as

$$L = F_p \cos\alpha \tag{7}$$

and

$$D = F_p \sin\alpha \tag{8}$$

Compared to the form drag, the drag due to the skin friction is relatively small [40] and will be regarded as un-modeled dynamics to be considered in the nonlinear robust controller design section. For the constant speed level flight considered in this paper, the thrust can be approximated as $T \approx D$, and the pitching moment about the center of gravity is therefore governed by

$$M_p = Tr_t - Lr_l - Dr_d \tag{9}$$

in which r_t, r_l, and r_d are the corresponding arms of the moments for the thrust, lift, and drag, respectively. r_l is the difference between the center of pressure and the center of gravity, which can be calculated as

$$r_l = x_{cg} - x_{cp} = x_{cg} - \int_0^c xp\left(x\right) dx \Big/ \int_0^c p\left(x\right) dx \tag{10}$$

Modeling and Control

As shown in Figure 3, in constant speed level flight, the governing equation of the pure pitch motion of the MAV is

$$J\ddot{\alpha} = M_p\left(\alpha, \delta_e\right) \tag{11}$$

in which J is the moment of inertia about the y axis. The moment M_p is a function of the pressure distribution, the angle of attack, and the deflection of the elevon. As can be seen in Eq. (11), such a model is not a control affine.

Combing Eqs. (6)-(11), the following equation is obtained to describe the pure pitch motion of the MAV, in which $C\left(x,\alpha\right) \triangleq \left(r_t - r_d\right)\sin\alpha + \left(x - x_{cg}\right)\cos\alpha$.

$$\begin{aligned}
J\ddot{\alpha} &= M_p\left(\alpha,\delta_e\right) = Tr_t - Lr_l - Dr_d \approx D\left(r_t - r_d\right) - Lr_l \\
&\approx F_p\left[\left(r_t - r_d\right)\sin\alpha - \left(x_{cg} - x_{cp}\right)\cos\alpha\right] \\
&= \int_0^b\int_0^c p\left(\alpha,\delta_e,x\right)dxdy\left[\left(r_t - r_d\right)\sin\alpha - \left(x_{cg} - x_{cp}\right)\cos\alpha\right] \\
&= \int_0^b\int_0^c p\left(\alpha,\delta_e,x\right)dxdy\begin{bmatrix}\left(r_t - r_d\right)\sin\alpha - x_{cg}\cos\alpha \\ +\cos\alpha\int_0^c xp\left(\alpha,\delta_e,x\right)dx \Big/ \int_0^c p\left(\alpha,\delta_e,x\right)dx\end{bmatrix} \\
&= \int_0^b\int_0^c\left[\left(r_t - r_d\right)\sin\alpha + \left(x - x_{cg}\right)\cos\alpha\right]p\left(\alpha,\delta_e,x\right)dxdy \\
&\triangleq \int_0^b\int_0^c C\left(x,\alpha\right)p\left(\alpha,\delta_e,x\right)dxdy
\end{aligned} \tag{12}$$

According to the small perturbation theory [41], if the difference between the actual and the trimmed deflection of the elevon is small, the pressure distribution in Eq. (12) can be approximated as

$$p\left(\alpha,\delta_e,x\right) \approx \bar{p}\left(\alpha,\delta_{e_{trim}},x\right) + p^{\delta_e}\Delta\delta_e \tag{13}$$

in which $\delta_{e_{trim}}$ is the deflection angle of the elevon at the trim condition, and p^{δ_e} can be regarded as the pressure derivative of the elevon around $\delta_{e_{trim}}$. $\bar{p}\left(\alpha,\delta_{e_{trim}},x\right)$ is the pressure information at the trim condition for a particular angle of attack.

Let us define

$$M_p\left(\alpha,\delta_{e_{trim}}\right)\triangleq\int_0^b\int_0^c C\left(x,\alpha\right)\bar{p}\left(\alpha,\delta_{e_{trim}},x\right)dxdy \tag{14}$$

and

$$M_p^{\delta_e}\left(\alpha,\delta_e\right)\triangleq\int_0^b\int_0^c C\left(x,\alpha\right)p^{\delta_e}dxdy \tag{15}$$

The control affine model is derived as

$$J\ddot{\alpha}=M_p\left(\alpha,\delta_{e_{trim}}\right)+M_p^{\delta_e}\left(\alpha,\delta_e\right)\Delta\delta_e \tag{16}$$

It is worth noting that the actual control variable is calculated as

$$\delta_e=\delta_{e_{trim}}+\Delta\delta_e \tag{17}$$

$\delta_{e_{trim}}$ cannot be calculated using the real-time pressure information. Therefore the following nominal model will be used in the control design:

$$J\ddot{\hat{\alpha}}=\hat{M}_p\left(\alpha,\delta_e\right)+\hat{M}_p^{\delta_e}\left(\alpha,\delta_e\right)\Delta\hat{\delta}_e \tag{18}$$

where the "caret" denotes the nominal value.

To achieve the affine nominal model as described in Eq. (18), several approximations have been applied and the mismatches between the actual dynamics and the nominal model are regarded as un-modeled dynamics. The un-modeled dynamics include: (1) the wingtip vortex effect on the pressure distribution, (2) the shear stress that is significantly less than the normal pressure, and (3) the drag component that is due to the skin friction. All of these effects are

neglected in the nominal model. It is worth noting that these effects are not explicitly shown in the nominal model for the controller design purpose; however, they do exist in the actual MAV plant, and the differences between the actual model and the nominal model are captured by the uncertainty bounds. The bounded uncertainties exist in the following quantities: the time variations in r_t and r_d, noise in the pressure measurements, and noise in the angle of attack measurements.

Let us define

$$f \triangleq M_p\left(\alpha, \delta_{e_{trim}}\right)/J \tag{19}$$

$$g \triangleq M_p^{\delta_e}\left(\alpha, \delta_{e_{trim}}\right)/J \tag{20}$$

$$\hat{f} \triangleq \hat{M}_p\left(\alpha, \delta_e\right)/J \tag{21}$$

and

$$\hat{g} \triangleq \hat{M}_p^{\delta_e}\left(\alpha, \delta_e\right)/J \tag{22}$$

The system in Eq. (16) can be rewritten as

$$\ddot{\alpha} = f + g\Delta\delta_e \tag{23}$$

and the nominal model in Eq. (18) can be written as

$$\ddot{\hat{\alpha}} = \hat{f} + \hat{g}\Delta\delta_e \tag{24}$$

A chattering mitigated nonlinear robust controller (CMC) [42] is customized here for the pressure information based pure pitch control. Different from approaches in [43-46], the CMC controller is designed to be

$$\Delta\delta_e = \hat{g}^{-1}\left[-\hat{f} + \ddot{\alpha}_d - k\lambda\tilde{\alpha} - (\lambda + k)\dot{\tilde{\alpha}}\right] \tag{25}$$

in which α_d is the desired angle of attack and $\tilde{\alpha}$ is the tracking error

$$\tilde{\alpha} = \alpha - \alpha_d \tag{26}$$

For the closed-loop system to be asymptotically stable, the control gain k should satisfy

$$\begin{cases} F + G\left|\ddot{\alpha}_d - \lambda\dot{\tilde{\alpha}} - \hat{f}\right| + \eta s = \quad ks - G|ks| & s > 0 \\ F + G\left|\ddot{\alpha}_d - \lambda\dot{\tilde{\alpha}} - \hat{f}\right| - \eta s = -ks - G|ks| & s < 0 \end{cases} \tag{27}$$

where s is defined to be $s = (d/dt + \lambda)\tilde{\alpha}$. When $s = 0$, ks will be solved together to avoid the singularity issue. Here λ and η are positive real values. F and G are the bounds associated with the un-modeled dynamics and uncertainties described before, in which

$$\left|\hat{f} - f\right| \le F \tag{28}$$

and

$$g = (1 + g^*)\hat{g},\ \left|g^*\right| \le G \le 1 \tag{29}$$

Since the analytical descriptions of the bounds F and G, and the nominal value $\hat{g}$ in Eqs. (28) and (29) cannot be easily derived, the Monte Carlo simulation method (500 runs) is used instead to find these values, as is illustrated in Figure 5. In the simulation, the angle of attack α and the elevon deflection δ_e are randomly chosen from the following ranges $\alpha \in [5^o, 15^o]$ and $\delta_e \in [-25^o, 25^o]$. Figure 5(a) shows that bound F can be found by dividing the maximum difference between the moments calculated at $(\alpha, \delta_{e_{trim}})$ and (α, δ_e) by the moment of inertia J. Bound G and nominal value $\hat{g}$ are calculated using the procedures illustrated in

Figure 5(b) and Figure 5(c). In every Monte Carlo simulation run, four moments- $M_p^{(1)}$, $M_p^{(2)}$, $\hat{M}_p^{(1)}$, and $\hat{M}_p^{(2)}$- are calculated at $(\alpha, \delta_{e_{trim}})$, $(\alpha, \delta_{e_{trim}} + \delta_\varepsilon)$, (α, δ_e) and $(\alpha, \delta_e + \delta_\varepsilon)$, respectively, in which δ_ε is the small variation of the elevon deflection. g^* and $\hat{g}^*$ can be calculated using $g^* = (M_p^{(2)} - M_p^{(1)})/(J\delta_\varepsilon)$ and $\hat{g}^* = (\hat{M}_p^{(2)} - \hat{M}_p^{(1)})/(J\delta_\varepsilon)$, respectively. Finally, $\hat{g}$ is found by calculating the mean value of $\hat{g}^*$ from the 500 Monte Carlo simulation runs, and bound G is obtained by calculating the maximum absolute value of the differences between $g^*/\hat{g}^*$ and one.

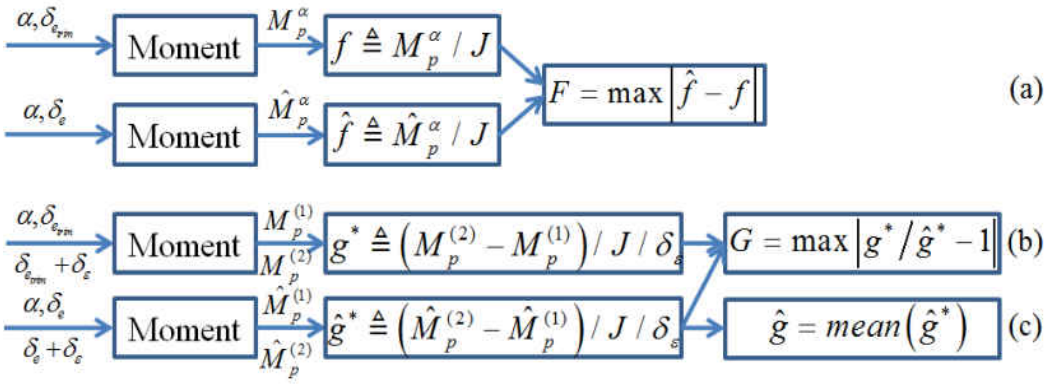

Figure 5 Parameters' calculation: (a) Bound F, (b) Bound G, and (c) input coefficient $\hat{g}$

Lemma 1. The closed-loop system defined in Eq. (23) is asymptotically stable if the controller is designed based on Eq. (25). The proof of Lemma 1 shown below is customized from [42].

Proof. Let us define the sliding surface to be $s = (d/dt + \lambda)\tilde{\alpha}$, in which $\lambda > 0$ and $\tilde{\alpha} = \alpha - \alpha_d$. The Lyapunov function is $V = s^2/2$, and the derivative of the Lyapunov function is

$$
\begin{aligned}
s\dot{s} &= s\left(\ddot{\tilde{\alpha}} + \lambda\dot{\tilde{\alpha}}\right) = \left(f + g\Delta\delta_e - \ddot{\alpha}_d + \lambda\dot{\tilde{\alpha}}\right)s \\
&= \left(f + g\hat{g}^{-1}\left[-\hat{f} + \ddot{\alpha}_d - k\lambda\tilde{\alpha} - (\lambda + k)\dot{\tilde{\alpha}}\right] - \ddot{\alpha}_d + \lambda\dot{\tilde{\alpha}}\right)s \\
&= \left(f + (1 + g^*)\left[-\hat{f} + \ddot{\alpha}_d - \lambda\dot{\tilde{\alpha}} - ks\right] - \ddot{\alpha}_d + \lambda\dot{\tilde{\alpha}}\right)s \\
&= \left\{f - \hat{f} - ks + g^*\left[-\hat{f} + \ddot{\alpha}_d - \lambda\dot{\tilde{\alpha}} - ks\right]\right\}s
\end{aligned}
\tag{30}
$$

It is worth noting that the control gain k is assumed to be positive. If $s(t) > 0$, Eq. (30) becomes

$$
\begin{aligned}
s\dot{s} &= \left\{f - \hat{f} - ks + g^*\left[-\hat{f} + \ddot{\alpha}_d - \lambda\dot{\tilde{\alpha}} - ks\right]\right\}s \\
&\le \left\{F + G\left|-\hat{f} + \ddot{\alpha}_d - \lambda\dot{\tilde{\alpha}}\right| - g^*ks - ks\right\}s \\
&\le \left\{F + G\left|-\hat{f} + \ddot{\alpha}_d - \lambda\dot{\tilde{\alpha}}\right| + Gks - ks\right\}s \triangleq -\eta s^2 < 0
\end{aligned}
\tag{31}
$$

Here $\eta > 0$. If $s(t) < 0$, Eq. (30) can be written as

$$
\begin{aligned}
s\dot{s} &= \left\{f - \hat{f} - ks + g^*\left[-\hat{f} + \ddot{\alpha}_d - \lambda\dot{\tilde{\alpha}} - ks\right]\right\}s \\
&\le \left\{-F + g^*\left[-\hat{f} + \ddot{\alpha}_d - \lambda\dot{\tilde{\alpha}}\right] - g^*ks - ks\right\}s \\
&\le \left\{-F - G\left|-\hat{f} + \ddot{\alpha}_d - \lambda\dot{\tilde{\alpha}}\right| - (1 + g^*)ks\right\}s \\
&\le \left\{-F - G\left|-\hat{f} + \ddot{\alpha}_d - \lambda\dot{\tilde{\alpha}}\right| - (1 + G)|ks|\right\}s \triangleq -\eta s^2
\end{aligned}
\tag{32}
$$

If $s(t) = 0$, then $V = 0$, $\dot{V} = 0$, and the Barbalat's Lemma [47] can be used to prove that $\dot{V}(x,t) \to 0$ as $t \to \infty$. Therefore, based on Eq. (31) and Eq. (32), the controlled system is asymptotically stable. The control gain can be calculated using Eq. (31) and Eq. (32) as

$$
\begin{cases}
F + G\left|\ddot{\alpha}_d - \lambda\dot{\tilde{\alpha}} - \hat{f}\right| + \eta s = \ ks - G|ks| & s > 0 \\
F + G\left|\ddot{\alpha}_d - \lambda\dot{\tilde{\alpha}} - \hat{f}\right| - \eta s = -ks - G|ks| & s < 0
\end{cases}
\tag{33}
$$

Since $G < 1$, the control gain k is positive.

Experiment and Simulation

The accuracy of the aerodynamic forces calculated using the data from a limited number of pressure data is validated in wind tunnel experiments. The capability of the low speed wind tunnel facility restricts the measurement to lift only, which is then compared to the calculated results.

Constrained by the size of the wind tunnel, a flying wing with nine sensors is used in the testing. The chord length of the wing is 14.7 cm and the wing span is 28.25 cm. The airfoil section along the wing span direction is uniform, and the whole wing is mounted on a force gauge inside of the low speed wind tunnel. The locations of the sensors are given in Figure 6 and Table 1. In Figure 6, c, b, and t are the chord length, wing span and thickness of the airfoil, respectively; the sensors are denoted by the small circles (on the upper surface) and squares (on the lower surface), and are carefully aligned with the wing surface. The sensor location (x, y) is measured from the leading edge and the right wing tip. In Table 1, the chord-wise location is given in a ratio between the distance of the sensor location measured from the leading edge and the chord length; the span-wise location is also given in a ratio between the distance of the sensor location measured from the right wing tip and the wing span. For example, sensor 1 is located at a distance of 73.4% of the chord length measured from the leading edge and 26.5% of the span measured from the right wing tip.

Table 1 Sensor locations on the wing surfaces

Sensor	1	2	3	4	5	6	7	8	9
x/c	73.4%	37.8%	29.2%	16.2%	10.8%	6.5%	16.2%	52.9%	73.4%
y/b	26.5%	36.6%	56.5%	76.5%	86.4%	66.5%	76.5%	66.5%	46.7%

As shown in Figure 7, the wing is mounted on a single strut force gauge in the center of an open circuit suction type low speed wind tunnel. A strut is attached to the wing with a bracket that could be adjusted to change the angle of attack. The angle of attack is recorded from the protractor, which is mounted on one side of the wind tunnel walls, and the wind speed is measured using a pitot static tube.

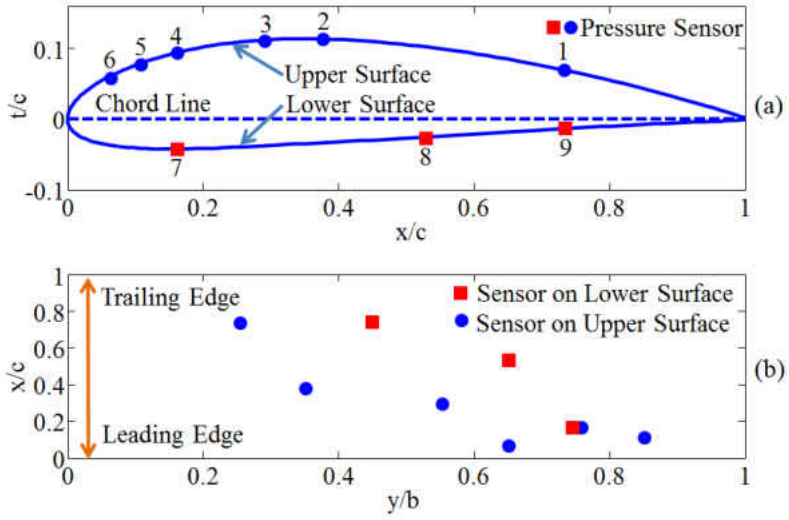

Figure 6 Sensor locations: (a) side view and (b) top view

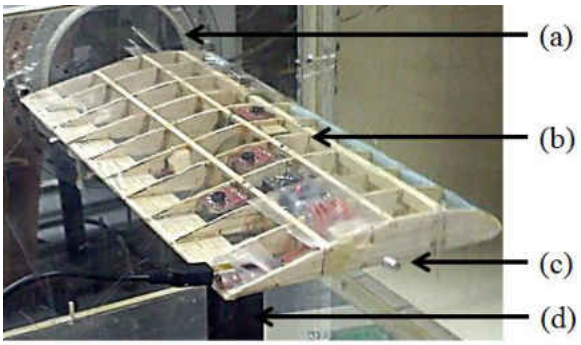

Figure 7 Wind tunnel setup: (a) protractor, (b) wing, (c) pitot tube, and (d) force gauge

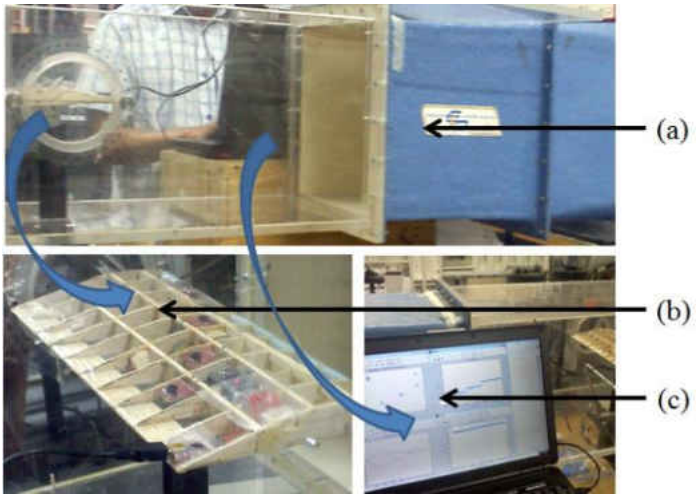

Figure 8 Wind tunnel test facility: (a) wind tunnel, (b) wing, and (c) software

Figure 8 shows the scenario in which the real-time pressure data is collected and processed. An Arduino microcontroller (ATMEGA168) is used to collect the pressure data from the sensor array, and then send the data to a laptop through a serial port. Software is designed in MATLAB to communicate with the hardware.

Numerous wind tunnel tests are conducted and five of them are shown in Figure 9 and Table 2. The measurements from the force gauge L_m and the ones calculated using the sensor

array data L_c match well with an error range from 0.3% to 9%. Here, L_c is computed using the lift calculation in Eq. (7). It is worth noting that if more sensors are placed on the surfaces of the wing, more accurate results can be achieved.

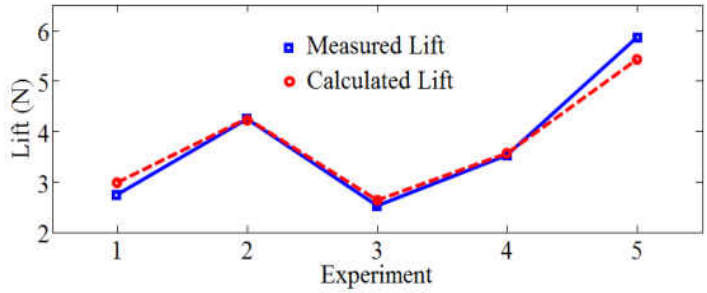

Figure 9 Wind tunnel experiment validation

Table 2 Wind tunnel test results

Test	α (°)	V_∞ (m/s)	Re	L_m (N)	L_c (N)	Error
1	5	8.14	79089.8	2.73939	2.98573	8.9%
2	5	10.17	98862.3	4.23816	4.24993	0.3%
3	10	6.43	62526.0	2.51735	2.63743	4.7%
4	10	7.33	71290.6	3.51653	3.55533	1.1%
5	10	10.37	100820	5.84795	5.41363	7.4%

The effectiveness of the proposed pressure information based pitch control concept is tested in a simulation environment and the control architecture is illustrated in Figure 10. An interface between the XFOIL® [48] and the MATLAB® software is developed to simulate the measurements obtained using the embedded sensor array. The theoretical pressure distribution can be generated using the XFOIL® according to the wind speed, angle of attack, and deflection of elevon. The discrete pressure data is simulated by adding noise to the pressure output of XFOIL® at the sensor locations according to the wind speed, angle of attack, and deflection of

the elevon. Then, these measurements will be interpolated to generate the pressure distribution, which is used by the controller. As mentioned previously, the wingtip vortex, shear, and drag due to the skin friction are not considered explicitly in the nominal model, but their effects are captured in the uncertainty bounds.

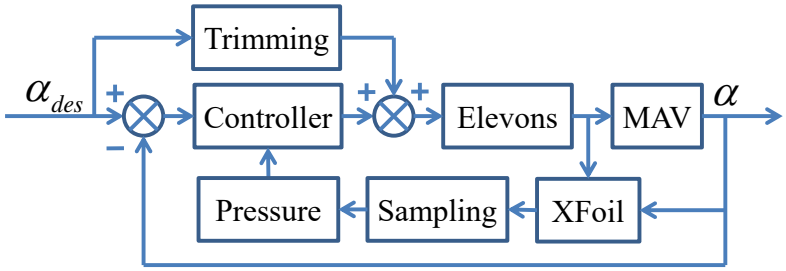

Figure 10 Pitch control simulation architecture

With a chord length of 14.70 cm and a wing span of 28.25 cm, the MAV wing used in simulation is same as the one described in the wind tunnel experiment section. Some additional parameters about the wing are shown in Table 3. Ten sensors are placed on each of the upper and lower surfaces of the wing, which are shown in

Table 4 and Figure 11. The notations used here are the same as those in Table 1 and Figure 6. x_e is the position of the elevon hinge position on the chord line.

Table 3 Configurations of the MAV used in simulation

Nomenclature	Value	Nomenclature	Value
J	$4.8\times10^{-3}\ kg\cdot m^2$	r_t	1.000 cm
x_{cg}	3.675 cm	r_d	0.500 cm
x_e	11.76 cm		

Table 4 Sensor locations on the simulated wing

Sensor	1	2	3	4	5	6	7	8	9	10
x/c	98%	90%	82%	78%	68%	50%	30%	10%	5%	2%
Sensor	11	12	13	14	15	16	17	18	19	20
x/c	2%	5%	10%	30%	50%	68%	78%	82%	90%	98%

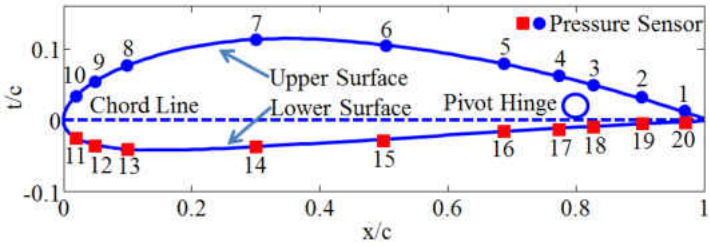

Figure 11 Sensor locations in the chord side view

Considering the capabilities of the selected sensors and other hardware devices, the sampling rate used in the simulation is set to be 20 Hz. It is worth noting that, the commercially available digital pressure sensor BMP 085 can operate at a frequency of 128 Hz [49]. Therefore in real implementation, a higher frequency can be chosen. It is assumed that the pressure sensor has a random noise with a zero mean and a standard deviation of 1.5 Pa, but truncated to be bounded within a [-4.5, 4.5] Pa range.

The nominal value $\hat{g}$ and the uncertainty bounds G and F are found from the Monte Carlo simulation. Figure 12 shows the randomly generated free stream wind speed (a Gaussian distribution with a mean value of 10.2 m/s and a standard deviation of 1.02 m/s), angle of attack (AOA: a uniform distribution within [5,15] degrees), and angle of elevon (AOE: a uniform distribution within [-25,25] degrees). Based on the 500 Monte Carlo runs, as are shown in Figure 13, $|\hat{f}-f|\le F=45$, $|g^*/\hat{g}^*-1|\le G=0.8$, and $\hat{g}=mean(\hat{g}^*)=-1$. However, to achieve a less

conservative design, two uncertainty bounds are further tuned to be $F = 1$ and $G = 0.2$.

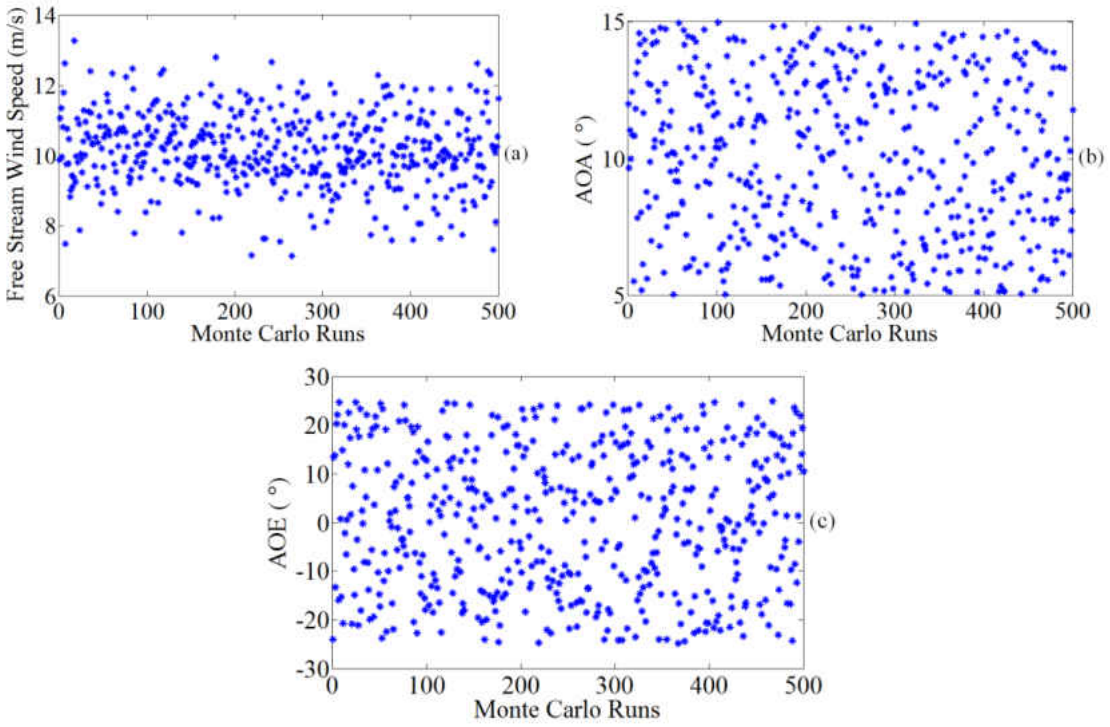

Figure 12 500 Monte Carlo runs: (a) free stream wind speed distribution, (b) angle of attack distribution, and (c) angle of elevon distribution

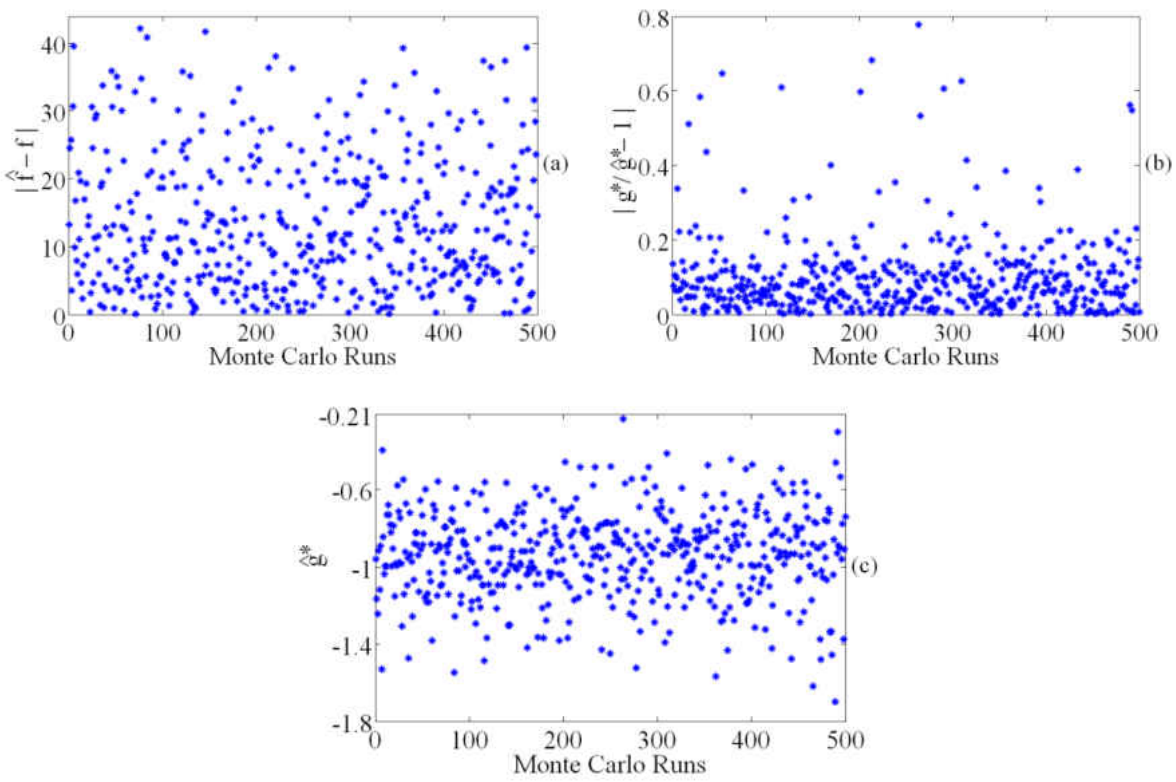

Figure 13 500 Monte Carlo runs: (a) $|\hat{f}-f|$, (b) $|g^*/\hat{g}^*-1|$, and (c) $\hat{g}^*$

The controller parameters are tuned to be $\lambda=\eta=3.2$. Figure 14 shows the closed-loop performances in Case I, where the angle of attack is commanded from 7o to 9o. The corresponding pressure distributions at the initial and steady state conditions are shown in Figure 15. The dotted line represents the result from XFOIL©, and the solid denotes the result from the simulated pressure sensor array. It can be seen from Figure 15 that, the pressure distribution only changes significantly around the leading edge and the elevon hinge. With proper sensor locations , the results calculated from the simulated 20 pressure sensors match very well with those calculated from XFOIL®.

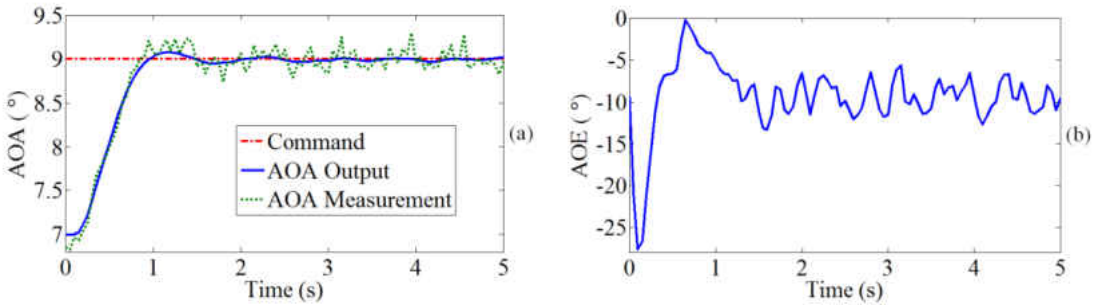

Figure 14 Simulation Case I: the angle of attack is commanded from 7° to 9°

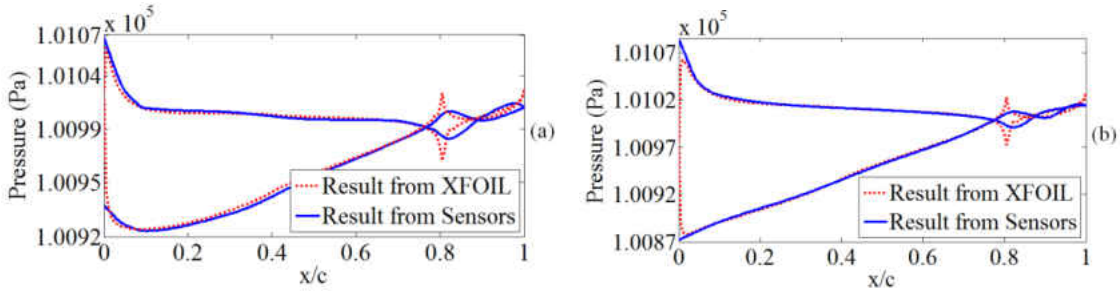

Figure 15 Pressure distribution in Case I when (a) $\alpha = 7^{\circ}$ and (b) $\alpha = 9^{\circ}$

The results of Case II, where the angle of attack is commanded from 10o to 6o, are shown in Figure 16 and Figure 17. Similar to Figure 15, Figure 17 shows the pressure distributions at the initial and steady state conditions.

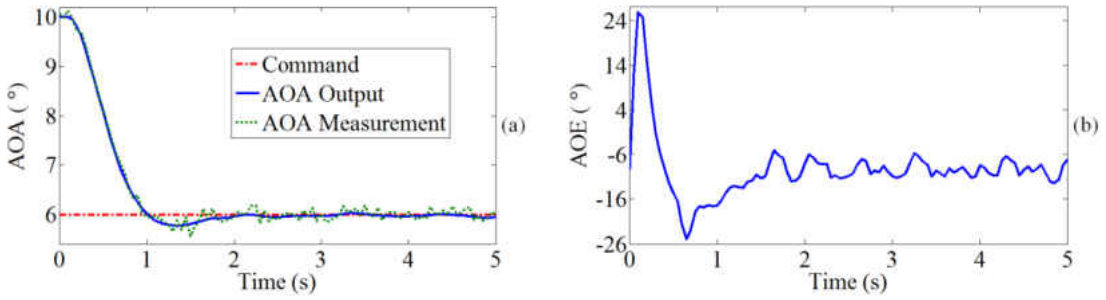

Figure 16 Simulation Case II: the angle of attack is commanded from 10° to 6°

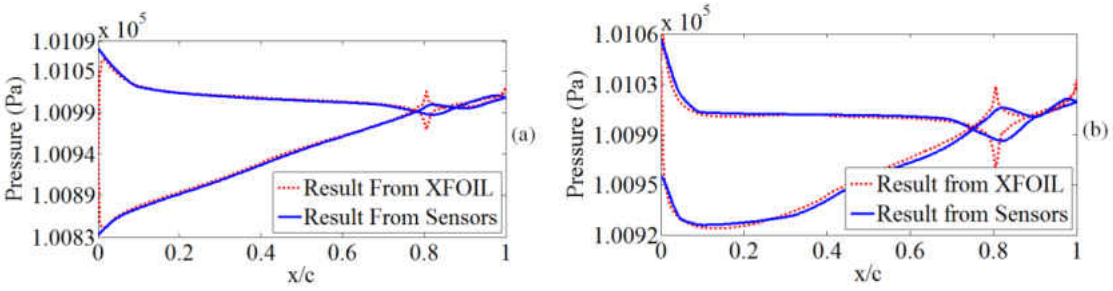

Figure 17 Pressure distribution in Case II when (a) $\alpha = 10^{\circ}$ and (b) $\alpha = 6^{\circ}$

In Case III, the angle of attack is controlled from 8o to 10o in a simulated unsteady flow environment. In this scenario, the wind speed is assumed to have a Gaussian distribution with a mean value of 10.2 m/s and a standard derivation of 1.02 m/s. The local flow separation is simulated by adding a Gaussian noise (a zero mean and a standard deviation of 30 Pa) to the pressure information measured on sensors 4-6. The noise associated with the pressure measurements from all the other sensors is assumed to be Gaussian with a zero mean and a standard deviation of 1.5 Pa. The free stream wind speed and noise on sensors 4-6 are shown in Figure 18(a) and Figure 18(b), respectively. It can be seen in Figure 18(b) that the simulated local flow separation happens during the time periods of 0.5-1 s, 2-2.5 s, and 3.5-4 s. Figure 19 shows that under the simulated unsteady flow environment, the pressure-sensor array based pitch control is able to achieve a satisfactory performance, with only small fluctuations when flow separation occurs. Pressure distributions sampled at t=0.5s, t=2.2s, and t=3.9s are shown in Figure 20.

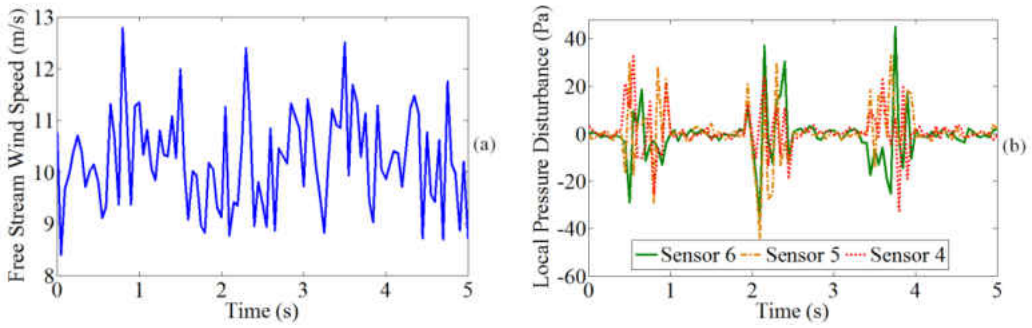

Figure 18 Unsteady flow in Case III: (a) unsteady free stream wind speed and (b) unsteady pressure at the locations of sensors 4, 5, and 6

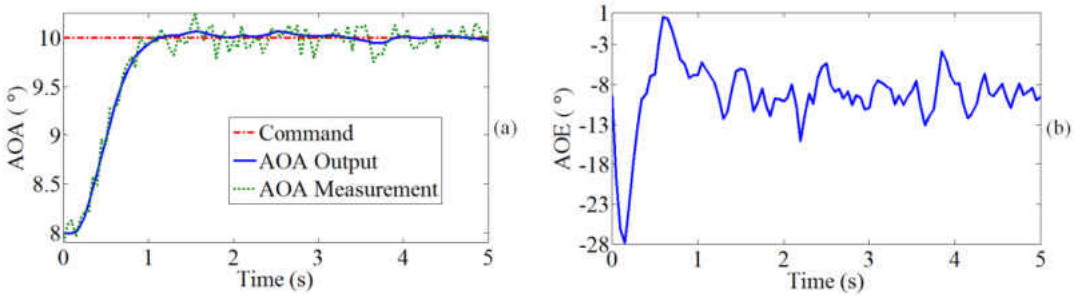

Figure 19 Simulation Case III: the angle of attack is commanded from 8° to 10°

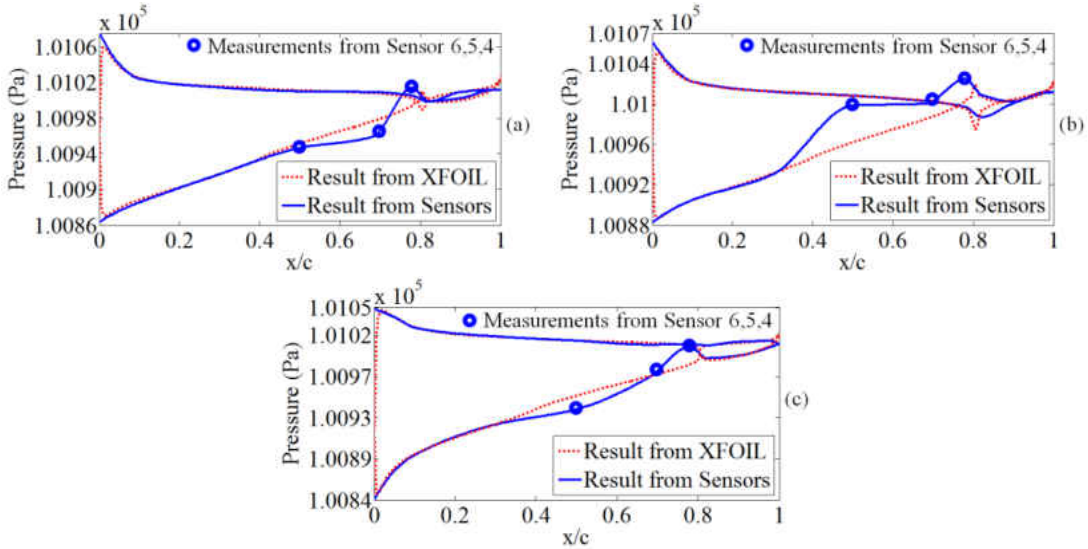

Figure 20 Pressure distribution in Case III at different times: (a) t=0.5s (b) t=2.2s (c) t=3.9s

Table 5 shows the performance of the pressure information based control in terms of the rising time, settling time, and overshoot. The testing results show that the closed-loop system is stabilized within 1.5 seconds and the overshoot is around 5%.

Table 5 Control performance

Simulation	Rise Time (s)	Settling Time (s)	Overshoot
Case I	0.78	1.20	5.00%
Case II	0.81	1.37	5.13%
Case III	0.84	1.13	4.95%

CHAPTER THREE: VALIDATION OF PITCHING CONTROL

In Chapter 2, we have designed a pitching control strategy of using real-time pressure information on the wing surfaces and the performance is validated in a simulated environment. In this paper, the hardware design and its experimental validation are discussed. In addition, a simple identification method is used to model the relationship between the angle of attack and the pressure near the leading edge. From this, the pitching control is designed using only pressure information. Multiple wind tunnel tests show that the closed-loop pitching control can track the commanded. The majority part of information in this chapter can be found in my paper [67].

Objective and Design Process

The basic conceptual design is shown in Figure 21. Unlike traditional designs, air pressure sensors will be embedded on both the upper and lower surfaces of the wing. These sensors are used to measure the real-time flow pressure, which will be further incorporated into flight control design.

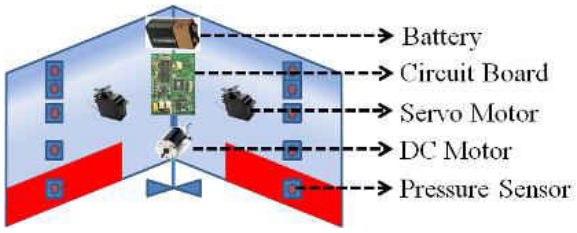

Figure 21 Pressure sensor enhanced MAV's conceptual design

Our previous results in [50] has shown that using limited number of pressure sensors on wing surface can get a good approximation of aerodynamic forces; at the same time, a simulation

of using pressure for pitch control is also demonstrated. Further research on hardware design, system implementation, and extensive wind tunnel tests hasn't been explored yet. The main objectives of this paper are (1) design a pressure sensor embedded pitch control testbed for fly-wing configured MAVs; (2) design and explore the effectiveness of using only pressure information for pitch control; and (3) experimentally validate the proposed pitching control approach.

The design follows an iterative process that is similar to the procedure of designing a full functioning MAV. As it is shown in Figure 22, each iteration process contains the following five steps.

Step 1-Design specification: It defines all constraints and requirements on the final design, such as the take-off weight constraint, testing facility size constraint, and performance requirements. In this paper, the following specifications are used: (1) wing size is smaller than 30 cm in both the chord and span; (2) total weight is less than 250 grams; and (3) stable pitching control should be achieved, with a rising time less than 2 seconds and an overshoot less than 10%.

Step 2-Configuration and Component Selection: The configuration includes the wing and airfoil shape, elevon size and location, center of gravity location, and aerodynamic center. Commercial-off-the-shelf products are selected according to the size, weight, and performance requirements from the design specifications and structural configuration.

Step 3-Testbed Design and Implementation: This is a vital step that determines the performance of the testbed. To find a rough arrangement of the hardware components, simulation in Solidworks R is done in prior to hardware implementation. Then, following the plan, a wing prototype is designed and manufactured. Note that small changes might be needed to achieve all

the design specifications.

Step 4-Control System Design: This step is mostly implemented in software, which including data acquisition, processing, controller design, and parameter tuning. Many tests need to be done to get a good offline data analysis and modeling.

Step 5-Test and Validation: Verify the performance of the system by conducting numerous wind tunnel tests. If desired performances are achieved, the design is finished. Otherwise, the design process will go back to step 2.

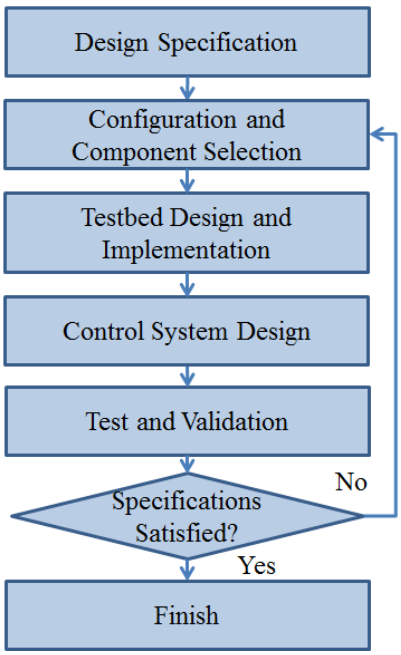

Figure 22 Block diagram of the design process

Testbed Design and Implementation

Focusing on the pitching control validation, a uniform, straight wing configuration is adopted as shown in Figure 23. In addition to the airfoil type, the wing span b, chord length c,

and elevon width d are used to define the wing geometry.

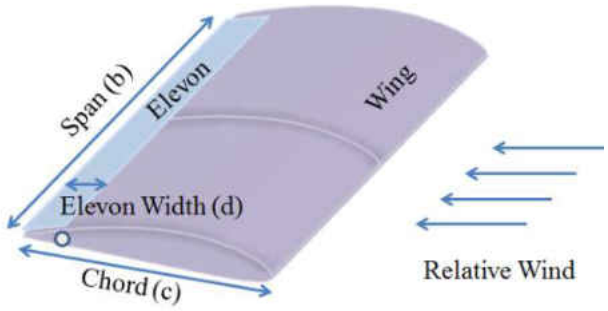

Figure 23 Simple wing configuration

Usually, the wing size is defined first, and then the airfoil can either be designed or selected from standard libraries. However, in this testbed design, there are special requirements on the airfoil, which must be suitable for low Reynolds flight, and larger in thickness to chord ration in order to fit all the electronics. Considering the above factors, the airfoil NACA4415 is selected for the wing section design. It is a low Reynolds number airfoil with a high lift to drag ratio. Meanwhile, this airfoil has a 15% maximum thickness, which allows for all of the hardware components to fit inside of the wing.

The barometric air pressure sensor BMP085 is chosen for the pressure measurement device. The configuration and features of the sensor are shown in Figure 24. It has a measurement range from 30 to 110 kPa, which is wide enough to capture all of the possible pressure data. At the same time, it has a resolution of 3 Pa, which compared to the pressure difference of several hundred Pa between the lower and upper surfaces of the wing, is accurate enough to precisely represent the pressure profile. Additionally, the sensor is small and light. At a size of 5×5×1.2 mm and a weight of 0.09 grams, it meets the requirements for the design. Considering the wing size specification on, 12 sensors are used in the current wing testbed

design.

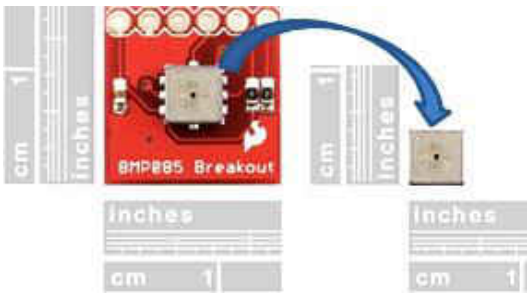

Features
Range: 30-110kPa
Resolution: 3 Pa
Size: 5×5×1.2 mm
Weight: 0.09 g
Power: 2.7V, 5μA
Frequency: 128 Hz

Figure 24 Barometric air pressure sensor BMP085™

A Hitec HS 55 servo motor is used to power the elevon. The servo motor has a size of 23×12×24 mm and weighs 8 grams. It can output a torque of 1.1 $kg \cdot cm$, which is strong enough for deflecting the elevon.

A 16 MHz Arduino Uno microcontroller is selected to acquire data from the sensors. It is compatible with the sensors' I2C interface. In addition, it has fourteen input/output pins, which are able to support twelve sensors, and one servo.

With all the major hardware components selected, the gross weight of the wing testbed ends up to about 243 grams, as shown in Table 6.

Table 6 Weight Breakdown of the Testbed

Component	Number	Weight
Sensor BMP085	12	10 gram
HS 55 Servo	1	8 gram
Microcontroller Board	1	25 gram
Structure and Coating*	1	70 gram
Wire and Other*	1	130 gram
	Total*	243 gram

Note: "*": approximated weight

Using the method described in [51], with a lift coefficient at the angle of attack α = 5o of

$C_L = 1$, the required wing area can be found from

$$S = 2W / (C_L \rho V^2) \tag{34}$$

where W is the take-off weight; ρ = 1.225 kg/m^3 the air density under standard atmospheric pressure at 15 ^{o}C; V is the cruse speed, it ranges from about 5 m/s to 20 m/s. Based on an approximated take-off weight of 300 grams, V =10 m/s, the required wing area is about 0.048 m^2. The aspect ratio AR for MAV designs is around 1~2 [52]. For a rectangular wing with a surface area of $S = bc$, and AR is given by

$$AR = b / c \tag{35}$$

Using $AR = 1$, the expected chord length and span would be 22 cm. Finally, the wing span is 26 cm, the chord length is 24 cm, and correspondingly the elevon width is 4.8 cm.

Typically, the elevon width should be within the range of 20% to 30% of the chord length (20% is chosen). To ensure the stability of the design, the center of gravity is designed to be at 20% of the chord length from the leading edge.

Intuitively, the sensor locations should be designed such that the pressure profile, which is curve-fitted using the discrete pressure information, can represent the actual pressure distribution with a high accuracy. Note that no optimal solution that would give best fitting results for all the operation states (e.g., flight velocity and attitude). To find these locations, the approximate pressure distribution is explored first using simulation. Many studies on computing pressure distributions have been investigated [53]. AVL© [54] is one example, which employs an extended vortex lattice model for the lifting surfaces analysis. By placing the horseshoe vortices sheet on the camber line defined surface of the wing, it provides a rough simulation of the pressure difference.

Although the simulated pressure distribution using AVL© is not accurate, it gives a rough idea of where the sensors should be placed and how they should be laid out. Figure 5 shows the distribution of pressure difference under different angles of attack and different angles of elevon. Cp is the pressure coefficient. The simulation settings are given in Table 7, where V_∞ is the free stream wind speed, α is the angle of attack, and δ_e is the angle of elevon.

Table 7 Pressure Simulation Setting

Tests	V_∞	α	δ_e	**Tests**	V_∞	α	δ_e
(a)	10 m/s	7	0	**(c)**	10 m/s	7	10
(b)	10 m/s	10	0	**(d)**	10 m/s	7	10

It can be seen from Figure 25 that the pressure distribution changes significantly around regions near the leading edge and the pivot hinge. It gives us a feeling that more sensors need to be placed around these two regions to get a more accurate pressure distribution. Many different sensor location patterns are tried and compared and the final layout is given in Table 8. Here, sensors 1-6 are on the upper surface while 7-12 are on the lower surface of the wing. Sensor location (x, y) is measured from the leading edge and the left wingtip. The values are given in the ratios of x/c and y/b. For example, sensor 1 is located at 87.79% of the chord length from the leading edge and 7.63% of the span from the left wing tip.

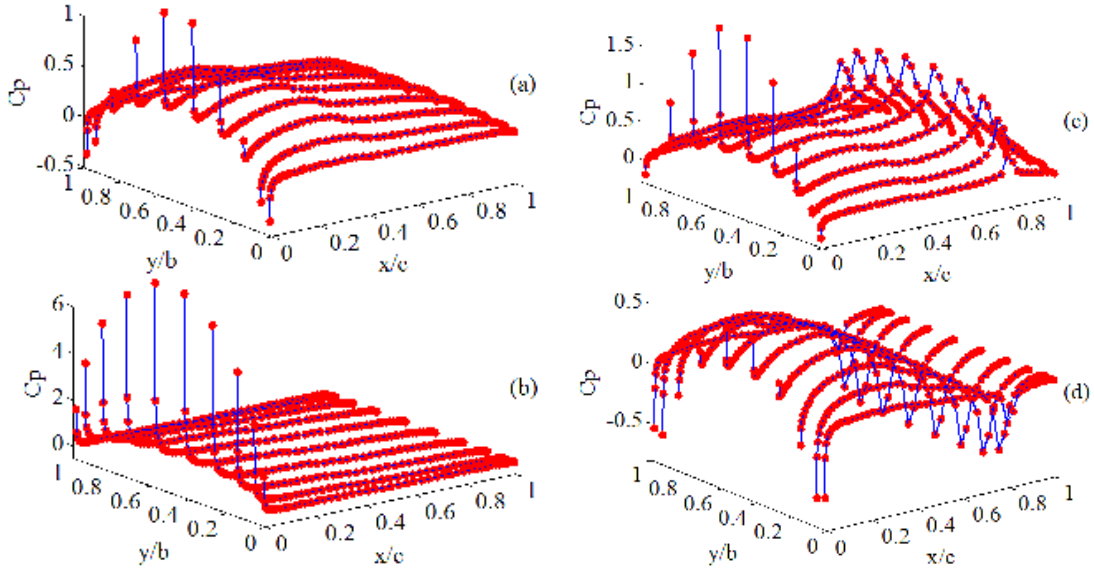

Figure 25 Simulated pressure difference distribution in different scenarios

Table 8 Sensor Locations

Sensor	**1**	**2**	**3**	**4**	**5**	**6**
x/c	87.79%	76.34%	54.20%	24.81%	15.27%	1.15%
y/b	7.63%	15.65%	33.59%	51.53%	73.28%	87.40%
Sensor	**7**	**8**	**9**	**10**	**11**	**12**
x/c	1.15%	15.27%	24.81%	54.20%	76.34%	87.79%
y/b	6.87%	21.76%	40.08%	58.78%	76.72	86.64%

Figure 26 shows the structural design and arrangement of the hardware components. The wing ribs are constructed from balsa wood sheets. The sensors are mounted on small balsa platforms, which are glued directly to the sides of the ribs. To make the structure stronger, the Alaskan yellow cedar, which is four times denser than the balsa wood, is used for the leading edge. A plastic tube runs through the center of gravity, which is used to mount the wing inside the wind tunnel. All communication wires run through this tube to avoid generating disturbance torque. Finally, the wing will be coated with Monokote.

To move the center of gravity forward to 20% of the chord, the microcontroller board,

together with the “battery and propulsion systems” (represented by metal weights), are placed close to the leading edge.

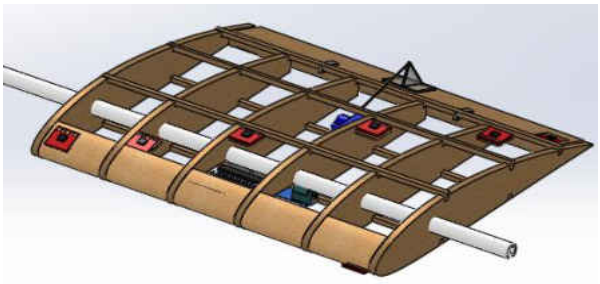

Figure 26 Structural design and arrangement of components

Figure 27 shows the circuit design of the testbed. It can be seen that, the circuits inside of the wing include twelve sensors, a microcontroller board, a servo motor, a control box, and connection wires. At each time instance, the micro controller reads data from the sensors and sends them to the laptop computer through the control box. The control box is composed of a potentiometer, a reset button, and a LED light. It also allows for manual controls of the elevon and to reset the circuit. A LED is used to indicate the status of the system. The microcontroller reads pressure from sensors using the I2C connection, while the serial communication is used between the control box and the laptop. The servo motor is controlled by the microcontroller generated pulse width modulation signals.

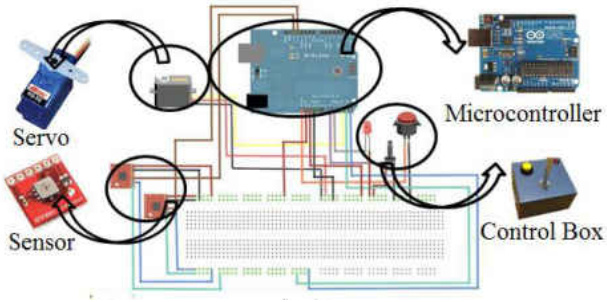

Figure 27 Circuit design

Following the circuit design, a hardware system is implemented as shown in Figure 28. To ensure the surface of the wing is strongly coated, is strong enough, we did not In order not not weaken the structure too much, constrained the space left between the plastic tube and the surface of the wign, the microcontroller board cannot be placed any further forward constrained by the thicknesses of the board and the wing.

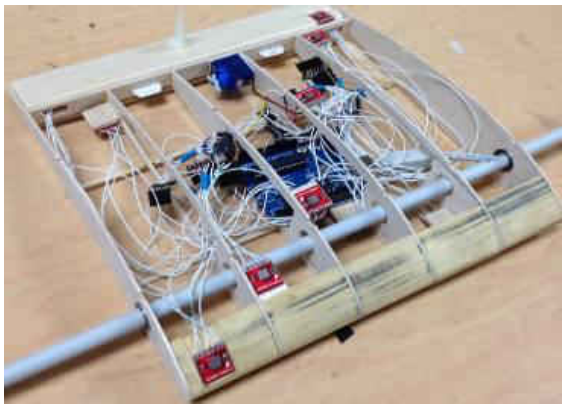

Figure 28 Hareware sytem implementation

The software is divided into two parts, in which one runs inside the microcontroller programed with C, and the other executes in a laptop using Matlab. As is shown in Figure 29, the code inside the micro controller is in charge of pressure data acquisition and servo control, and dealing with service interruption from the computer. Examples of interruption are sending data

and receiving commands. The software written in Matlab is used to process data from the microcontroller, run control algorithm, and generate commands.

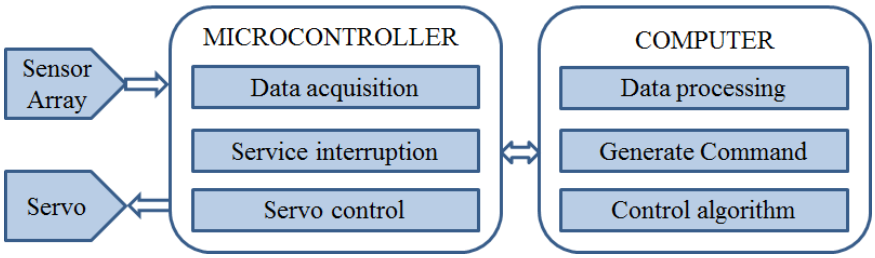

Figure 29 Software design

Combining the hardware and software, the whole system is shown in Figure 30. The system works in either one of the two modes: manual mode and autonomous mode. In the manual mode, the elevon is manually controlled by tuning the potentiometer in the control box. In the autonomous mode, the controller would control the wing to a desired angle of attack autonomously. In the autonomous mode, the testbed allows manual interactions by detecting changes in the potentiometer. Whenever there is a change in potentiometer, the elevon will respond. If there is no change in 3 seconds, it will go back to autonomous mode.

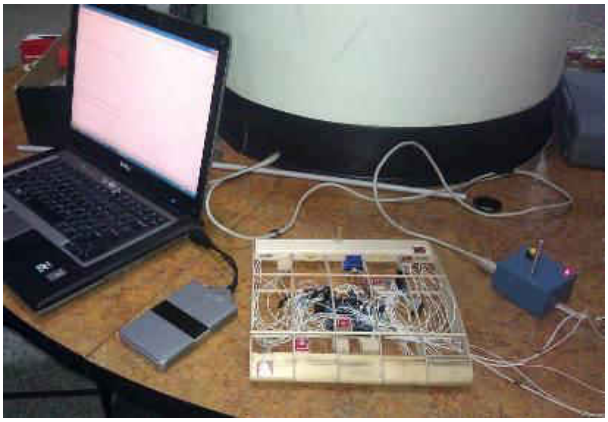

Figure 30 Completed design of the wing testbed

Control System Design

The system data flow diagram is shown in Figure 31. The sensors on the surfaces of the flying wing acquire the real-time pressure data. Interpolating the discretized pressure data, an approximated pressure distribution will be obtained. Then, the angle of attack will be identified from the pressure distribution near the leading edge. At the same time, together with the pressure distribution, the commanded and computed actual angle of attack will be sent to the controller. Finally, the controller decides the deflection of the elevon to control the pitching motion.

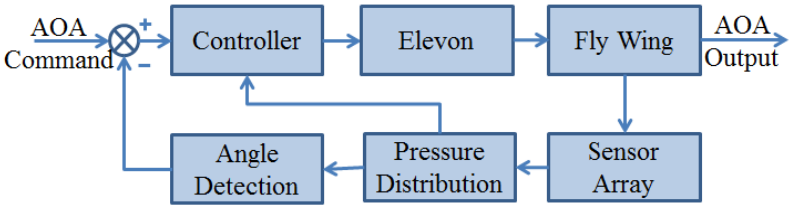

Figure 31 System data flow diagram

Since the angle of attack can be computed from pressure information, it could enable MAVs to fly without other sensing devices. Studies in [32, 33] indicate that the pressure difference from the lower and upper surfaces near the leading edge has a strong relationship with the angle of attack. Here, a simple identification method (i.e. a curve fitting approach) [55] is customized to find a proper mapping function from the pressure to the angle of attack. It is assumed that the mapping function is a polynomial as

$$\alpha = f(\Delta p, \theta^{\alpha}) = \theta_0^{\alpha} + \theta_1^{\alpha}\Delta p + \theta_2^{\alpha}\Delta p^2 + \ldots + \theta_n^{\alpha}\Delta p^n \tag{36}$$

where Δp is the frontal pressure difference, $\theta_i^{\alpha}, i = 1, \ldots, n$ are the parameters to be estimated from identification, and n is the order of the mapping function. To avoid overfitting and obtain a

more accurate statistical model, the cross validation technique is used to find the mapping function parameters [56]. Here, the test data will be randomly separated into two complimentary sets, one of which is the training set and the other is the validation set. The training set is used to find the coefficients in the mapping function, while the validation set is used to test the accuracy of the model. The following root mean square error is minimized

$$\hat{f} = \arg\min_{f_k} \left\{ \sqrt{\frac{1}{N_v N_c} \sum_{j=1}^{N_c} \sum_{i=1}^{N_v} (\alpha_{ijk} - \hat{\alpha}_{ijk})^2} \right\} \tag{37}$$

$$i = 1, 2, ..., N_v,\ j = 1, 2, ..., N_c,\ k = 1, 2, ..., N_f$$

where N_v is the number of data in the validation set, N_f is the number of data in the training set, N_c is the time of cross validations, f_k is the k^{th} mapping function candidate, $\hat{\alpha}_{ijk}$ is the estimated value at point i under the j^{th} cross validation using the mapping candidate k.

The servo motor can be controlled precisely. However, the deflection angle of elevon depends not only on the servo output but also the structure assembly. Instead of going through a tedious procedure to find an analytical solution using the geometrical relations (shown in Figure 32), the mapping function is approximated by using the same identification method described in Section V.B.

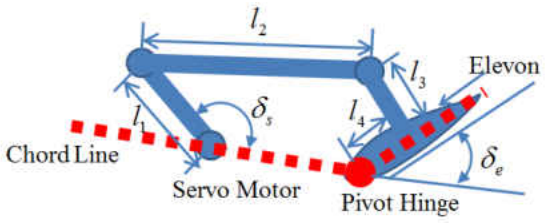

Figure 32 Geometric configuration of servo and elevon

Polynomial functions, with orders from 1 to 5, are tried and 10 cross validations are

carried out. The root mean square error (RMS) is illustrated in Figure 33, and as can be seen, the third order polynomial model has the smallest RMS error and thus is chosen as the mapping function

$$\delta_e = \theta_0^\delta + \theta_1^\delta \delta_s + \theta_2^\delta \delta_s^{\,2} + \theta_3^\delta \delta_s^{\,3} \tag{38}$$

where δ_s is the servo output, and the coefficients of the model are found to be $\theta_0^\delta = -45.222$, $\theta_1^\delta = 1.768$, $\theta_2^\delta = -0.015$, and $\theta_3^\delta = 6.016\times10^{-5}$. The corresponding fitted result is shown in Figure 34.

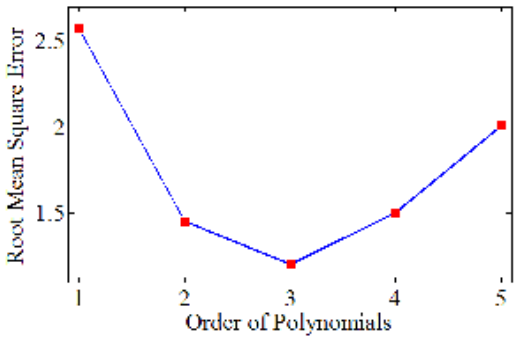

Figure 33 Root mean square error with models of different orders

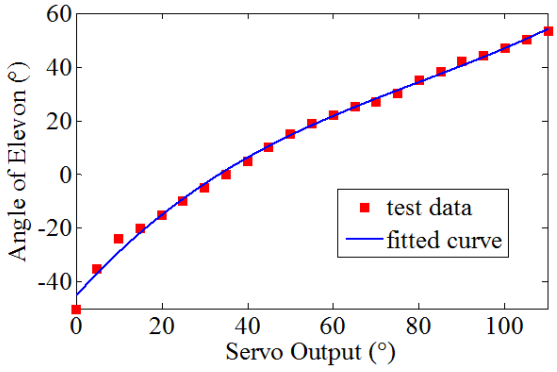

Figure 34 Relationship between the servo output to the elevon deflection

The control block is shown in Figure 35, in which the inputs are the reference command (desired value) α_d, detected angle of attack $\hat{\alpha}$, and pressure distribution $p(x)$. The output is the elevon deflection angle δ_e.

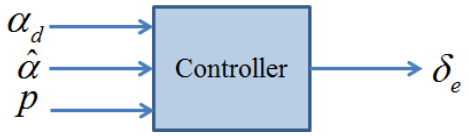

Figure 35 The control unit

After the wing is stabilized, the center of pressure would fall on the center of gravity and the angle of attack would be controlled to the desired value. To make the control system more stable, a PID controller, which combines these two signals from the pressure distribution, is designed for the pitching control as

$$\Delta\delta_e = K_1^P e_1 + K_1^I \int e_1 dt + K_1^D \dot{e}_1 + K_2^P e_2 + K_2^I \int e_2 dt + K_2^D \dot{e}_2 \tag{39}$$

where the error signals e_1 and e_2 are calculated using

$$e_1 \triangleq x_{cp} - x_{cg} \tag{40}$$

and

$$e_2 \triangleq \alpha_d - \alpha \tag{41}$$

x_{cp} is the center of pressure, x_{cg} is the center of gravity, α is current angle of attack, and α_d is desired angle of attack. x_{cp} and α are found from the moving average filters as

$$x_{cp}(t_k) = \frac{1}{h}\sum_{i=0}^{h-1} \hat{x}_{cp}(t_{k-i}) \tag{42}$$

and

$$\alpha(t_k) = \frac{1}{h}\sum_{i=0}^{h-1}\hat{\alpha}(t_{k-i}) \tag{43}$$

where h is the width of the moving average filter. $\hat{x}_{cp}(t_k)$ and $\hat{\alpha}(t_k)$ are the estimated center of pressure and the computed angle of attack from the pressure measurement at time t_k. $\hat{\alpha}(t_k)$ is found from Eq. (36). $\hat{x}_{cp}(t_k)$ is calculated by

$$\hat{x}_{cp}(t_k) = \frac{\int_0^c x(p_l(t_k) - p_u(t_k))\,dx}{\int_0^c (p_l(t_k) - p_u(t_k))\,dx} \tag{44}$$

where p_l and p_u are the pressure distributions on the lower and upper surfaces. The control law is

$$\delta_e = \delta_e^* + \Delta\delta_e \tag{45}$$

where δ_e^* is the initial elevon deflection.

Wind Tunnel Experiment

The facility used to perform the tests is the low speed wind tunnel located at University of Central Florida, as shown in Figure 36. It is a suction type, non-return wind tunnel with a testing section of 60×30×30 cm and can provide a speed ranges from 5 m/s to 25 m/s. The data acquisition system is composed of a protractor, a wind speed measurement unit, and a force gauge. The protractor has an accuracy of 1 degree. The wind speed measurement device is DATUM 2000TM produced by Setra. The DATUM 2000TM measures the pressure with an accuracy of 0.01 inch water column (inw), which will be further converted to the wind speed using the pressure-speed relation.

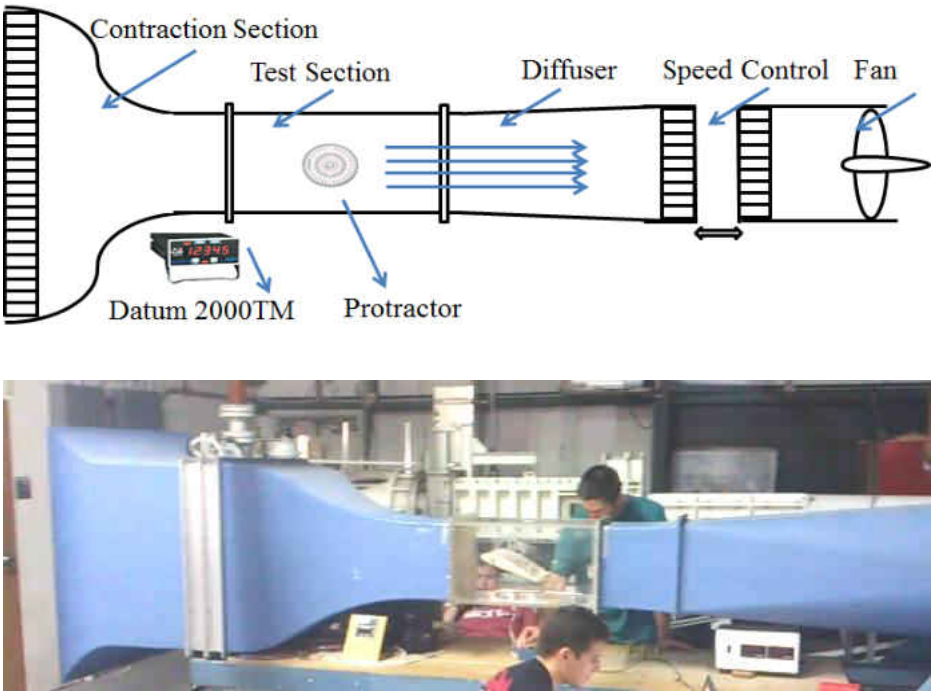

Figure 36 Low speed wind tunnel facility: (a) sketch and (b) photo

Figure 37 shows the wind tunnel test setup, which consists of three components: the flying wing, the control station (a laptop), and the wind tunnel. The flying wing is mounted inside the wind tunnel by the tube that goes through the center of gravity. The command wire goes through the tube and connects to the laptop. The laptop is used to send control commands to the servo motor

The data to be measured in these tests includes the free stream wind speed, pressure data, angle of elevon and angle of attack. The free stream wind speed is measured in inches of water column, which is converted to m/s by the following equation,

$$V_\infty = \sqrt{2\kappa V_m / \rho} \tag{46}$$

where $\kappa = 248.8$ is a constant that convert the unit of inches of water column to Pa, $\rho = 1.225$ kg/m^3 is air density, and V_m is the measured wind speed with the unit of inches of water column.

The pressure data and angle of elevon can be automatically saved using the designed software. In order to reduce the errors coming from the angle of attack readings, experiments are recorded using a SONY DSC-HX100V camera.

Figure 37 Wind tunnel testing setup: (a) Top view and (b) Side view

To test the wing pitch stability, turbulent flow is simulated by applying sudden changes in the wind speed and directions. The sudden wind speed change can be easily realized by adjusting the wind speed rapidly. Considering the fact that the wind direction change in the pitching motion is similar to the angle of attack change, sudden direction changes in the wind flow is simulated by applying sudden changes in angle of attack.

Figure 38 gives an example of how the test is carried out. The whole process is recorded by the camera, so that the wind speed and angle of attack can be recorded at the same time. In testing the disturbance rejection capability of the wing pitch motion, a rod is used to lift the wing up by an angle within a range of -5 to 5 degrees then quickly releasing it. Figure 39 gives an example of the testing process. In this example, at 52 seconds, the angle of attack is lifted up by 5 degrees and then released, and the wing quickly returns to its original state.

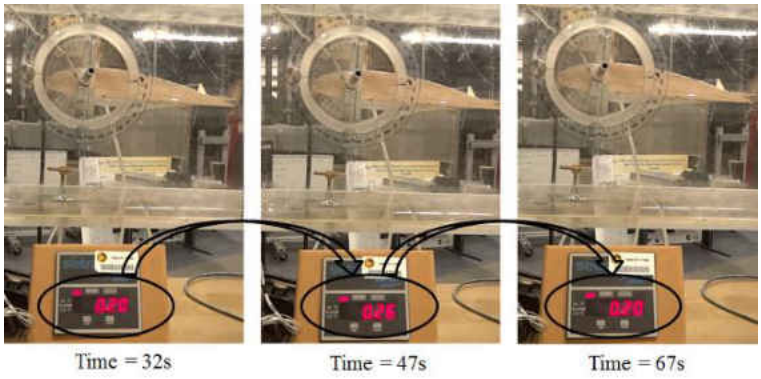

Figure 38 An example of stability test under wind speed disturbance

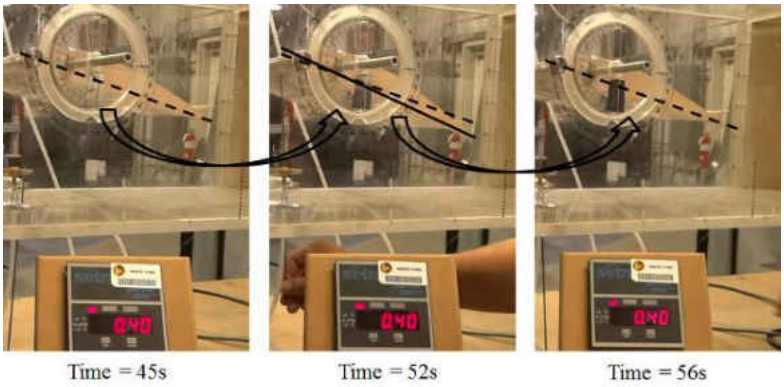

Figure 39 An example of stability test under wind direction disturbance

The test settings and results are shown in Table 9, where α and δ_e is the flight status before the disturbances are applied. Under the conditions that the wind speeds range from 8 m/s to 14 m/s, with the disturbances range from -4 m/s to 4 m/s in magnitude and -5 degrees to 5 degrees in direction, the wing is always stable.

Table 9 Stability under Different Wind Speed

Steady Flight				**Disturbance**		**Result**
V_∞		α	δ_e	ΔV	$\Delta\alpha$	
0.16 inw	8 m/s	10^o	20.11^o	1.5 m/s	4^o	Stable
0.21 inw	10m/s	12^o	22.43^o	3.4 m/s	5^o	Stable
0.35 inw	12 m/s	14^o	25.73^o	-4.0 m/s	-5^o	Stable
0.49 inw	14 m/s	16^o	33.93^o	-3.5 m/s	-4^o	Stable

The frontal pressure difference (the pressure difference of sensors 6 and 7) is recorded under wind speeds of 8 m/s, 10m/s, 12 m/s, and 14m/s and the results are shown in Figure 40. The dots represent the measured data, while the lines are linear curve fitted from these measurements. It can be seen that, under a specific wind speed, the angle of attack and frontal pressure difference have a very strong linear relationship. To avoid over fitting, the first order polynomial model is selected to identify the angle of attack. Under different wind speeds, the relationship between the frontal pressure difference and angle of attack is described using a group of first order polynomials, but with different slopes and interceptions.

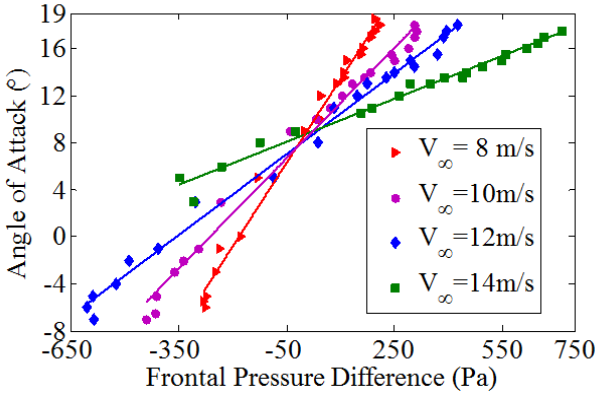

Figure 40 Experimental data of fontral pressure difference and angle of attack

From the above analysis, the mapping function is giving by the following slop-intercept

linear form

$$\hat{\alpha}_{V_\infty} = \theta_0^\alpha + \theta_1^\alpha \Delta p \tag{47}$$

Here, $\hat{\alpha}_{V_\infty}$ is estimated angle of attack under the wind speed of V_∞, and the coefficients θ_0^α and θ_1^α in the above tests are given in Table 10. It provides the coefficients of the model at four different wind speeds. Coefficients under other wind speeds can be found from the spline-fitted curve, as shown in Figure 41.

Table 10 Coefficients for Angle of Attack Identification

Wind	**Parameters**		**95% Confidence Bounds**	
V_∞	θ_0^α	θ_1^α	θ_0^α	θ_1^α
8 m/s	8.658	0.047	(8.206, 9.111)	(0.045, 0.050)
10 m/s	8.224	0.031	(7.746, 8.702)	(0.030, 0.033)
12 m/s	8.15	0.023	(7.741, 8.560)	(0.022, 0.024)
14 m/s	8.676	0.012	(8.308, 9.044)	(0.011, 0.013)

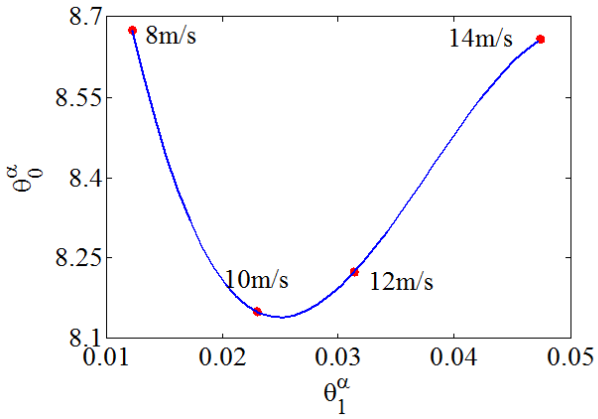

Figure 41 Parameter selection according to wind speed

With the controller designed in section V, the pitching control system is tested under the wind speeds of 8 m/s, 12 m/s and 14 m/s. The PID gains in the controller are chosen to be

$K_1^P = 0.5$, $K_1^I = 0.008$, $K_1^D = 0.1, K_2^P = 0.6$, $K_2^I = 0.005$ and $K_2^D = 0.3$.

The experiment tests under the wind speeds of 8 m/s, 12 m/s and 14 m/s are shown in Figure 42, Figure 43 and Figure 44, respectively. The test settings and system performances are given in Table 11, where α_{t_0}, α_{t_f}, σ t_r, and t_s are the initial angle of attack, steady state, overshoot, rising time, and settling time, respectively.

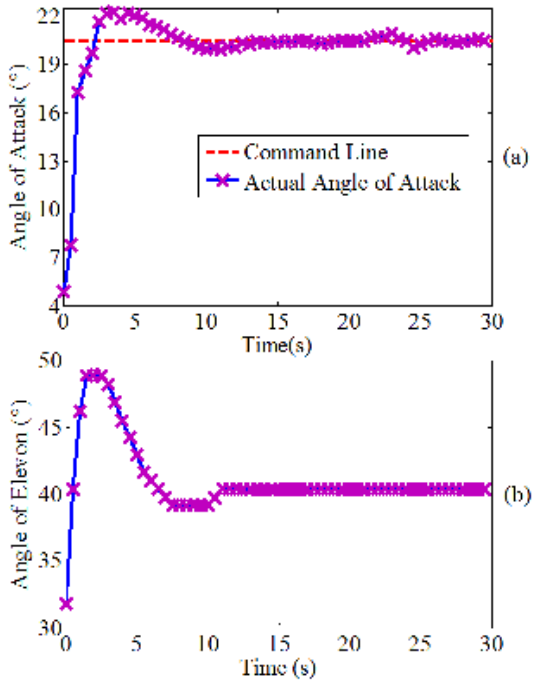

Figure 42 Wind tunnel test I: wind speed 8 m/s (a) angle of attack and (b) angle of elevon

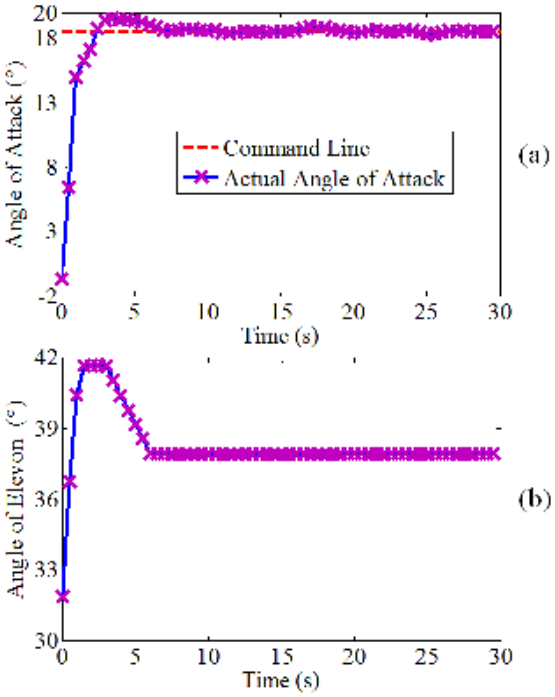

Figure 43 Wind tunnel test II: wind speed 12 m/s (a) angle of attack and (b) angle of elevon

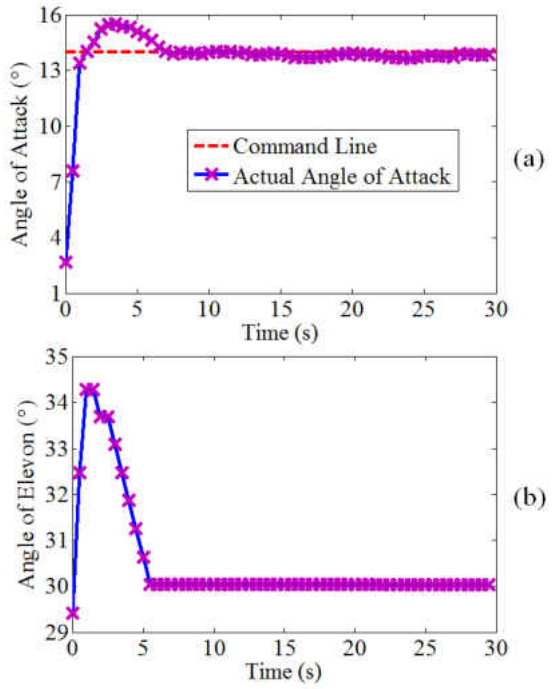

Figure 44 Wind tunnel test III: wind speed 14 m/s (a) angle of attack and (b) angle of elevon

Table 11 Test Setting and System Performance

Tests	V_∞	α_d	α_{t_0}	α_{t_f}	σ	t_r	t_s
I	8 m/s	20.5	4.5	20.5	9.38%	2.0 s	5.48 s
II	12 m/s	18.5	-1	18.5	5.13%	2.0 s	4.96 s
III	14 m/s	14.0	2.5	1.4.0	13.0%	1.8 s	6.50 s

As shown in Table 11, the rising time, settling time, and overshoot are approximately 2 seconds, 5 seconds, and 10%, respectively. In addition, the angle of attack curves are smooth, which indicate that the simple curve-fitting method for the identify angle of attack from the frontal pressure differences is accurate enough.

CHAPTER FOUR: THREE AXIS ATTITUDE CONTROL

The research results reported in Chapters 2 and 3 have demonstrated the effectiveness of using pressure information only for micro air vehicle's pitching control in both simulation and wind tunnel tests. In this chapter, we extend our research from the pressure information based pure pitching control to a three-axis attitude control using both pressure and shear information measured by an array of flow sensors [61]. Compared to the pure pitching control scenario [50], three-axis attitude control faces additional challenges and the main contributions of the paper are as followed. First, more complex flow conditions will be encountered since the three dimensional MAV geometry is considered and more control surfaces are incorporated to achieve enough control authorities. Second, the locations and number of sensors are carefully designed such that the force and moment through curve fitting (for the point-wise distributed pressure and shear measured by individual sensors) and integration can be used to approximate the actual forces and moments experienced by the MAV. Third, a new model relating the flow information and the attitude states (Euler angles and angular velocity) is derived. Fourth, the closed–loop system is robust with respect to more severe uncertainties and disturbances as compared with the pure pitching control cases.

The rest of this chapter is organized as follows. Firstly, the conceptual MAV design with embedded flow sensor couples is discussed. Secondly, the new dynamic model capturing the relationships between the flow information and the flight status is derived, based on which a nonlinear robust controller is designed. Finally, a simulated environment is constructed, in which the capabilities of the new MAV concept and the closed-loop control performance are demonstrated.

Conceptual Design

A delta flying-wing configuration is adopted in the MAV design as shown in Fig. 2. As compared with wing-tail configurations, the induced drag in the flying-wing configuration is smaller and the MAV can fly with a wider range of angle of attack [3]. NACA 4415 is selected as the airfoil section specifically for low Reynolds number flights. The wing span, root chord, and tip chord are designed to be 15 cm, 10 cm, and 5 cm, respectively, and the MAV weighs 250 grams. Two elevons and a rudder are used to control the attitude motion of MAV. The pitching control can be achieved by moving two elevons in the same direction, while the roll and yaw motions are coupled and can be controlled by a combination of the elevons and rudder deflections.

Two sensor strips (Figure 45(b)), simultaneously measuring the pressure and shear stresses, are embedded on the wing surface and a sensor couple (Figure 45(c) and Figure 45(d)) is installed on the rudder surface. Each sensor strip has sensors on both upper and lower wing surfaces. To achieve the stability in the longitudinal direction, the center of gravity is at 20% of the root chord with all avionics onboard. The lateral direction stability of the wing is enhanced by a small dihedral angle. The notations of the symbols used in the wing geometry are listed in Table 12.

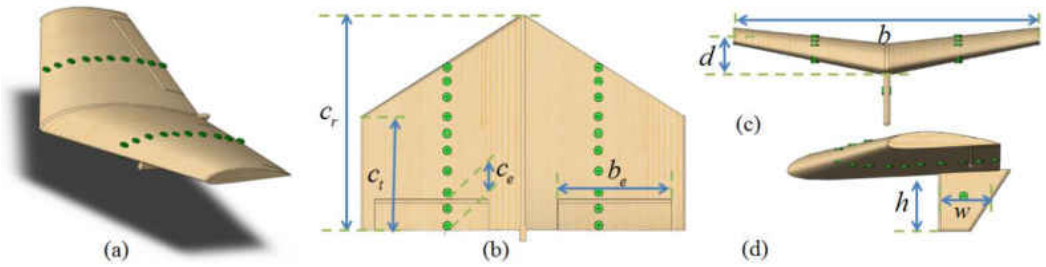

Figure 45 The delta flying-wing configuration: (a) 3-D view, (b) top view, (c) front view, and (d) side view

Table 12 Geometry definitions and design parameters

Symbol	Definition	Value	Symbol	Definition	Value
c_r	Chord length of the wing root section	10 *cm*	h	Rudder length	3 *cm*
c_t	Chord length of the wing tip section	5 *cm*	w	Rudder width	3 *cm*
b	Wing span	15 *cm*	J	The moment of inertia $\begin{bmatrix} 0.0526 & 0 & 0.0049 \\ 0 & 0.0804 & 0 \\ 0.0049 & 0 & 0.0405 \end{bmatrix}$	$Kg\ m^2$
c_e	Elevator width at the mean aerodynamic chord section	2 *cm*			
b_e	Elevator length	7.5 *cm*			
d	Dihedral height at the tip	1 *cm*			

It is desirable to have as many sensors as possible in order to achieve accurate flow profiles; however, due to the weight, surface area, volume, and power constraints, only a limited number of sensors can be embedded on the wing and rudder surfaces of an MAV. To get an accurate flow profile with a finite number of sensors, two sensor strips are span-wisely distributed along the mean aerodynamic chord (MAC) of the wing, as shown in Fig. 2(b). According to the definition in [51], the MAC is the chord of an equivalent rectangular wing that has the same wing area, aerodynamic force, and center of pressure as those of the delta flying-wing. The MAC can be found using the geometric method described in [51]. The sensor locations within the sensor strip are chosen according to the curvature of the airfoil mean

camber. The sensors near the pivot hinge of elevons are adjusted to capture possible prompt changes in the pressure and shear stresses. The results in [50] showed that ten pressure sensors on each of the bottom and upper surfaces of the wing can lead to a good approximation of the pressure distribution. Here only one sensor couple is placed in the middle of the flat rudder surfaces.

The block diagram of the pressure and shear information augmented attitude control system is illustrated in Figure 46. In addition to the typically used attitude feedback loop, the information coming from the pressure and shear sensors are fed into the controller. The pressure/shear information is used to calculate the approximated force, part of the drag, and moments acting on the MAV, which will be used in assisting the nonlinear robust controller.

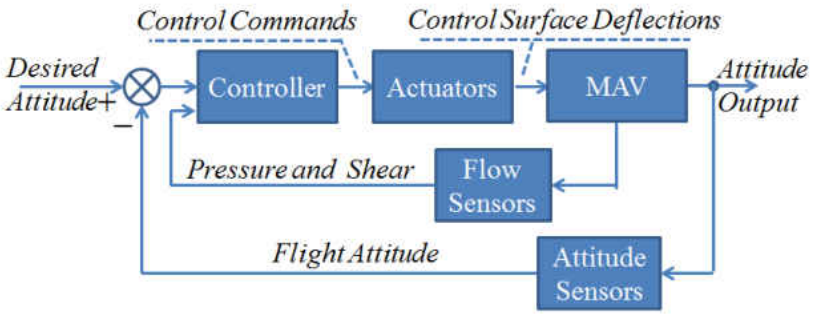

Figure 46 Block diagram of the proposed three-axis attitude control system

Three coordinate systems (the body coordinate and two surface coordinates) are used in the flow analysis as defined in Table 13. The superscripts B, WS, and RS refer to the body, wing surface, and rudder surface coordinates, respectively.

Table 13 Coordinate systems used in the force and moment calculations

Coordinate System	Axis	Unit Vector
Body Coordinate	X^B: point forward along the root chord line	$\hat{e}_X^B$
	Y^B: point to the right	$\hat{e}_Y^B$
	Z^B: point downward defined by the right hand rule	$\hat{e}_Z^B$
Surface Coordinate on the Wing	X^{WS}: point forward and tangential to the surface	$\hat{e}_X^{WS}$
	Y^{WS}: point to the right and tangential to surface	$\hat{e}_Y^{WS}$
	Z^{WS}: inner normal of the surface	$\hat{e}_Z^{WS}$
Surface Coordinate on the Rudder	X^{RS}: point forward and tangential to the surface	$\hat{e}_X^{RS}$
	Y^{RS}: point to the right and normal to surface	$\hat{e}_Y^{RS}$
	Z^{RS}: point downward and tangential to the surface	$\hat{e}_Z^{RS}$

The forces acting on an arbitrary element of the wing surface are shown in Figure 47, where p_{WS} is the pressure on the wing along the inner normal direction $\hat{e}_Z^{WS}$, $\tau_{WS,X}$ is the shear stress along $\hat{e}_X^{WS}$, and $\tau_{WS,Y}$ is the shear stress along $\hat{e}_Y^{WS}$. The lengths of the infinitesimal element are denoted by ds_X^{WS} and ds_Y^{WS}.

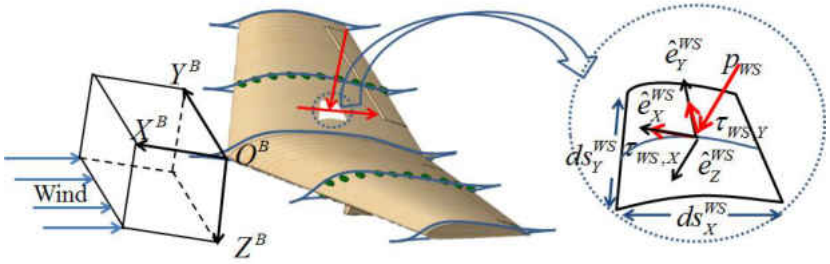

Figure 47 Pressure and shear stress analyses on an arbitrary wing surface element

If the position vector of the surface element is given by $\vec{r}_{WS}$, the force and moment with respect to the center of gravity is calculated by

$$\begin{cases} d\dot{f}_{WS} = (p_{WS}\hat{e}_Z^{WS} + \tau_{WS,X}\hat{e}_X^{WS} + \tau_{WS,Y}\hat{e}_Y^{WS})ds_X^{WS}ds_Y^{WS} \\ d\dot{m}_{WS} = (\dot{r}_{WS} - \dot{r}_{cg}) \times (p_{WS}\hat{e}_Z^{WS} + \tau_{WS,X}\hat{e}_X^{WS} + \tau_{WS,Y}\hat{e}_Y^{WS})ds_X^{WS}ds_Y^{WS} \end{cases} \tag{48}$$

where $\vec{r}_{cg}$ is the center of gravity of the MAV. Then the force $\dot{f}_{WS}$ and moment $\vec{m}_{WS}$ contributed by the pressure and shear acting on the wing surface can be found by integrating Eq. (1) over the whole wing surface as

$$\begin{cases} \dot{f}_{WS} = \oiint_{WS} (p_{WS}\hat{e}_Z^{WS} + \tau_{WS,X}\hat{e}_X^{WS} + \tau_{WS,Y}\hat{e}_Y^{WS})ds_X^{WS}ds_Y^{WS} \\ \dot{m}_{WS} = \oiint_{WS} (\dot{r}_{WS} - \dot{r}_{cg}) \times (p_{WS}\hat{e}_Z^{WS} + \tau_{WS,X}\hat{e}_X^{WS} + \tau_{WS,Y}\hat{e}_Y^{WS})ds_X^{WS}ds_Y^{WS} \end{cases} \tag{49}$$

The stress analysis for an arbitrary element with the position vector $\vec{r}_{RS}$ on the rudder surface is shown in Figure 48, where $\hat{e}_Y^{RS}$ is the unit vector of the pressure along the inner normal direction of the rudder surface, and $\hat{e}_X^{RS}$ and $\hat{e}_Z^{RS}$ are the unit vectors along the shear stress directions. ds_X^{RS} and ds_Z^{RS} are the lengths of the infinitesimal element. The force and moment on the rudder can be calculated by

$$\begin{cases} \dot{f}_{RS} = \oiint_{RS} (p_{RS}\hat{e}_Y^{RS} + \tau_{RS,X}\hat{e}_X^{RS} + \tau_{RS,Z}\hat{e}_Z^{RS})ds_X^{RS}ds_Z^{RS} \\ \dot{m}_{RS} = \oiint_{RS} (\dot{r}_{RS} - \dot{r}_{cg}) \times (p_{RS}\hat{e}_Y^{RS} + \tau_{RS,X}\hat{e}_X^{RS} + \tau_{RS,Z}\hat{e}_Z^{RS})ds_X^{RS}ds_Z^{RS} \end{cases} \tag{50}$$

and the pressure and shear generated force and moment on the MAV can be found using

$$\begin{cases} \dot{f} = \dot{f}_{WS} + \dot{f}_{RS} \\ \dot{m} = \dot{m}_{WS} + \dot{m}_{RS} \end{cases} \tag{51}$$

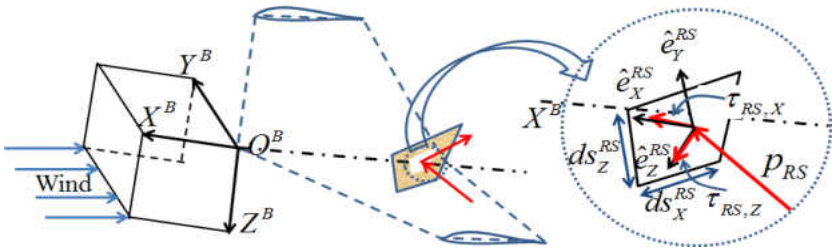

Figure 48 Pressure and shear stress analyses on an arbitrary rudder surface element

Ideally, information from an infinite number of pressure and shear sensor couples would be integrated to obtain accurate force and moment values. However, in reality, due to the size, weight, volume, and power constrains, only a limited number of sensors can be placed on the wing and rudder surfaces. To obtain a good approximation of the actual flow profile, two sensor strips are embedded on the MAC section along the chord direction as shown in Figure 49(a). The equivalent rectangular wing is shown in Figure 49(b), over which the flow information integrated along the MAC can represent the overall flow profile in terms of the resultant force and moment. Here, "C.G." refers to the center of gravity. The locations of these sensors along the MAC are shown in Table 14, where the numbers are given in the percentages of the distances measured from the leading edge to the sensor locations with respect to the MAC.

Table 14 Chord-wise locations of the pressure/shear sensors along the MAC

Sensor No.	1	2	3	4	5	6	7	8	9	10
Location	1%	4%	10%	25%	50%	70%	74%	76%	85%	98%

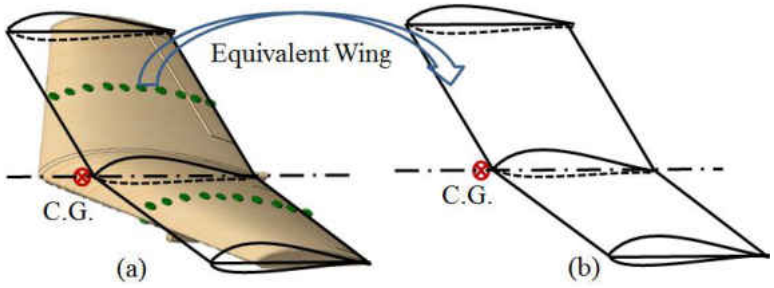

Figure 49 Equivalent rectangular wing with the same aerodynamic chord along the wing span

The transformation from the wing surface coordinate to the body coordinate $T_{B/WS}$, following a 2-1 rotation sequence, is given by

$$T_{B/WS} = \begin{bmatrix} 1 & 0 & 0 \\ 0 & \cos\vartheta_d & \sin\vartheta_d \\ 0 & -\sin\vartheta_d & \cos\vartheta_d \end{bmatrix} \begin{bmatrix} \cos\vartheta_f & 0 & \sin\vartheta_f \\ 0 & 1 & 0 \\ -\sin\vartheta_f & 0 & \cos\vartheta_f \end{bmatrix} \tag{52}$$

where ϑ_d and ϑ_f are the dihedral angle and airfoil curvature angle as illustrated in Figure 50. The rotation angle and its sign for the left wing can be defined accordingly. Similarly, the transformation from the rudder surface coordinate to the body coordinate system is given by

$$T_{B/RS} = \begin{bmatrix} \cos\delta_r & -\sin\delta_r & 0 \\ \sin\delta_r & \cos\delta_r & 0 \\ 0 & 0 & 1 \end{bmatrix} \tag{53}$$

in which δ_r is the rudder deflection with the positive sign denoting the case of deflecting towards right.

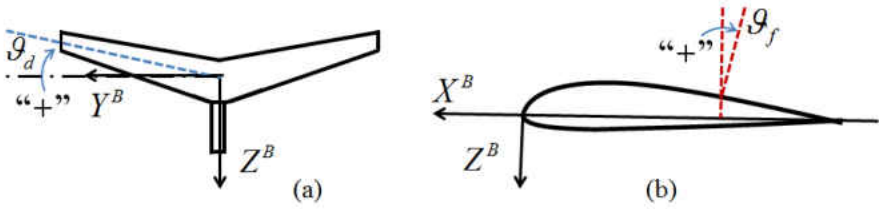

Figure 50 Dihedral angle and airfoil curve angle (a) front view, and (b) side view

Using the geometry relationship $ds_X^{WS} = dx / \cos\vartheta_f$ and assuming that the rudder has a uniformly distributed thickness $ds_X^{RS} = dx$, the moment equations can be simplified as

$$\begin{cases} \bar{m}_{WS} = b\oint_{WS}(\vec{r}_{WS} - \vec{r}_{cg}) \times (p_{WS}\hat{e}_Z^{WS} + \tau_{WS,X}\hat{e}_X^{WS} + \tau_{WS,Y}\hat{e}_Y^{WS}) \dfrac{dx}{\cos\vartheta_f} \\ \bar{m}_{RS} = hw(\bar{r}_r - \bar{r}_{cg}) \times (p_{RS}\hat{e}_Y^{RS} + \tau_{RS,X}\hat{e}_X^{RS} + \tau_{RS,Z}\hat{e}_Z^{RS}) \end{cases} \tag{54}$$

where the pressure profile (p_{WS}) and the shear profiles ($\tau_{WS,X}$ and $\tau_{WS,Y}$) on the wing surface are curve fitted using the data measured. The monotonic piecewise cubic interpolation method [38] is applied here. Since the rudder is a flat, the pressure and shear profile is assumed to be uniform.

Attitude Control and Controller Design

The attitude dynamics of the MAV in the body coordinate is given by

$$\begin{cases} \dot{\theta} = D\dot{\omega}^B \\ J\dot{\omega}^B = -\dot{\omega}^B \times (J\dot{\omega}^B) + \dot{m}^B \end{cases} \tag{55}$$

in which $\vec{\theta} = [\phi, \theta, \psi]$ is the Euler angle, $\vec{\omega}^B = [p, q, r]^T$ is the angular velocity expressed in the body coordinate, J is the moment of inertia with respect to the center of mass, $\dot{m}^B$ is the moment acting on the MAV and expressed in the body coordinate, and matrix D [57] is the relationship between the Euler angle rate and the angular velocity for a 3-2-1 rotation sequence

$$D = \begin{bmatrix} 1 & \sin\phi\tan\theta & \cos\phi\tan\theta \\ 0 & \cos\phi & -\sin\phi \\ 0 & \sin\phi\sec\theta & \cos\phi\sec\theta \end{bmatrix} \tag{56}$$

The moment $\dot{m}^B$ in Eq. (55) is a complex nonlinear function of the wind speed, attitude, and control surface deflections. Here, $\vec{u} = [\delta_{el}, \delta_{er}, \delta_r]$ is the control vector composed of the deflection angles of the left elevon, right elevon, and rudder. To achieve a control-affine model, the moment is expanded around the trimmed control vector $\vec{u}_{trim}$ for the current flight status (attitude states and wind speed) using the Taylor series expansion as

$$\dot{m}^B = \dot{m}^B\Big|_{\vec{u}=\vec{u}_{trim}} + \frac{\partial \dot{m}^B}{\partial \dot{u}}\Big|_{\vec{u}=\vec{u}_{trim}} \Delta\dot{u} + O(\Delta\dot{u}^2) \tag{57}$$

where $\Delta\vec{u} = \vec{u} - \vec{u}_{trim}$ is the difference between the current control signal $\vec{u}$ and the trimmed control signal $\vec{u}_{trim}$. Let us define $m_\delta^B = \partial\vec{m}^B / \partial\vec{u}$ as the moment derivative, and substitute Eq. (57) into Eq. (55), the following approximated control-affine model is obtained

$$\begin{cases} \dot{\vec{\theta}} = D\dot{\omega}^B \\ J\dot{\dot{\omega}}^B = -\dot{\omega}^B \times (J\dot{\omega}^B) + \dot{m}^B\Big|_{\vec{u}=\vec{u}_{trim}} + m_\delta^B\Big|_{\vec{u}=\vec{u}_{trim}} \Delta\dot{u} \end{cases} \tag{58}$$

The model in Eq. (58) is a control-affine model; however $\vec{m}^B\Big|_{\dot{u}=\dot{u}_{trim}}$ and $m_\delta^B\Big|_{\dot{u}=\dot{u}_{trim}}$ cannot be easily computed using the real-time pressure/shear information. Hence $\hat{\vec{m}}^B = \vec{m}^B\Big|_{\dot{u}(t)}$, instead of $\vec{m}^B\Big|_{\dot{u}=\dot{u}_{trim}}$, is used that can be easily computed using Eq. (54), and a nominal value $\hat{m}_\delta^B$ is used to replace $m_\delta^B\Big|_{\dot{u}=\dot{u}_{trim}}$. Thus, the nominal model used in the controller design is

$$\begin{cases} \dot{\theta} = D\omega^B \\ J\dot{\omega}^B = -\omega^B \times (J\omega^B) + \hat{m}^B + \hat{m}_\delta^B \Delta\hat{u} \end{cases} \tag{59}$$

It is worth noting that the differences between the actual and nominal models are captured by the uncertainty bounds discussed later.

In the controller design, the state vector is defined to be $\vec{x} \triangleq [\vec{x}_1, \vec{x}_2]^T = [\vec{\theta}, \vec{\omega}^B]^T$, the nominal state function is

$$\hat{\vec{f}}(x) \triangleq \begin{bmatrix} \hat{\vec{f}}_1 \\ \hat{\vec{f}}_2 \end{bmatrix} = \begin{bmatrix} D\omega^B \\ -J^{-1}\omega^B \times (J\omega^B) + J^{-1}\hat{m}^B \end{bmatrix} \tag{60}$$

the nominal input matrix is defined to be

$$\hat{g}(x) \triangleq \begin{bmatrix} \hat{g}_1 \\ \hat{g}_2 \end{bmatrix} = \begin{bmatrix} 0_{3\times 3} \\ J^{-1}\hat{m}_\delta^B \end{bmatrix} \tag{61}$$

and the output is

$$\vec{y} = \vec{h}(x) = \vec{\theta} \tag{62}$$

In the nominal model, the moment derivative $\hat{m}_\delta^B$ can be approximated by averaging the experiment or simulation data (e.g., via the Monte Carlo simulation) as

$$\hat{m}_\delta^B = \frac{1}{N}\sum_{i=1}^{N} \hat{m}_{\delta,i}^B \tag{63}$$

where N is the number of experiment or simulation samples.

The mismatches between the nominal and actual models (Eq. (55) vs. Eq. (59)) come from the following sources: 1) only a finite number of sensors are used to find the pressure/shear profiles, 2) the equivalent rectangular wing is used to approximate the delta flying-wing configuration, 3) a flat and thin rudder surface is assumed, and 4) noise associated with sensor

measurements cannot be avoided. All these mismatches are captured by the following two uncertainty bounds: the functional uncertainty bound F for the state function and the parametric uncertainty bound G for the input matrix. These two bounds are assumed to satisfy the following tow inequalities

$$\vec{\Delta}_{\dot{F}} = L_{\dot{f}}^2 \vec{h} - L_{\hat{\dot{f}}}^2 \vec{h}, \quad \left\| \Delta_{\dot{F}} \right\| \le \vec{F} \tag{64}$$

and

$$(I + \Delta_G) = [L_{\dot{g}} L_{\dot{f}} \vec{h}][L_{\hat{\dot{g}}} L_{\hat{\dot{f}}} \vec{h}]^+, \quad \left\| \Delta_G \right\| \le G < 1 \tag{65}$$

where "L" refers to the Lie derivative, $\vec{\Delta}_{\dot{F}}$ and Δ_G are the difference of the Lie derivatives between the nominal and true model, $\dot{F}$ and G represent the parametric uncertainty bounds, '$\| \ \|$' denotes the element by element absolute operator, and "+" denotes the pseudo-inverse operation. The Lie derivatives in Eqs. (64) and (65) are simplified as

$$\begin{cases} L_{\bar{\dot{f}}} \bar{h} = \begin{bmatrix} \dfrac{\partial \bar{h}}{\partial \bar{\theta}} & \dfrac{\partial \bar{h}}{\partial \bar{\omega}} \end{bmatrix} \begin{bmatrix} \bar{f}_1 \\ \bar{f}_2 \end{bmatrix} = \bar{\dot{f}}_1 \\ L_{\hat{\bar{\dot{f}}}} \hat{\bar{h}} = \begin{bmatrix} \dfrac{\partial \hat{\bar{h}}}{\partial \hat{\bar{\theta}}} & \dfrac{\partial \hat{\bar{h}}}{\partial \hat{\bar{\omega}}} \end{bmatrix} \begin{bmatrix} \hat{\bar{f}}_1 \\ \hat{\bar{f}}_2 \end{bmatrix} = \hat{\bar{\dot{f}}}_1 \end{cases} \tag{66}$$

$$\begin{cases} L_{\bar{\dot{f}}}^2 \bar{h} = L_{\bar{\dot{f}}}(L_{\bar{\dot{f}}} \bar{h}) = L_{\bar{\dot{f}}} \bar{f}_1 = \begin{bmatrix} \dfrac{\partial \bar{f}_1}{\partial \bar{\theta}} & \dfrac{\partial \bar{f}_1}{\partial \bar{\omega}} \end{bmatrix} \begin{bmatrix} \bar{f}_1 \\ \bar{f}_2 \end{bmatrix} = D_{11} \bar{f}_1 + D \bar{f}_2 \\ L_{\hat{\bar{\dot{f}}}}^2 \hat{\bar{h}} = L_{\hat{\bar{\dot{f}}}}(L_{\hat{\bar{\dot{f}}}} \hat{\bar{h}}) = L_{\hat{\bar{\dot{f}}}} \hat{f}_1 = \begin{bmatrix} \dfrac{\partial \hat{\bar{f}}_1}{\partial \hat{\bar{\theta}}} & \dfrac{\partial \hat{\bar{f}}_1}{\partial \hat{\bar{\omega}}} \end{bmatrix} \begin{bmatrix} \hat{\bar{f}}_1 \\ \hat{\bar{f}}_2 \end{bmatrix} = \tilde{D}_{11} \hat{\bar{f}}_1 + \tilde{D} \hat{\bar{f}}_2 \end{cases} \tag{67}$$

and

$$\begin{cases} L_{\bar{g}}L_{\bar{f}}\bar{h} = L_{\bar{g}}(L_{\bar{f}}h) = L_{\bar{g}}\bar{f}_1 = \begin{bmatrix} \dfrac{\partial \bar{f}_1}{\partial \bar{\theta}} & \dfrac{\partial \bar{f}_1}{\partial \bar{\omega}} \end{bmatrix} \begin{bmatrix} \bar{g}_1 \\ \bar{g}_2 \end{bmatrix} = D\bar{g}_2 \\ L_{\hat{\bar{g}}}L_{\hat{\bar{f}}}\hat{\bar{h}} = L_{\hat{\bar{g}}}(L_{\hat{\bar{f}}}\hat{\bar{h}}) = L_{\hat{\bar{g}}}\hat{\bar{f}}_1 = \begin{bmatrix} \dfrac{\partial \hat{\bar{f}}_1}{\partial \hat{\bar{\theta}}} & \dfrac{\partial \hat{\bar{f}}_1}{\partial \hat{\bar{\omega}}} \end{bmatrix} \begin{bmatrix} \hat{\bar{g}}_1 \\ \hat{\bar{g}}_2 \end{bmatrix} = \tilde{D}\hat{\bar{g}}_2 \end{cases} \tag{68}$$

where $D_{11} \triangleq \partial \bar{f}_1 / \partial \bar{\theta}$, $\tilde{D}_{11} \triangleq \partial \hat{\bar{f}}_1 / \partial \hat{\bar{\theta}}$, and $\tilde{D} = D\big|_{\dot{\theta}=\hat{\theta}}$.

In this paper, bounds $\dot{F}$ and G are found through the Monte Carlo simulation. In each of the Monte Carlo runs, the free stream wind speed, Euler angles, angular velocity, and control surface deflections are randomly chosen within certain ranges around the nominal values. The uncertainty bounds, $\dot{\Delta}_{\dot{F}}^{(i)}$ and $\Delta_G^{(i)}$, can be calculated for each Monte Carlo run (denoted by the superscript "(*i*)"). After all the Monte Carlo runs are finished, the control derivative $\hat{m}_\delta^B$, and bounds $\dot{F}$ and G can be found numerically via Eq. (63), (64) and (65), respectively.

A nonlinear robust controller in [42] is customized as

$$\Delta\vec{u} = \left[L_{\hat{\bar{g}}}L_{\hat{\bar{f}}}\vec{\bar{h}} \right]^{+} \left[\ddot{\vec{y}}_d - L_{\hat{\bar{f}}}^2\hat{\bar{h}} + \vec{\lambda}_{-1} \circ \vec{e} + \vec{\lambda}_0 \circ \dot{\vec{e}} + \vec{k} \circ \vec{s} \right] \tag{69}$$

in which the gain is calculated using

$$\dot{k} \circ \dot{s} = (I_{3\times 3} - G)^{-1} \left[\dot{F} + G \left\| \frac{d^2\dot{y}_d}{dt^2} - L_{\hat{\bar{f}}}^2\dot{\hat{h}} + \dot{\lambda}_{-1} \circ \dot{e} + \dot{\lambda}_0 \circ \ddot{e} \right\| + \dot{\eta} \circ \dot{s} \right] \tag{70}$$

where "$\circ$" denotes the element-wise multiplication operation, $I_{3\times 3}$ is a three by three identity matrix, $\vec{s}$ is defined as $\vec{s} = \vec{\lambda}_{-1} \circ \int \vec{e}dt + \vec{\lambda}_0 \circ \vec{e} + \dot{\vec{e}}$, $\vec{e} = \vec{y}_d - \vec{y} = \vec{\theta}_d - \vec{\theta}$ is the error between the desired and actual values, $\vec{\lambda}_{-1}$, $\vec{\lambda}_0$ and η are positive control parameters to guarantee the asymptotically stability. The stability and robustness proof can be found in [20]. The main

advantage of this controller is its ability in mitigating the chattering phenomenon.

Simulation Results

Due to the fact that several techniques, such as the flow sensor that can simultaneously measure pressure and shear information, are still under development, a simulation environment is investigated in this paper to demonstrate the advantages of new MAV concept and associated three-axis attitude control method.

Compared with the block diagram used in real flight (Figure 46), a flow simulation block is added in the simulated environment to approximate the pressure and shear profiles, as is shown in Figure 51. Specifically, the pressure profile is computed using AVL® [54], while the shear stress is simulated using the model for Newtonian fluid described in [58]. It is worth noting that there are differences between the simulated and real flow fields. First, the pressure in low Reynolds number flights, predicted using the state-of-the-art computational fluid design software such as the lattice vortex model based method [59], are not accurate. Second, to the best knowledge of the authors, there is no software or algorithm can accurately predict the shear stress acting on each point of the MAV surface under turbulent flow conditions. However the purpose of validating the new MAV concept will not be affected by the accuracy of the simulated flow condition.

All the simulations are conducted using MATLAB (R2010a) running in a desktop computer with 2.67 GHz intel(R) i7 Core and 8 GB of RAM. The simulation operates at 10 Hz. The computational cost of the proposed MAV concept mainly comes from the following three subroutines: pressure/shear information reading and data transmission, moment calculation, and control command generation. The measurement update rate of the pressure sensor BMP085 [49]

can be as high as 128 Hz, and if FPGA is used and data are read in parallel, a set of measurements from all the sensors can be obtained every 8 milliseconds. For the 42-sensor configuration used in this paper, it takes the software roughly 2 milliseconds in computing the moments. The control command can be generated within 0.7 milliseconds. It is worth mentioning that as the number of sensors increases, the computational cost will not increase noticeably, because only the moment calculation subroutine will be slightly influenced by the number of sensors while the CPU time used in sensor reading and control command calculation will not be affected much.

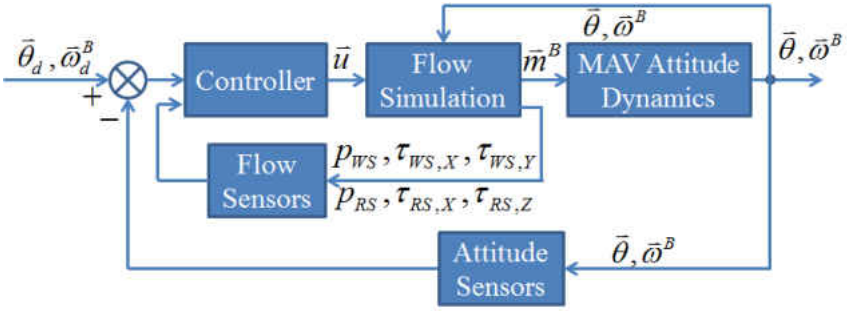

Figure 51 Block diagram of the attitude control system in a simulated environment

The mismatches between the nominal model used in the nonlinear robust controller design and the true attitude model come from the following sources: (a) the pressure/shear information measured using a finite number of sensors along the MAC is used to represent the pressure/shear profiles over the MAV surfaces and calculate the moments acting on the MAV; and (b) the nominal state function and input matrix are different from those in the actual model.

To quantify the mismatch between the actual moment acting on the MAV and the numerically integrated one using a finite number of sensors along the MAC, a Monte Carlo

simulation with 500 runs is conducted. The free stream wind speed V_∞ is randomly chosen from a uniform distribution within a range of [5, 25] *m/s*, and the angle of attack is randomly chosen from a uniform distribution within [-5, 25] degrees. δ_{el} and δ_{er} are uniformly distributed in [-5, 35] degrees, while δ_r is randomly chosen from a uniformly distribution of [-25, 25] degrees.

The actual moment acting on the MAV is simulated using the following steps. First in AVL®, 660 horseshoe vortices that follow a cosine distribution in both the span-wise and chord-wise directions are placed on the wing, and 25 vortices are evenly distributed on the rudder surface. Second, since the air velocity on every point is not known in the simulated environment, the shear distribution is assumed to be uniform and Newtonian, and can be simulated using the equation $\tau = 0.5\rho V_\infty^2 C_f$, where $C_f = 0.664/\sqrt{\mathrm{Re}}$ is the local skin friction coefficient [58]. The Reynolds number is $\mathrm{Re} = \rho V_\infty L/\mu$, where the air density is $\rho =$ 1.225 kg/m^3, the dynamic viscosity is $\mu = 1.789\times10^{-5} kg/m\cdot s$, and L is the characteristic traveled length.

The mismatches between the actual moments and the ones calculated from a finite number of sensor measurements are shown in Figure 52. It can be seen that the differences in the roll, pitch and yaw directions fall into a range of [-0.006, 0.006] $N\cdot m^2$, [-0.015, 0.015] $N\cdot m^2$, and [-0.012, 0.012] $N\cdot m^2$, respectively. The mismatches are about 5% of the actual moments.

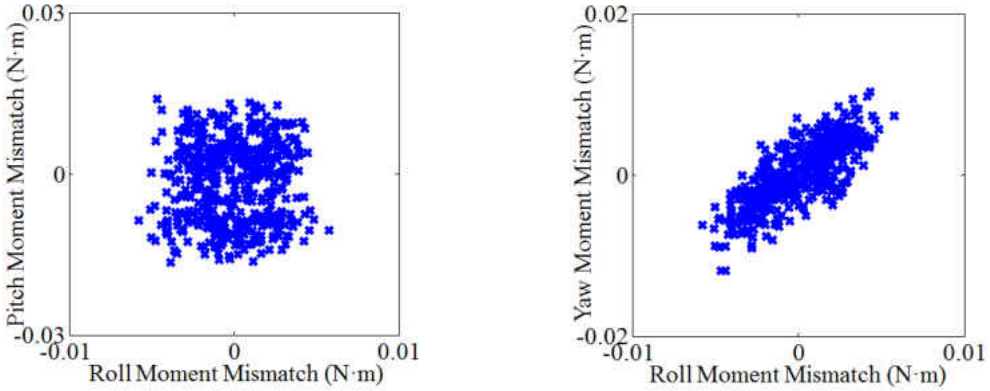

(a) mismatches in roll and pitch moments (b) mismatches in roll and yaw moments

Figure 52 Comparisons of the moments calculated using a large number of nodes in AVL and the ones calculated from the simulated sensors

The uncertainties between the nominal and actual state function and input matrix in Eqs. (64) and (65) are quantified here. Using the same setting shown above, the mismatches in the state function $\Delta_{\dot{F}}$ and the input matrix Δ_G are show in Figure 53 and Figure 54, respectively. The nominal control derivative $\hat{m}_\delta^B$, nominal state function bound $\bar{F}$, and nominal input matrix bound G are found to be $\hat{m}_\delta^B = \begin{bmatrix} 0.2009 & 0.0001 & 0.0052 \\ -0.0002 & 0.2930 & 0.0000 \\ -0.0630 & 0.0000 & 0.0497 \end{bmatrix}$, $\bar{F} = \begin{bmatrix} 0.15 & 0.25 & 0.3 \end{bmatrix}^T$, and $G = \begin{bmatrix} 0.08 & 0.25 & 0.60 \\ 0.20 & 0.04 & 0.25 \\ 0.08 & 0.20 & 0.45 \end{bmatrix}$, respectively. In the simulated environment, the nominal control derivative $\hat{m}_\delta^B$ is found by averaging the results from a Monte-Carlo simulation and it is assumed to be constant. Practically, this value can be found through wind tunnel experiments or flight tests. If $\hat{\bar{m}}_\delta^B$ is significantly different for different flight conditions, a gain scheduling technique can be used so that the uncertainty bound can be reduced and the control performance can be less

conservative. Since the bounds $\dot{F}$ and G obtained from the Monte Carlo simulation are typically very conservative, smaller bounds, guided by the calculated conservative bounds, are used instead to get a better closed-loop performance.

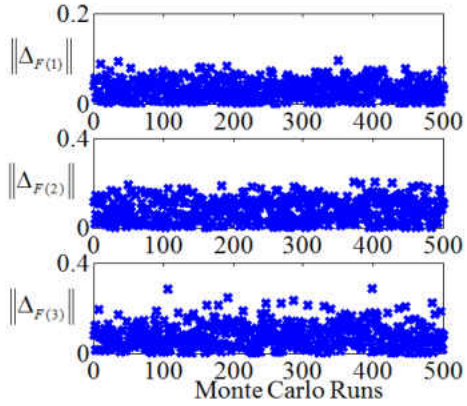

Figure 53 The mismatches between the nominal and actual state functions

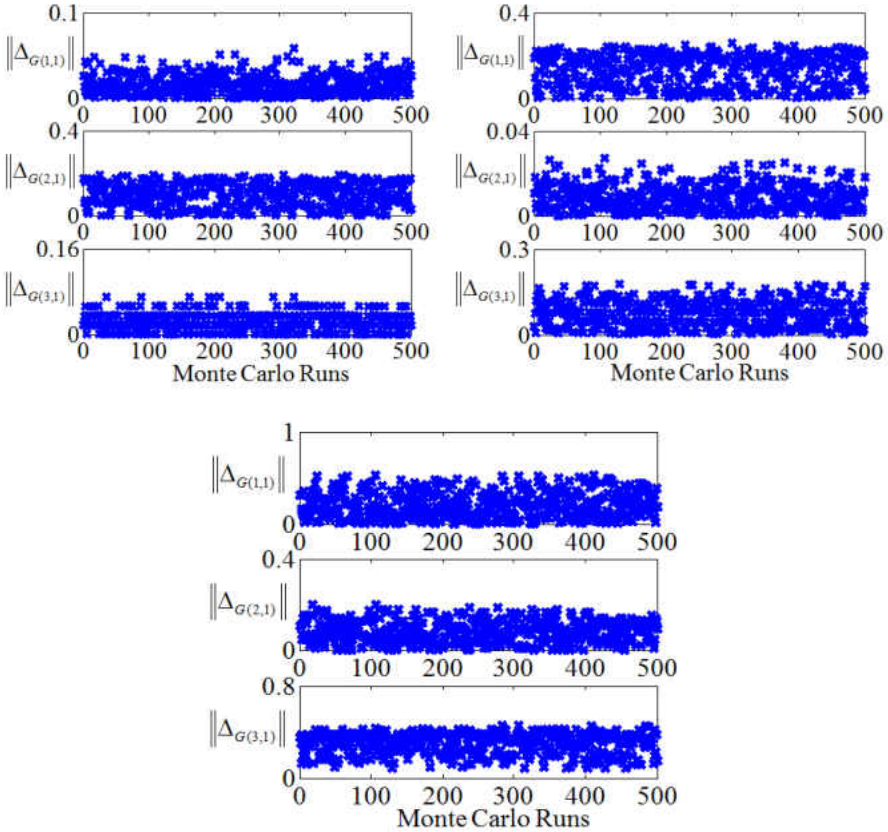

Figure 54 The mismatches between the nominal and actual input matrices

To verify the effectiveness of the system, it is tested under various conditions, Case I: Steady wind condition; Case II: Turbulent wind condition; Case III: Turbulent wind with airflow separation. In Case I, the MAV is flying at a constant free steam wind speed of $V_\infty = 20\,\text{m/s}$. According to the commercial barometric air pressure sensor BMP085 [49], the noise on the pressure measurement is a Gaussian with a zero mean and a standard deviation of $\sigma = 3Pa$, and assumed to be bounded by 3σ. Based on [60], the Euler angle measurement noise is a Gaussian with a zero mean and a standard deviation of 0.2 degrees, and is assumed to be bounded in [-0.6, 0.6] degrees. Similarly, the measurement noise on the angular rate is a Gaussian with a zero mean and a standard deviation of 0.01 deg/s, but assumed to be bounded in [-0.03, 0.03] deg/s. The controller parameters are tuned to be $\vec{\lambda}_{-1} = [0.1, 0.1, 0]^T$, $\vec{\lambda}_0 = [1, 0.4, 1]^T$, and $\vec{\eta} = [4, 4, 4]^T$. The results of two simulation cases are shown below: In Case I, the attitude is controlled from $\vec{\theta}_0 = [0, 5, 0]$ degrees to $\vec{\theta}_d = [0, 10, 6]$ degrees, and in Case II, the attitude is controlled from $\vec{\theta} = [10, 20, 10]$ to $\vec{\theta}_d = [0, 4, 0]$. The closed-loop attitude performance and the control signal applied to the system for these two cases are shown in Figure 55 and Figure 56, respectively. It can be seen that the MAV can track the attitude command using the pressure/shear information, with a small lateral damping within a range of [-1, 1] degrees and a settling time of 5 seconds.

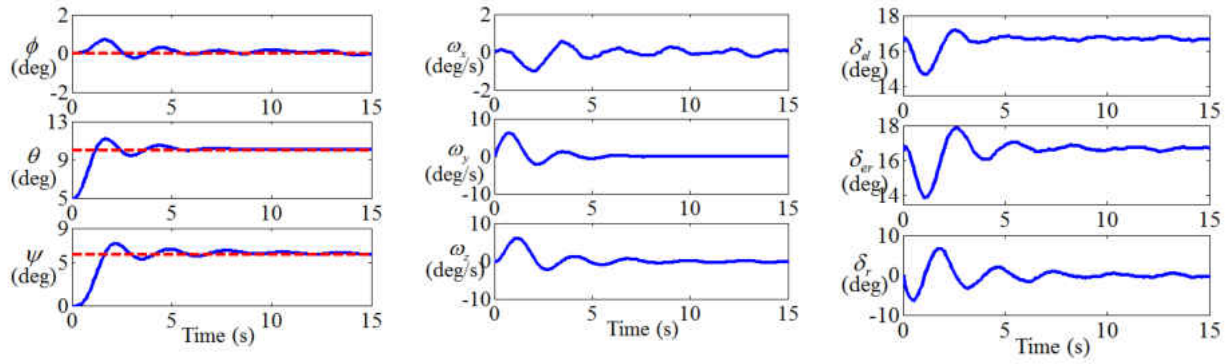

(a) attitude profile (b) angular rate profile (c) control signal profile

Figure 55 Attitude control under a steady flow condition (Case I)

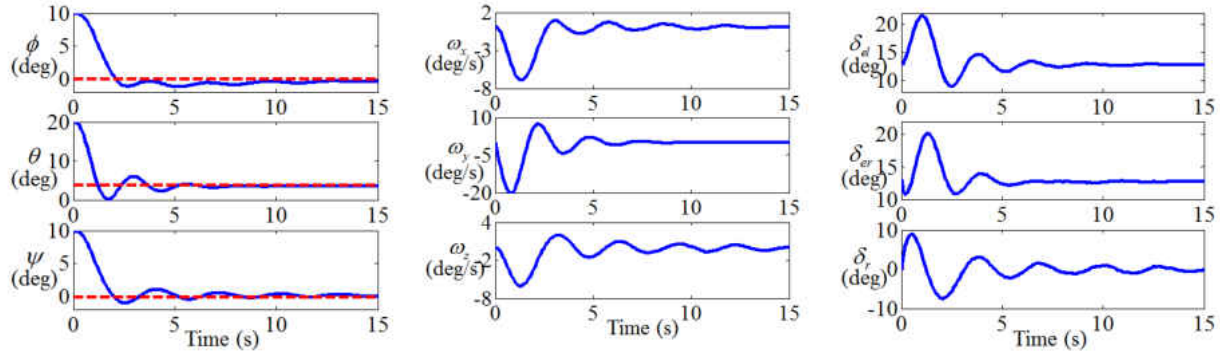

(a) attitude profile (b) angular rate profile (c) control signal profile

Figure 56 Attitude control under a steady flow condition (Case II)

In Case II, to show the effectiveness of the pressure/shear information augmented attitude control system, a turbulent wind is simulated by adding a strong Gaussian noise to the wind velocity. The wind speed is assumed to be a Gaussian distribution with a mean value of 20 m/s and a standard deviation of 2 m/s. Also there are wind disturbances in the Y^B and Z^B axes (a zero mean Gaussian noise with a standard deviation of 2 degrees in the pitching direction and 2 degrees in the yaw direction), which are represented by v_p and v_s respectively. All the other settings including the control parameters are the same as those of the steady wind condition. The results of two simulation cases are shown below: In Case I the attitude is controlled from

$\vec{\theta}_0 = [0,5,0]$ degrees to $\vec{\theta}_d = [0,10,6]$ degrees, and in Case II the attitude is controlled from $\vec{\theta} = [10,20,10]$ degrees to $\vec{\theta}_d = [0,4,0]$ degrees. The simulation results are shown in Figure 57 and Figure 58, respectively. Figure 57(a) and Figure 58(a) show the attitude performance, where the solid line refers to the actual attitude and the dashed lines refer to the desired value. In both simulation cases, the attitude can be controlled to desired value within a rising time of 1.5 seconds, with a settling time of 3 seconds and a small lateral damping winthin 2 degrees.

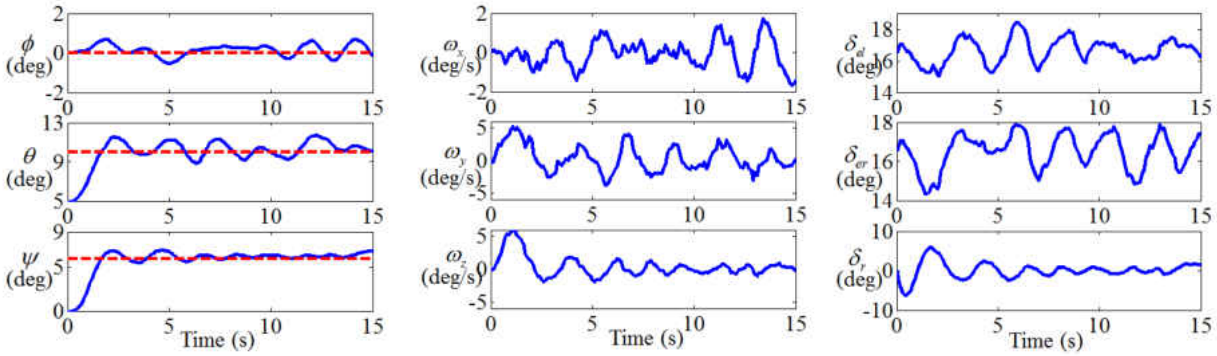

(a) attitude profile (b) angular rate profile (c) control signal profile

Figure 57 Attitude control under turbulent flow condition (Case I)

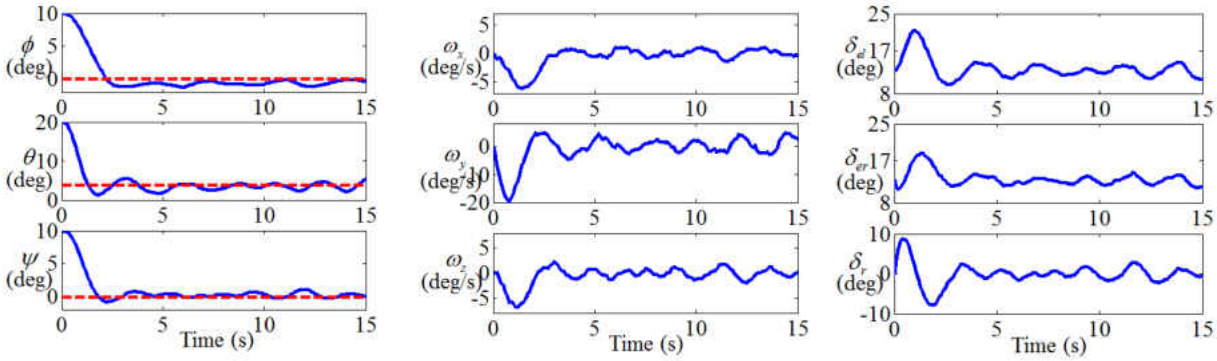

(a) attitude profile (b) angular rate profile (c) control signal profile

Figure 58 Attitude control under turbulent flow condition (Case II)

In Case III, the proposed attitude control system is tested in a simulated turbulent condition with flow separations. The simulated turbulence is simulated to that of Section V.D. The flow separation is simulated through adding a uniformly distributed noise to the sensor couples 6-10 on both sides of the wing and the sensor couple on the rudder, considering the fact that the flow may separates easily on the half wing towards the trailing edge. The simulated flow separation is added to the system at a frequency of 5 Hz, with amplitude of twice the nominal pressure and shear stresses. The closed-loop system performance is shown in Figure 59. As it can be seen, even in such a complex flow condition, the MAV is still stable, although the settling time is longer as compared with those of the steady wind condition.

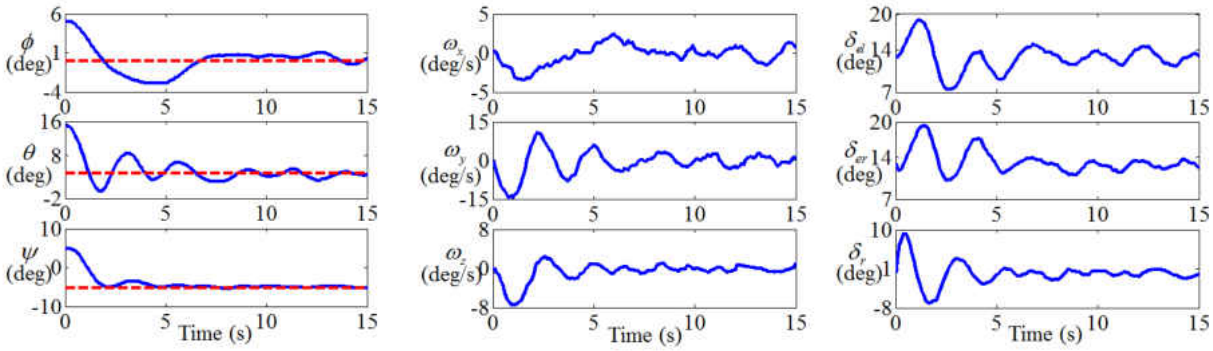

(a) attitude profile (b) angular rate profile (c) control signal profile

Figure 59 Attitude control under turbulent conditions with flow separations

It's obvious that both the novel sensing strategy and the robust controller design contribute to the stable performance of MAV in complex flow conditions. To further demonstrate the benefit of incorporating pressure/shear information in the MAV attitude control, two additional simulations under exactly the same turbulence and flow separation conditions are conducted. In Case I, it is assumed that the nominal pressure and shear information are known for different flow conditions through extensive wind tunnel and flight experiments, but real-time

turbulence and sudden flow separations are not known. This test scenario can be used to mimic the gain scheduling control method in which the nominal moment coefficients are known. In Case II, it is assumed that no pressure and shear information is available and only the rigid body motion information (e.g. the Euler angle) can be measured. The results for these two simulation cases are shown in Figure 60 and Figure 61, respectively. It is shown in the mimicked gain scheduling approach (Figure 60) that a stable result can be obtained but the settling time is much longer and the lateral damping is much higher than those of the proposed method. It is worth noting that this stable performance is based on the assumption that the nominal moment coefficients are precisely predicted. If no flow information is known (in Figure 61), the closed-loop system is unstable in the simulated turbulence condition with flow separations.

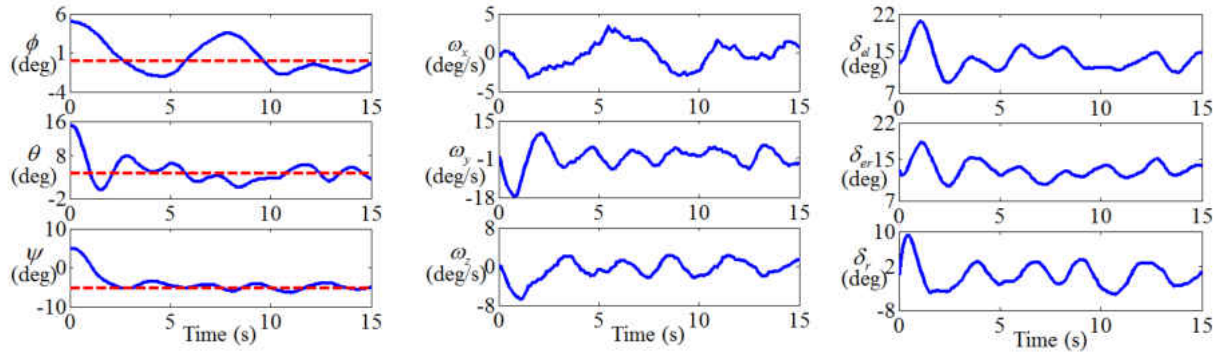

(a) attitude profile (b) angular rate profile (c) control signal profile

Figure 60 Attitude control under turbulent and separated flow with patial sensing capabilities

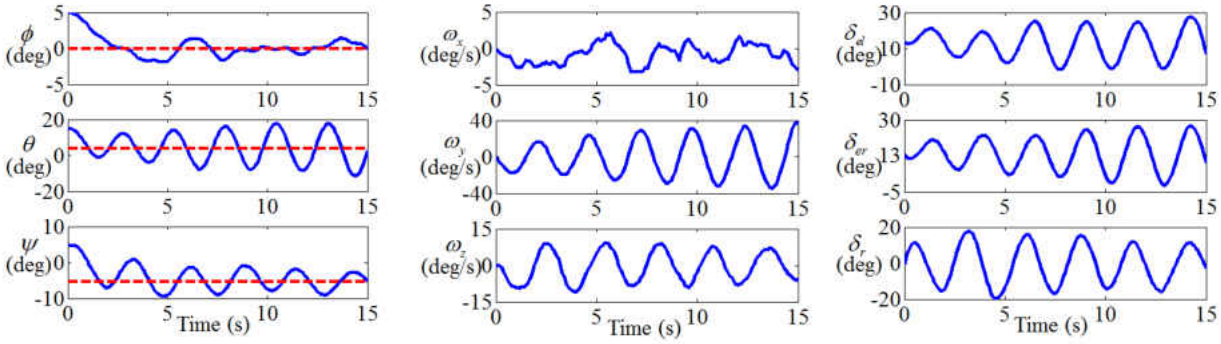

(a) attitude profile (b) angular rate profile (c) control signal profile

Figure 61 Attitude control under turbulent and separated flow without sensing capability

CHAPTER FIVE: FAULT TOLERANT CONTROL

In chapters 2 and 3, pitching control of a straight uniform wing is demonstrated in both simulation and wind tunnel tests, and the three-axis attitude control for a MAV is shown in Chapter 4. All the previous studies are based on an assumption that all the sensors work during flights. However, since there are many airflow sensors onboard and many cables are involved, the chance of sensor failures is not small. Therefore, an attitude controller that is adaptive or robust with respect to sensor failures needs to be studied. One efficient approach in dealing with hardware failure is to add redundant devices. However, hardware redundancy is not a viable option for MAVs because of its stringent power, size, and weight limitations. This chapter will show a robust adaptive control strategy to deal with sensor failure scenarios.

Traditionally, the MAV's attitude motion model is inherited from that of bigger airplanes. As shown in Figure 62(a), the attitude control system is normally composed of feedback loops, and the attitude information is measured using rigid-body sensors such as inertial measurement unit and vision sensors. Figure 62(b) shows the attitude control system in [50, 61], in addition to the rigid-body attitude feedback signal, the airflow measurements over the body surface also feedback into the controller to achieve better performance. In this system, the moment is purely calculated from the sensor measurements by assuming that all the sensors work well in the flight. If some of sensors fail, the moment calculation will be varied from the true value. Hence, to enable the fault tolerant capability of the flight control system, an updated structure needs to be designed so that the true moment can be estimated in real-time during flight. Figure 62(c) shows the structure of the robust adaptive controller, in which the "mapping structure update" block relates the airflow information and the aerodynamic forces/moments.

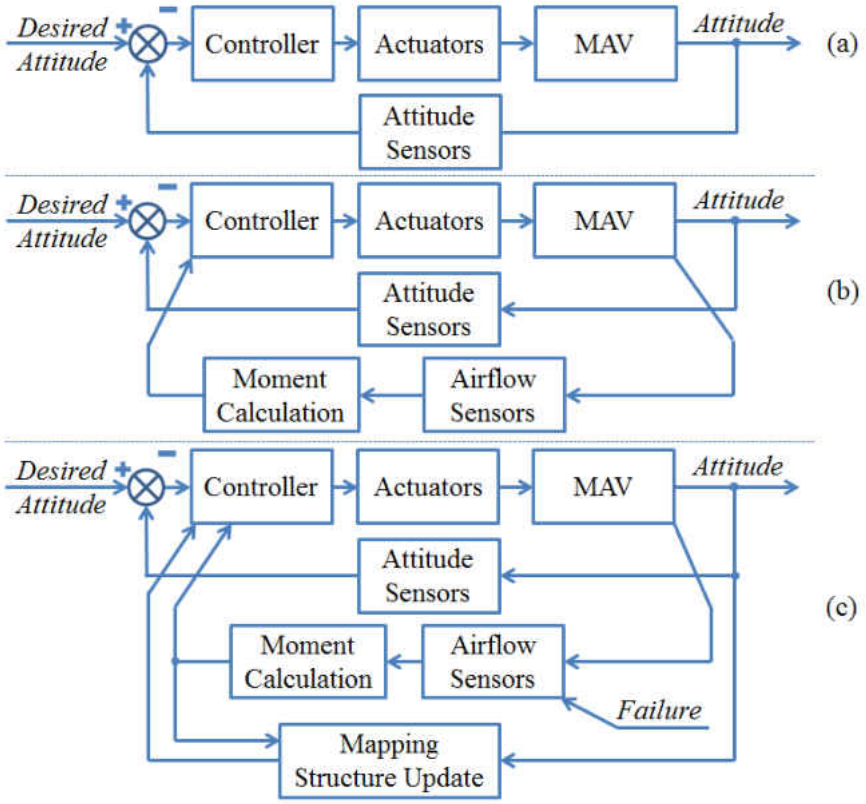

Figure 62 Development of attitude control systems (a) traditional method, (b) method with airflow (pressure and shear) feedback, and (c) method with fault tolerance

Traditionally, the fault tolerant control systems are classified into mainly two categories, passive methods and active methods [62-64]. In passive methods, the potential failure modes are assumed to be known and considered together with the nominal operating conditions in the control design process; while the active methods react to system failures by reconfiguring the controller based on the information from fault detection system to maintain acceptable performance. The fault tolerant attitude control of this paper belongs to the active methods. The advantages of this method are as follows, first, it does not depend on fault detection for actions; second, it can deal with not only the inaccuracy in moment calculation caused by sensor failure but also from error in the approximation itself.

The rest of this chapter is organized as follows, firstly, the moment calculation from the raw measurement is formulated, and the sensor placement is formulated as a constrained optimization problem; secondly, the attitude control modeling is derived; thirdly, the robust and adaptive fault tolerant controller is derived with and the stability of which is proved; and finally, the simulation results are given.

Airflow Sensing and Moment Mapping

Two coordinate systems, including the body coordinate $O^B X^B Y^B Z^B$ and the local surface coordinate $O_i^S X_i^S Y_i^S Z_i^S$ at the location of surface element i, are used in the aerodynamic moment analysis as shown in Fig. 1. In the body coordinate, axis X^B points forward towards the nose, axis Y^B points to the right wing, and axis Z^B points downward defined by the right hand rule. The surface coordinate is defined in accordance with the sensor. $O^B X^B Y^B Z^B$ In Figure 63, "C.G." refers to the center of gravity $\boldsymbol{r}_{cg}$, $\boldsymbol{r}_i$ is the position vector of the surface element i, and p_i, $\tau_{x,i}$, and $\tau_{y,i}$ are the pressure, shear stresses along the three axes of the local surface coordinate respectively.

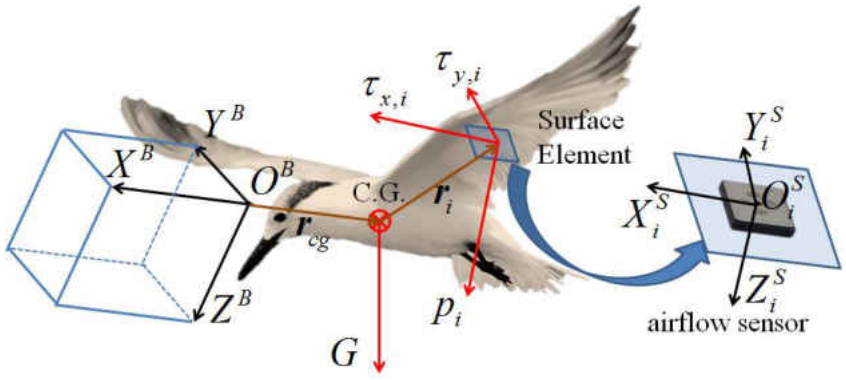

Figure 63 Pressure and shear stresses on an arbitrary surface element

Let us assume that N_S sensors can approximate the air flow on a MAV surface. Thus, the aerodynamic moment can be calculated using

$$\hat{\boldsymbol{m}}_f = \sum_{i=1}^{N_S} s_i \left(\boldsymbol{r}_i \times (R_i \cdot \boldsymbol{q}_i) \right) \tag{71}$$

in which s_i is the area of surface element governed by sensor i; as $N_S \to \infty$, $s_i \to ds$ (the deferential unit) Otherwise, s_i is approximately the area between successive sensors. $\boldsymbol{q}_i = [\tau_{x,i}, \tau_{y,i}, p_i]^T$ is the sensor measurements, R_i is the rotational matrix from the local surface coordinate $O_i^S X_i^S Y_i^S Z_i^S$ to the MAV body frame $O^B X^B Y^B Z^B$, and $\boldsymbol{r}_i = [r_{i,1}, r_{i,2}, r_{i,3}]^T$ is expressed in the body coordinate system. Let us define a skew-symmetric matrix

$$P_i \triangleq \begin{bmatrix} 0 & -r_{i,3} & r_{i,2} \\ r_{i,3} & 0 & -r_{i,1} \\ -r_{i,2} & r_{i,1} & 0 \end{bmatrix}, \tag{72}$$

, and Eq. (71) becomes

$$\hat{\boldsymbol{m}}_f = \sum_{i=1}^{N_S} s_i P_i R_i \boldsymbol{q}_i = M_f \boldsymbol{q}_f \tag{73}$$

where $M_f = [s_1 P_1 R_1, \cdots, s_{N_S} P_{N_S} R_{N_S}] \in \mathbb{R}^{3 \times 3N_S}$, $\boldsymbol{q}_f = [\boldsymbol{q}_1^T, \cdots, \boldsymbol{q}_{N_S}^T]^T \in \mathbb{R}^{3N_S \times 1}$, $\boldsymbol{q}_i$ is composed of all the measured shear and pressure information. M_f is a function of the geometrical configuration and the control surface deflections, all the entries in M_f are calculated offline except the contributions from the airflow sensors installed on the control surfaces. Here, the area elements s_i and the skew-symmetric matrix P_i, $i = 1, \cdots, N_S$, are constants and predefined once the sensor layout is determined. The calculation of the direct cosine matrix R_i is shown in Figure 64 for

three cases. Case 1: for the wing surface element, R_i is obtained from two rotations, firstly through a rotation around the X^B axis by the dihedral angle ϑ_d, and then a second rotation of ϑ_f about the Y^B axis. Case 2: for the surface elements on the elevon, the rotations are the same as that of the wing surface case except that the angle in the second rotation is $\vartheta_f + \delta_e$, where δ_e is the angle of the elevon. Case 3: for the rudder surface elements, the direct cosine matrix R_i can be achieved by rotating the local surface around the Z^B axis for the rudder deflection angle δ_r. Hence, R_i is given as

$$R_i = \begin{cases} R_{Y^B}(\vartheta_{f,i}) R_{X^B}(\vartheta_d) & \text{if } s_i \in W \\ R_{Y^B}(\vartheta_{f,i} + \delta_e) R_{X^B}(\vartheta_d) & \text{if } s_i \in E \\ R_{Z^B}(\delta_r) & \text{if } s_i \in R \end{cases} \tag{74}$$

where W, E, and R refer to the wing surface, elevon surface, and rudder surface, respectively. R_{X^B}, R_{Y^B}, and R_{Z^B} are the single axis rotation matrices given as

$$R_{X^B}(\vartheta) = \begin{bmatrix} 1 & 0 & 0 \\ 0 & \cos(\vartheta) & \sin(\vartheta) \\ 0 & -\sin(\vartheta) & \cos(\vartheta) \end{bmatrix}, \quad R_{Y^B}(\vartheta) = \begin{bmatrix} \cos(\vartheta) & 0 & -\sin(\vartheta) \\ 0 & 1 & 0 \\ \sin(\vartheta) & 0 & \cos(\vartheta) \end{bmatrix}, \text{ and}$$

$$R_{Z^B}(\vartheta) = \begin{bmatrix} \cos(\vartheta) & \sin(\vartheta) & 0 \\ -\sin(\vartheta) & \cos(\vartheta) & 0 \\ 0 & 0 & 1 \end{bmatrix}, \text{ respectively.}$$

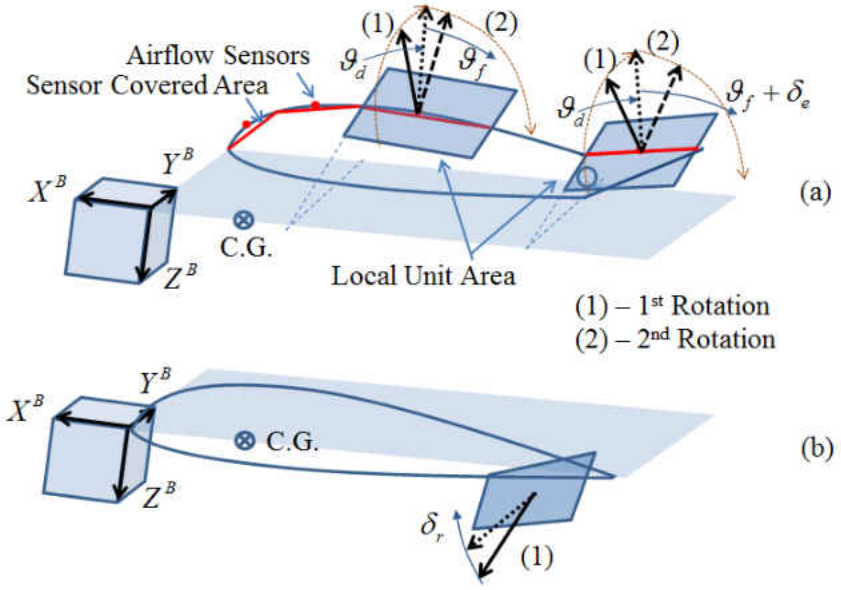

Figure 64 Calculation of the local rotation matrices

Attitude Motion Model with an Airflow Sensor Array

The attitude dynamics of the MAV in the body frame [57] is given by

$$\begin{cases} \dot{\boldsymbol{\theta}} = D\boldsymbol{\omega} \\ J\dot{\boldsymbol{\omega}} = -\boldsymbol{\omega} \times (J\boldsymbol{\omega}) + \boldsymbol{m} \end{cases} \tag{75}$$

in which $\boldsymbol{\theta} = [\phi, \theta, \psi]^T \in \mathbb{R}^{3\times 1}$ is the Euler angle, $\boldsymbol{\omega} = [p, q, r]^T \in \mathbb{R}^{3\times 1}$ is the angular velocity in the body frame, and matrix D is the relationship between the Euler angle rate and the angular velocity in the body frame

$$D = \begin{bmatrix} 1 & \sin\phi\tan\theta & \cos\phi\tan\theta \\ 0 & \cos\phi & -\sin\phi \\ 0 & \sin\phi\sec\theta & \cos\phi\sec\theta \end{bmatrix} \tag{76}$$

$J \in \mathbb{R}^{3\times 3}$ is the moment of inertia of the MAV, and $\boldsymbol{m}$ is the actual aerodynamic moment. To obtain a control affine model, through the Taylor series expansion, Eq. (5) is written as

$$\begin{cases} \dot{\boldsymbol{\theta}} = D\boldsymbol{\omega} \\ J\dot{\boldsymbol{\omega}} = -\boldsymbol{\omega} \times (J\boldsymbol{\omega}) + \boldsymbol{m}_f^0 + B^0\boldsymbol{u} \end{cases} \tag{77}$$

Here $B^0 \in \mathbb{R}^{3\times3}$ is the control derivative, evaluated at current flight states and trimmed deflection angles of the control surfaces. It is worth noting that $\boldsymbol{u}$ is small disturbance control from the trimmed value and is modeled as

$$\boldsymbol{u} = H(\boldsymbol{\delta} - \boldsymbol{\delta}_{trim}) \tag{78}$$

where $\boldsymbol{\delta} = [\delta_{el}, \delta_{er}, \delta_r]^T$ is the control surface deflection angles, and $\boldsymbol{\delta}_{trim}$ is the trim angles of the control surfaces. δ_{el}, δ_{er} and δ_r are the deflection angles of the left elevon, right elevon and rudder, respectively. To make the input matrix B diagonal, H is a transformation matrix defined as

$$H = \frac{1}{2}\begin{bmatrix} -1 & 1 & 0 \\ 1 & 1 & 0 \\ 0 & 0 & 2 \end{bmatrix} \tag{79}$$

From the definition of H in Eq. (79), the control input matrix B becomes diagonally dominant. Since $\boldsymbol{m}_f^0$ is not easy to be calculated and it may vary for different trim conditions, the real-time aerodynamic moment is used in the nominal model as

$$\begin{cases} \dot{\boldsymbol{\theta}} = D\boldsymbol{\omega} \\ J\dot{\boldsymbol{\omega}} = -\boldsymbol{\omega} \times (J\boldsymbol{\omega}) + \hat{\boldsymbol{m}}_f + \boldsymbol{\eta} + B\boldsymbol{u} \end{cases} \tag{80}$$

where $B = diag([B_{11}^0, B_{22}^0, B_{33}^0])$, $\boldsymbol{\eta} \in \mathbb{R}^{3\times1}$ is a compensator, which is composed of three parts (1) the mismatches between $\boldsymbol{m}_f^0$ and $\hat{\boldsymbol{m}}_f$, (2) the mismatch of using $B\boldsymbol{u}$ to replace $B^0\boldsymbol{u}$, and (3) moment drifting caused by sensor failures.

Fault Tolerant Control Design

Let us define $\boldsymbol{e}_1 = \boldsymbol{\theta} - \boldsymbol{\theta}_d$ and $\boldsymbol{e}_2 = \boldsymbol{\omega} - \boldsymbol{\omega}_d$. Then Eq. (80) is derived as

$$\begin{cases} \dot{\boldsymbol{e}}_1 = -\dot{\boldsymbol{\theta}}_d + D(\boldsymbol{e}_2 + \boldsymbol{\omega}_d) \\ \dot{\boldsymbol{e}}_2 = -\dot{\boldsymbol{\omega}}_d - J^{-1}\{(\boldsymbol{e}_2 + \boldsymbol{\omega}_d) \times [J(\boldsymbol{e}_2 + \boldsymbol{\omega}_d)]\} + J^{-1}\hat{\boldsymbol{m}}_f + J^{-1}\boldsymbol{\eta} + J^{-1}B\boldsymbol{u} \end{cases} \tag{81}$$

Considering the fact that the input matrix B is a function of the state variables, and the aerodynamic moment change is mainly captured by the sensors, the moment changes obtained by control surface changed around current state doesn't varying too much, B is assumed to be bounded around a constant matrix $\hat{B}$, given by

$$B = (I + \Delta)\hat{B} \tag{82}$$

where Δ is assumed to be bounded, diagonal matrix, and $0 \le |\Delta_{ii}| \le G_{ii}, \; i, j = 1,2,3$, and $\Delta_{ij} = 0, \; if \; i \ne j$.

Let $\hat{\boldsymbol{\eta}}$ be the estimated value of $\boldsymbol{\eta}$, and the error between them are defined as

$$\tilde{\boldsymbol{\eta}} \triangleq \hat{\boldsymbol{\eta}} - \boldsymbol{\eta} \tag{83}$$

Considering the fact that the airflow sensor fails at a much lower frequency compared to the control system sampling frequency, $\boldsymbol{\eta}$ can be assumed as an unknown constant. To simplify the derivation of the controller, let's define

$$\boldsymbol{f}_1(\boldsymbol{e}_1, \boldsymbol{e}_2) \triangleq -\dot{\boldsymbol{\theta}}_d + D(\boldsymbol{e}_2 + \boldsymbol{\omega}_d) \tag{84}$$

and

$$\boldsymbol{f}_2(\boldsymbol{e}_1, \boldsymbol{e}_2) \triangleq -\dot{\boldsymbol{\omega}}_d - J^{-1}\{(\boldsymbol{e}_2 + \boldsymbol{\omega}_d) \times [J(\boldsymbol{e}_2 + \boldsymbol{\omega}_d)]\} + J^{-1}\hat{\boldsymbol{m}}_f + J^{-1}\hat{\boldsymbol{\eta}} \tag{85}$$

Then Eq. (81) can be written in a simpler form as

$$\begin{cases} \dot{\boldsymbol{e}}_1 = \boldsymbol{f}_1(\boldsymbol{e}_1, \boldsymbol{e}_2) \\ \dot{\boldsymbol{e}}_2 = \boldsymbol{f}_2(\boldsymbol{e}_1, \boldsymbol{e}_2) - J^{-1}\tilde{\boldsymbol{\eta}} + J^{-1}B\boldsymbol{u} \end{cases} \tag{86}$$

Following the back-stepping design procedure [65], a new set of state variables are defined as

$$\begin{cases} \boldsymbol{x}_1 = \boldsymbol{e}_1 \\ \boldsymbol{x}_2 = \Gamma_1 \boldsymbol{e}_1 + \boldsymbol{f}_1(\boldsymbol{e}_1, \boldsymbol{e}_2) \end{cases} \tag{87}$$

The derivative of the state variable $\boldsymbol{x}_i, i = 1,2$ leads to

$$\begin{cases} \dot{\boldsymbol{x}}_1 = -\Gamma_1 \boldsymbol{x}_1 + \boldsymbol{x}_2 \\ \dot{\boldsymbol{x}}_2 = -\Gamma_2 \boldsymbol{x}_2 - \Gamma_3 \int_{t_0}^{t} \boldsymbol{x}_1 dt + \boldsymbol{f}(\boldsymbol{x}_1, \boldsymbol{x}_2) + \boldsymbol{h}(\boldsymbol{x}_1, \boldsymbol{x}_2)\tilde{\boldsymbol{\eta}} + \boldsymbol{g}(\boldsymbol{x}_1, \boldsymbol{x}_2)\boldsymbol{u} \end{cases} \tag{88}$$

where Γ_1, Γ_2, and Γ_3 are positive diagonal matrices, they define the decreasing rate of states $\boldsymbol{x}_1$ and $\boldsymbol{x}_2$. $\boldsymbol{f}(z_1, z_2)$, $\boldsymbol{g}(z_1, z_2)$, and $\boldsymbol{h}(z_1, z_2)$ are defined as follows,

$$\begin{cases} \boldsymbol{f}(\boldsymbol{x}_1, \boldsymbol{x}_2) \triangleq \Gamma_2 \boldsymbol{x}_2 + \Gamma_3 \int_{t_0}^{t} \boldsymbol{x}_1 dt + \Gamma_1 \boldsymbol{f}_1(\boldsymbol{e}_1, \boldsymbol{e}_2) + \dfrac{\partial \boldsymbol{f}_1(\boldsymbol{e}_1, \boldsymbol{e}_2)}{\partial \boldsymbol{e}_1} \boldsymbol{f}_1(\boldsymbol{e}_1, \boldsymbol{e}_2) \\ \qquad\qquad + \dfrac{\partial \boldsymbol{f}_1(\boldsymbol{e}_1, \boldsymbol{e}_2)}{\partial \boldsymbol{e}_2} [\boldsymbol{f}_2(\boldsymbol{e}_1, \boldsymbol{e}_2) + J^{-1}\hat{\boldsymbol{\eta}}] \\ \boldsymbol{g}(\boldsymbol{x}_1, \boldsymbol{x}_2) \triangleq \dfrac{\partial \boldsymbol{f}_1(\boldsymbol{e}_1, \boldsymbol{e}_2)}{\partial \boldsymbol{e}_2} J^{-1} B \\ \boldsymbol{h}(\boldsymbol{x}_1, \boldsymbol{x}_2) \triangleq -\dfrac{\partial \boldsymbol{f}_1(\boldsymbol{e}_1, \boldsymbol{e}_2)}{\partial \boldsymbol{e}_2} J^{-1} \end{cases} \tag{89}$$

The derivation of Eq. (88) and Eq. (89) is shown in Appendix A.

From Eq.(88), we can see that if $\boldsymbol{x}_1 \to \boldsymbol{0}$ and $\boldsymbol{e}_1 \to \boldsymbol{0}$ and $\boldsymbol{e}_2 \to \boldsymbol{0}$, and vice versa. Therefore, instead of designing a controller for the system Eq. (86), a controller for the equivalent system in Eq.(88) is designed.

Theorem 1: If B is perfectly know and $\boldsymbol{g}(z_1, z_2)$ is invertible, if the following controller and

parameter update law are adopted

$$\boldsymbol{u} = -[\boldsymbol{g}(\boldsymbol{x}_1, \boldsymbol{x}_2)]^{-1} \boldsymbol{f}(\boldsymbol{x}_1, \boldsymbol{x}_2) \tag{90}$$

and

$$\dot{\tilde{\boldsymbol{\eta}}} = -\Gamma_\eta [\boldsymbol{h}(\boldsymbol{x}_1, \boldsymbol{x}_2)]^T \boldsymbol{x}_2 \tag{91}$$

Then, the system in Eq. (88) is globally asymptotically stable.

Proof: Choose the following Lyapunov function

$$\begin{aligned} V = & \frac{1}{2} \boldsymbol{x}_1^T \boldsymbol{x}_1 + \frac{1}{2} \boldsymbol{x}_2^T \boldsymbol{x}_2 + \frac{1}{2} \tilde{\boldsymbol{\eta}}^T \Gamma_\eta^{-1} \tilde{\boldsymbol{\eta}} + \\ & \frac{1}{2} \left(\Gamma_1^{-1/2} \Gamma_3^{1/2} \boldsymbol{x}_1 + \Gamma_1^{1/2} \Gamma_3^{1/2} \int_{t_0}^{t} \boldsymbol{x}_1 \, dt \right)^T \left(\Gamma_1^{-1/2} \Gamma_3^{1/2} \boldsymbol{x}_1 + \Gamma_1^{1/2} \Gamma_3^{1/2} \int_{t_0}^{t} \boldsymbol{x}_1 \, dt \right) \end{aligned} \tag{92}$$

Since $V = 0$ if and only if $\boldsymbol{x}_1 = \boldsymbol{x}_2 = \tilde{\boldsymbol{\eta}} = \boldsymbol{0}$ and $V > 0$ everywhere else, V is positive definite.

The derivative of this Lyapunov function is

$$\begin{aligned} \dot{V} = & \boldsymbol{x}_1^T (-\Gamma_1 \boldsymbol{x}_1 + \boldsymbol{x}_2) + \boldsymbol{x}_1^T \Gamma_1^{-1} \Gamma_3 (-\Gamma_1 \boldsymbol{x}_1 + \boldsymbol{x}_2) + \tilde{\boldsymbol{\eta}}^T \Gamma_\eta^{-1} \dot{\tilde{\boldsymbol{\eta}}} \\ & + \left(\int_{t_0}^{t} \boldsymbol{x}_1 \, dt \right)^T \Gamma_1 \Gamma_3 \boldsymbol{x}_1 + \boldsymbol{x}_1^T \Gamma_3 \boldsymbol{x}_1 + \left(\int_{t_0}^{t} \boldsymbol{x}_1 \, dt \right)^T \Gamma_3 (-\Gamma_1 \boldsymbol{x}_1 + \boldsymbol{x}_2) \\ & + \boldsymbol{x}_2^T (-\Gamma_2 \boldsymbol{x}_2 - \Gamma_3 \int_{t_0}^{t} \boldsymbol{x}_1 dt + \boldsymbol{f}(\boldsymbol{x}_1, \boldsymbol{x}_2) + \boldsymbol{h}(\boldsymbol{x}_1, \boldsymbol{x}_2) \tilde{\boldsymbol{\eta}} + \boldsymbol{g}(\boldsymbol{x}_1, \boldsymbol{x}_2) \boldsymbol{u}) \\ = & -\boldsymbol{x}_1^T \Gamma_1 \boldsymbol{x}_1 + \boldsymbol{x}_1^T \boldsymbol{x}_2 + \boldsymbol{x}_1^T \Gamma_1^{-1} \Gamma_3 \boldsymbol{x}_2 - \boldsymbol{x}_2^T \Gamma_2 \boldsymbol{x}_2 \\ & + \boldsymbol{x}_2^T [\boldsymbol{f}(\boldsymbol{x}_1, \boldsymbol{x}_2) + \boldsymbol{g}(\boldsymbol{x}_1, \boldsymbol{x}_2) \boldsymbol{u}] + \tilde{\boldsymbol{\eta}}^T \{ \Gamma_\eta^{-1} \dot{\tilde{\boldsymbol{\eta}}} + [\boldsymbol{h}(\boldsymbol{x}_1, \boldsymbol{x}_2)]^T \boldsymbol{x}_2 \} \\ = & -\boldsymbol{x}_1^T \Gamma_1 \boldsymbol{x}_1 + \boldsymbol{x}_1^T (I + \Gamma_1^{-1} \Gamma_3) \boldsymbol{x}_2 - \boldsymbol{x}_2^T \Gamma_2 \boldsymbol{x}_2 \\ & + \boldsymbol{x}_2^T [\boldsymbol{f}(\boldsymbol{x}_1, \boldsymbol{x}_2) + \boldsymbol{g}(\boldsymbol{x}_1, \boldsymbol{x}_2) \boldsymbol{u}] + \tilde{\boldsymbol{\eta}}^T \{ \Gamma_\eta^{-1} \dot{\tilde{\boldsymbol{\eta}}} + [\boldsymbol{h}(\boldsymbol{x}_1, \boldsymbol{x}_2)]^T \boldsymbol{x}_2 \} \end{aligned} \tag{93}$$

If we choose

$$\Gamma_2 = \frac{1}{4} \Gamma_1^{-1} (I + \Gamma_1^{-1} \Gamma_3)^T (I + \Gamma_1^{-1} \Gamma_3) + \Gamma_4 \tag{94}$$

$$\boldsymbol{u} = -[\boldsymbol{g}(\boldsymbol{x}_1, \boldsymbol{x}_2)]^{+} [\boldsymbol{f}(\boldsymbol{x}_1, \boldsymbol{x}_2) + \boldsymbol{K} \circ \operatorname{sgn}(\boldsymbol{x}_2)] \tag{95}$$

and

$$\dot{\hat{\boldsymbol{\eta}}} = -\Gamma_{\eta}[\boldsymbol{h}(\boldsymbol{x}_1, \boldsymbol{x}_2)]^T \boldsymbol{x}_2 \tag{96}$$

where Γ_4 is an arbitrary positive diagonal matrix. Then,

$$\begin{aligned} \dot{V} &= -\boldsymbol{x}_1^T \Gamma_1 \boldsymbol{x}_1 + \boldsymbol{x}_1^T (\boldsymbol{I} + \Gamma_1^{-1}\Gamma_3)\boldsymbol{x}_2 - \boldsymbol{x}_2^T \Gamma_2 \boldsymbol{x}_2 \\ &\quad + \boldsymbol{x}_2^T [\boldsymbol{f}(\boldsymbol{x}_1, \boldsymbol{x}_2) + \boldsymbol{g}(\boldsymbol{x}_1, \boldsymbol{x}_2)\boldsymbol{u}] + \tilde{\boldsymbol{\eta}}^T \{\Gamma_{\eta}^{-1}\dot{\hat{\boldsymbol{\eta}}} + [\boldsymbol{h}(\boldsymbol{x}_1, \boldsymbol{x}_2)]^T \boldsymbol{x}_2\} \\ &= -(\Gamma_1^{1/2}\boldsymbol{x}_1 - \Gamma_2^{1/2}\boldsymbol{x}_2)^2 - \boldsymbol{x}_2^T \Gamma_4 \boldsymbol{x}_2 \le \boldsymbol{0} \end{aligned} \tag{97}$$

Use the Lyapunov stability theorem [66], we can conclude that the close loop system is asymptotically stable.

Theorem 2: If B is unknown but bonded by Eq. (82), and the following controller and parameter update law are adopted

$$\boldsymbol{u} = -[\hat{\boldsymbol{g}}(\boldsymbol{x}_1, \boldsymbol{x}_2)]^{+}[\boldsymbol{f}(\boldsymbol{x}_1, \boldsymbol{x}_2) + \boldsymbol{K} \circ \mathrm{sgn}(\boldsymbol{x}_2)],\ \boldsymbol{K} \in \mathbb{R}^{3\times 1}, \boldsymbol{K} \ge \boldsymbol{0} \tag{98}$$

$$\dot{\hat{\boldsymbol{\eta}}} = -\Gamma_{\eta}[\boldsymbol{h}(\boldsymbol{x}_1, \boldsymbol{x}_2)]^T \boldsymbol{x}_2 \tag{99}$$

where $\mathrm{sgn}(x) = \begin{cases} 1, & if\ x \ge 0 \\ -1, & if\ x < 0 \end{cases}$, $\hat{\boldsymbol{g}}(\boldsymbol{x}_1, \boldsymbol{x}_2) \triangleq \dfrac{\partial \boldsymbol{f}_1(\boldsymbol{x}_1, \boldsymbol{x}_2)}{\partial \boldsymbol{x}_2} J^{-1}\hat{B}$, and "$\circ$" denotes the element by element multiplication. Then, the closed-loop system in Eq. (80) is globally asymptotically stable.

Proof: Use the same Laypunov function as in Eq. (92) $V \ge \boldsymbol{0}$, and take derivative of the Lyapunov function, we get Eq.(93). Then, submit Eq. (94), (98), (99), and (82) into Eq.(93), we can obtain

$$
\begin{aligned}
\dot{V} &= -\boldsymbol{x}_1^T\Gamma_1\boldsymbol{x}_1 + \boldsymbol{x}_1^T(I+\Gamma_1^{-1}\Gamma_3)\boldsymbol{x}_2 - \boldsymbol{x}_2^T\Gamma_2\boldsymbol{x}_2 \\
&\quad + \boldsymbol{x}_2^T[\boldsymbol{f}(\boldsymbol{x}_1,\boldsymbol{x}_2)+\boldsymbol{g}(\boldsymbol{x}_1,\boldsymbol{x}_2)\boldsymbol{u}] + \tilde{\boldsymbol{\eta}}^T\{\Gamma_\eta^{-1}\dot{\tilde{\boldsymbol{\eta}}} + [\boldsymbol{h}(\boldsymbol{x}_1,\boldsymbol{x}_2)]^T\boldsymbol{x}_2\} \\
&= -\boldsymbol{x}_1^T\Gamma_1\boldsymbol{x}_1 + \boldsymbol{x}_1^T(I+\Gamma_1^{-1}\Gamma_3)\boldsymbol{x}_2 - \boldsymbol{x}_2^T\Gamma_2\boldsymbol{x}_2 + \tilde{\boldsymbol{\eta}}^T\{\Gamma_\eta^{-1}\dot{\tilde{\boldsymbol{\eta}}} + [\boldsymbol{h}(\boldsymbol{x}_1,\boldsymbol{x}_2)]^T\boldsymbol{x}_2\} \\
&\quad + \boldsymbol{x}_2^T\{\boldsymbol{f}(\boldsymbol{x}_1,\boldsymbol{x}_2) - \boldsymbol{g}(\boldsymbol{x}_1,\boldsymbol{x}_2)[\hat{\boldsymbol{g}}(\boldsymbol{x}_1,\boldsymbol{x}_2)]^+[\boldsymbol{f}(\boldsymbol{x}_1,\boldsymbol{x}_2)+\boldsymbol{K}\circ\mathrm{sgn}(\boldsymbol{x}_2)]\} \\
&= -(\Gamma_1^{1/2}\boldsymbol{x}_1 - \Gamma_2^{1/2}\boldsymbol{x}_2)^2 - \boldsymbol{x}_2^T\Gamma_4\boldsymbol{x}_2 \\
&\quad + \boldsymbol{x}_2^T\{\boldsymbol{f}(\boldsymbol{x}_1,\boldsymbol{x}_2) - (I+\Delta)[\boldsymbol{f}(\boldsymbol{x}_1,\boldsymbol{x}_2)+\boldsymbol{K}\circ\mathrm{sgn}(\boldsymbol{x}_2)]\} \\
&= -(\Gamma_1^{1/2}\boldsymbol{x}_1 - \Gamma_2^{1/2}\boldsymbol{x}_2)^2 - \boldsymbol{x}_2^T\Gamma_4\boldsymbol{x}_2 + \boldsymbol{x}_2^T\{\Delta\boldsymbol{f}(\boldsymbol{x}_1,\boldsymbol{x}_2) - (I+\Delta)\boldsymbol{K}\circ\mathrm{sgn}(\boldsymbol{x}_2)\}
\end{aligned}
\tag{100}
$$

Since $\Delta \le G$, we get

$$
\dot{V} \le -(\Gamma_1^{1/2}\boldsymbol{x}_1 - \Gamma_2^{1/2}\boldsymbol{x}_2)^2 - \boldsymbol{x}_2^T\Gamma_4\boldsymbol{x}_2 + |\,\boldsymbol{x}_2^T\,|\{G\boldsymbol{F}(\boldsymbol{x}_1,\boldsymbol{x}_2) - (I-G)\boldsymbol{K}\} \tag{101}
$$

where $\boldsymbol{F}(z_1,z_2)$ is given by

$$
\boldsymbol{F}(\boldsymbol{x}_1,\boldsymbol{x}_2) \triangleq \frac{1}{2}\big[\boldsymbol{f}(\boldsymbol{x}_1,\boldsymbol{x}_2) + |\,\boldsymbol{f}(\boldsymbol{x}_1,\boldsymbol{x}_2)\,|\big] \tag{102}
$$

From Eq. (101), we can see that if we can find a $\boldsymbol{K}$ such that $G\boldsymbol{F}(\boldsymbol{x}_1,\boldsymbol{x}_2) - (I-G)\boldsymbol{K} \le \boldsymbol{0}$, then $\dot{V} \le \boldsymbol{0}$. Luckily the solution of $\boldsymbol{K}$ exists and it is unique for the special case of $G\boldsymbol{F}(\boldsymbol{x}_1,\boldsymbol{x}_2) - (I-G)\boldsymbol{K} = \boldsymbol{0}$, which is guaranteed by the following Lemma.

Lemma 1: Let $G \in \mathbb{R}^{3\times 3}$ be a positive and diagonally dominant with $0 < G_{ii} < 0.5$ and $\boldsymbol{F}(\boldsymbol{x}_1,\boldsymbol{x}_2) \ge 0$ $\boldsymbol{F}(\boldsymbol{x}_1,\boldsymbol{x}_2) \ge 0$. There is always a solution $\boldsymbol{K} \ge 0$ such that $\boldsymbol{F}(\boldsymbol{x}_1,\boldsymbol{x}_2) - \big(I-G\big)\boldsymbol{K} = \boldsymbol{0}$.

Proof: Since $G \in \mathbb{R}^{3\times 3}$ is diagonal and positive, and $0 < G_{ii} < 0.5$, so, the maximum eigenvalue $\lambda_{\max}$ of G is $\lambda_{\max} = \max\{G_{11}, G_{22}, G_{33}\} < 1$. . Using the Frobenius-Perron Theorem [47], we can conclude that there is always a solution of $\boldsymbol{K}$ to the equation $\boldsymbol{F}(\boldsymbol{x}_1,\boldsymbol{x}_2) - \big(I-G\big)\boldsymbol{K} = 0$ and all the components of $\boldsymbol{K}$ are non-negative. Moreover, the solution is given by

$$\boldsymbol{K} = \left(I - G\right)^{-1} \boldsymbol{F}\left(\boldsymbol{x}_1, \boldsymbol{x}_2\right) = \left(I - G\right)^{-1} G\boldsymbol{F}\left(\boldsymbol{x}_1, \boldsymbol{x}_2\right) \tag{103}$$

Simulation Results

The simulation diagram is shown in Figure 65. Compared to the block diagram for reality flight in Figure 62, an additional airflow simulator block is added to the system. Theoretically, to simulate the real-time flight scenarios, a best candidate of the airflow simulators should have fast speed, be easy to embed into the control system, and capable of simulating both pressure and shear stresses. To the best knowledge of the authors, software that could simulate the distributions of pressure and shear stresses simultaneously is not mature yet. Here, consider the flexibility in MAV configuration design, AVL® [54] is adopted for the pressure distribution calculation, while the shear stress is simulated as $\tau = \frac{1}{2}\rho_\infty V_\infty^2 c_f$ and for laminar flows $c_f = \frac{0.664}{\sqrt{\mathrm{Re}_x}}$, for turbulent flows $c_f = \frac{0.0592}{\sqrt{\mathrm{Re}_x}}$, $\mathrm{Re}_x = \frac{V_\infty \rho_\infty x}{\mu_\infty}$, where V_∞ is the free stream wind speed, ρ_∞ is the air density, μ_∞ is the absolute viscosity coefficient, x is the distance to the leading edge.

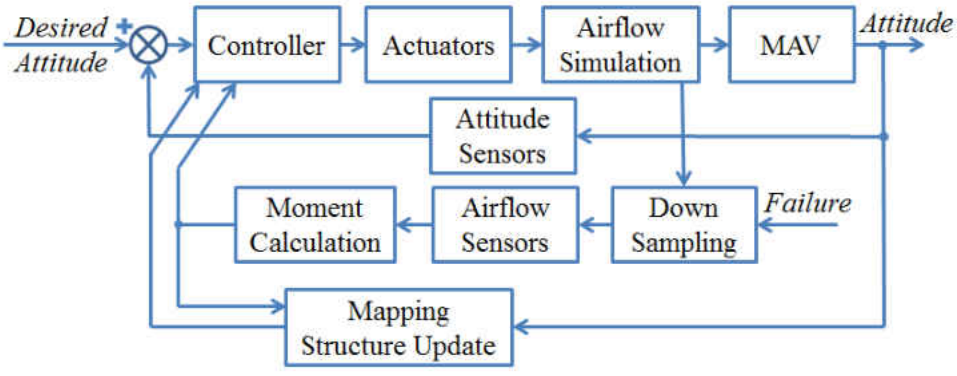

Figure 65 Simulation diagram of attitude control

The configuration of the MAV used in this paper is the same as that in [61], which is duplicated as Figure 45. The geometrical sizes are given as follows, c_r = 10 cm, c_t = 5 cm, b = 15 cm, c_e = 2 cm, b_e = 7.5 cm, d = 1 cm, h = 3 cm, w = 3 cm, and the moment of inertia is J = [0.0526, 0, 0.0049; 0, 0.0804, 0; 0.0049, 0, 0.0405] $\mathrm{kg}\cdot\mathrm{m}^2$. Forty sensor couples are placed on the mean aerodynamic chords on the wing, while five sensor couples are placed on the middle horizontal section of the rudder. Considering the fact that AVL can only simulate the flow over the mean chord surface of a MAV, the sensors are placed in couples, where a sensor couple is composed of two sensors that share the same X^B and Y^B (Z^B) components but on both sides of the wing (rudder) surface. Moreover, to make full use of these sensor couples and reduce the number of sensors needed for airflow sensing purpose, the sensor couples on the wing and elevon surfaces are placed on the mean aerodynamic chord section; while on the rudder surface, five sensor couples are placed vertically along the middle line of the surface. Considering the symmetry of the wing, chordwise location of the half number the sensors on the wing and all sensors on the rudder are given in Table 15. Here, sensor couples $S_1,\cdots,S_{20}$ are on the left wing, sensor couples $S_{21},\cdots,S_{40}$ are on the right wing, and sensor couples $S_{41},\cdots,S_{45}$. The values are given in percentage of the length of mean aerodynamic chord, measured from the leading edge of the mean aerodynamic chord and rudder respectively.

Table 15 Chordwise locations of the sensor couples

S_1	1%	S_2	2%	S_3	4%	S_4	6%	S_5	9%
S_6	13%	S_7	17%	S_8	22%	S_9	38%	S_{10}	45%
S_{11}	53%	S_{12}	60%	S_{13}	65%	S_{14}	70%	S_{15}	74%
S_{16}	76%	S_{17}	80%	S_{18}	85%	S_{19}	96%	S_{20}	98%
S_{41}	10%	S_{42}	30%	S_{43}	50%	S_{44}	70%	S_{45}	90%

Before we show the experiment of the attitude control performance, the comparison of the "actual" moment on the MAV and that calculated from the sensor measurement. Here, the "actual" moment on the MAV is calculated from using 685 nodes on surface of the MAV, while a down-sampled 45 nodes (sensors) are used as nominal sensor measurements. Here, The free stream wind speed V_∞ is randomly chosen within a range of [5, 25] m/s, and the angle of the attitude angles are randomly selected from $\boldsymbol{\theta} \sim U[\boldsymbol{\theta}_{\min}, \boldsymbol{\theta}_{\max}]$, where $\boldsymbol{\theta}_{\min} = [-10, -5, -20]^T$ degs, and $\boldsymbol{\theta}_{\max} = [10, 20, 20]^T$; the angular rates are randomly selected from $\boldsymbol{\omega} \sim U[\boldsymbol{\omega}_{\min}, \boldsymbol{\omega}_{\max}]$, where $\boldsymbol{\omega}_{\min} = [-10, -10, -10]^T$ degs, and $\boldsymbol{\omega}_{\max} = [10, 10, 10]^T$. It can be seen that the overall calculated results from Figure 66, the mismatch in the moments fall into ranges of [-1,1]×10-3 N·min roll, [-5,5]×10-3 N·m in pitch, and [-2,2]×10-3 N·m in yaw, respectively.

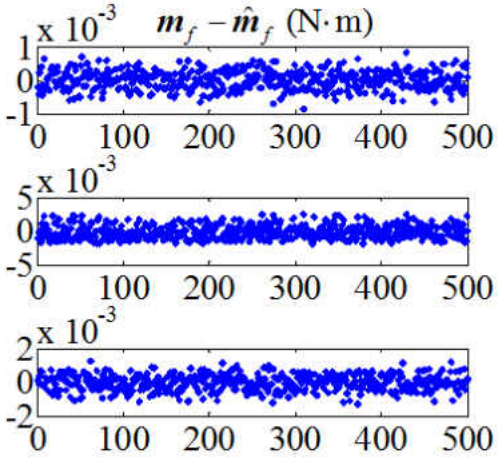

Figure 66 Difference between the "actual" and calculated moments

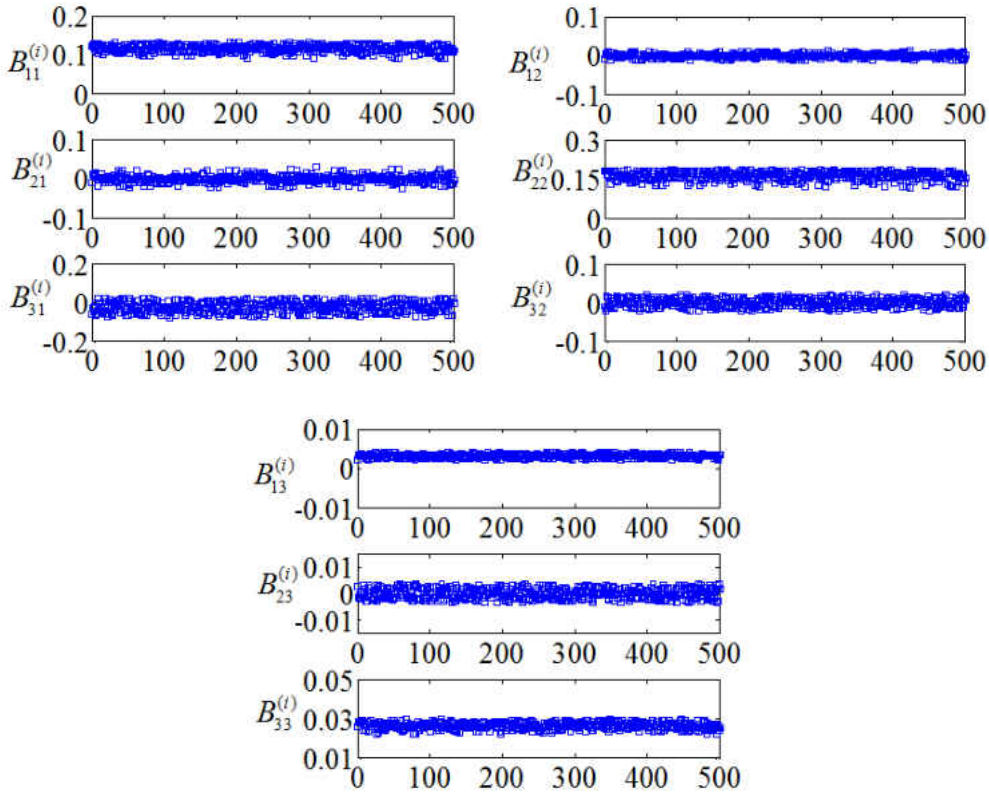

Figure 67 Control input matrix and its bound

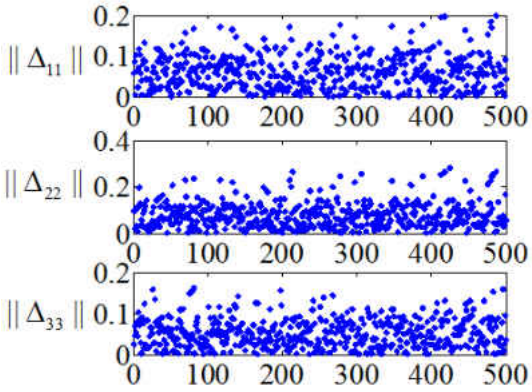

Figure 68 Mismatch bound between matrix B and $\hat{B}$

The uncertainty between the nominal and actual input matrix in Eq. (82) is characterized using the Monte Carlo simulation, where the attitude angles and angular rates are selected the

same ways as mentioned above. The results are shown in Figure 67, where we found that $B^0 = \begin{bmatrix} 0.116 & -0.000 & 0.003 \\ -0.000 & 0.163 & 0.000 \\ -0.017 & 0.001 & 0.027 \end{bmatrix}$ and $B = \begin{bmatrix} 0.116 & 0 & 0 \\ 0 & 0.163 & 0 \\ 0 & 0 & 0.027 \end{bmatrix}$. From Figure 68, we let $G = diag([0.2, 0.3, 0.2])$. Note that the uncertainty matrix G is very conservative, and it can be loosen to $G = diag([0.1, 0.1, 0.1])$ to achieve a better performance. Other parameters in the controller Eq. are set as $\Gamma_1 = 4 \cdot \text{diag}([1,1,1])$, $\Gamma_2 = 2.65 \times \text{diag}([1,1,1])$, $\Gamma_3 = 0.3 \cdot \text{diag}([1,1,1])$, and $\Gamma_\eta = \text{diag}([1,2,1])$. Based on [26], the Euler angle measurement noise is a Gaussian with a zero mean and a standard deviation of 0.2 degrees, and is assumed to be bounded in [-0.6, 0.6] degrees. Similarly, the measurement noise on the angular rate is a Gaussian with a zero mean and a standard deviation of 0.01 deg/s, but assumed to be bounded in [-0.03, 0.03] deg/s. The noise on the pressure sensor is modeled be a zero mean Gaussian noise with a standard deviation of 1.5 Pa, and the noise is bounded in [-4.5, 4.5] Pa. The sensors might have different types of failures, and the most common seen failures are big noise failure, zero output failure, and maximum output failure. All of the three types of failures are tested; it is found that the big noise failure is easiest case to deal with. The zero output failure and the maximum output failure has similar influence on the system performance. Hence, in this paper, the sensor failure is modeled as zero output failure.

The performances of the proposed robust adaptive controller are demonstrated in the following four scenarios. Case I: no airflow sensor fails; Case II: 50% of the airflow sensors $\{S_i \mid i = 1,3,\cdots,45\}$ on the wing surface fail; Case III: all the airflow sensors on the left wing fail; and Case IV: all the air flow sensors fail, but the adaptive compensation is still valid. To

compare the performance as the sensors fail, the same initial and final desired states are used to in these four cases, where the MAV attitude is controlled from $\boldsymbol{\theta}_0 = [0,0,0]^T$ degrees to $\boldsymbol{\theta}_d = [0,5,5]^T$ degrees.

The result of testing Case I is shown in Figure 69. It can be seen that the system can reach desired states within settling time is less than 2 seconds with a less than 10% overshoot. The three control surfaces change within ranges of [8, 14] degrees, [5, 18] degrees, [-18, 30] degrees, respectively. The uncertain parameters in the mapping function settle down in about 3 seconds. This result will be used as a reference for other cases to compare with.

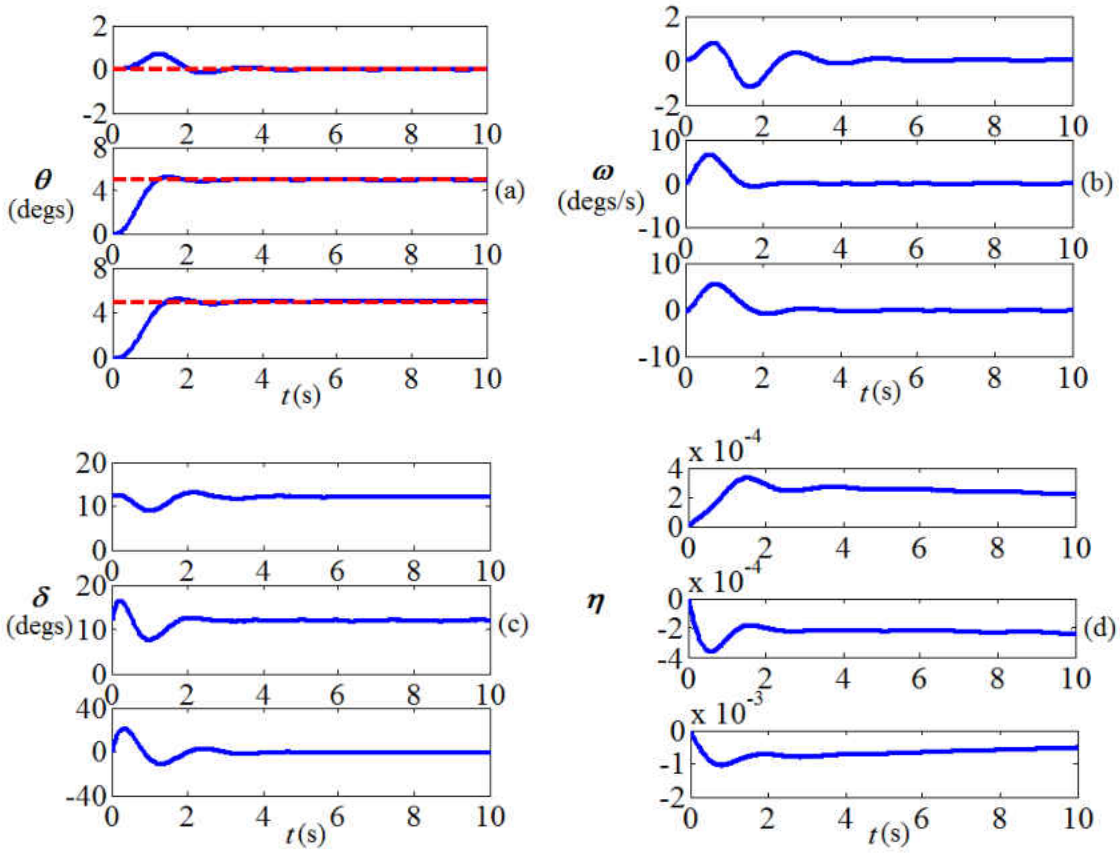

Figure 69 Case I, attitude control performance when there is no sensor failure (a) attitude angles, (b) angular rates, (c) control angles, and (d) structure update parameters

The result of Case II is illustrated in Figure 70, where the sensors with odd numbers $\{S_i \mid i = 1,3,\cdots,45\}$ are failed. As compared to the results of Case I, the settling time of the closed-loop system is approximately 4 seconds. The deflection of control surfaces is larger than that of Case I. As shown in Fig. 10(d), the moment compensation terms have larger oscillations.

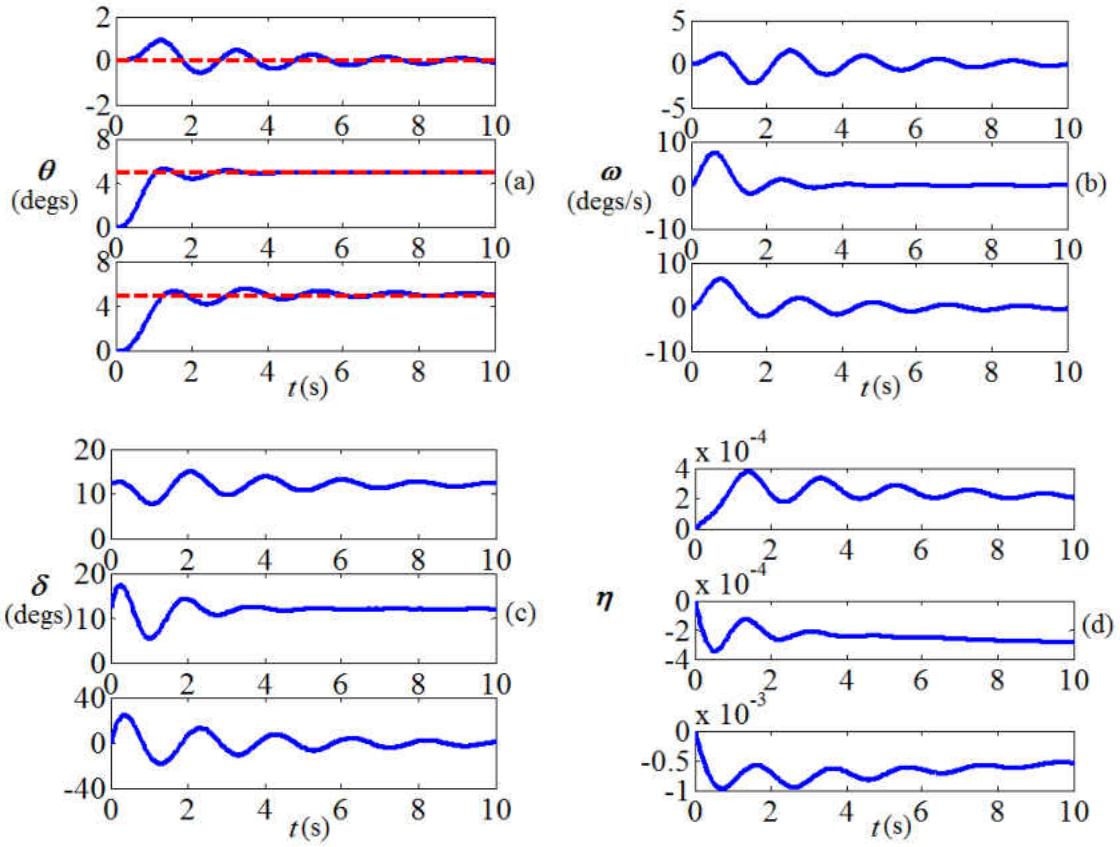

Figure 70 Case II, attitude control performance when 50% sensors on the wing fail (a) attitude angles, (b) angular rates, (c) control angles, and (d) structure update parameters

In Case II, the failure sensors are distributed symmetrically, while in Case III all sensors on the left wing are assumed failed. By comparing Figure 71 to Figure 70, we can see that, the closed loop system is still stable; however, the settling time is much longer (approximately 6 seconds) and the amplitude of oscillation in roll increases up to 1.7 degrees.

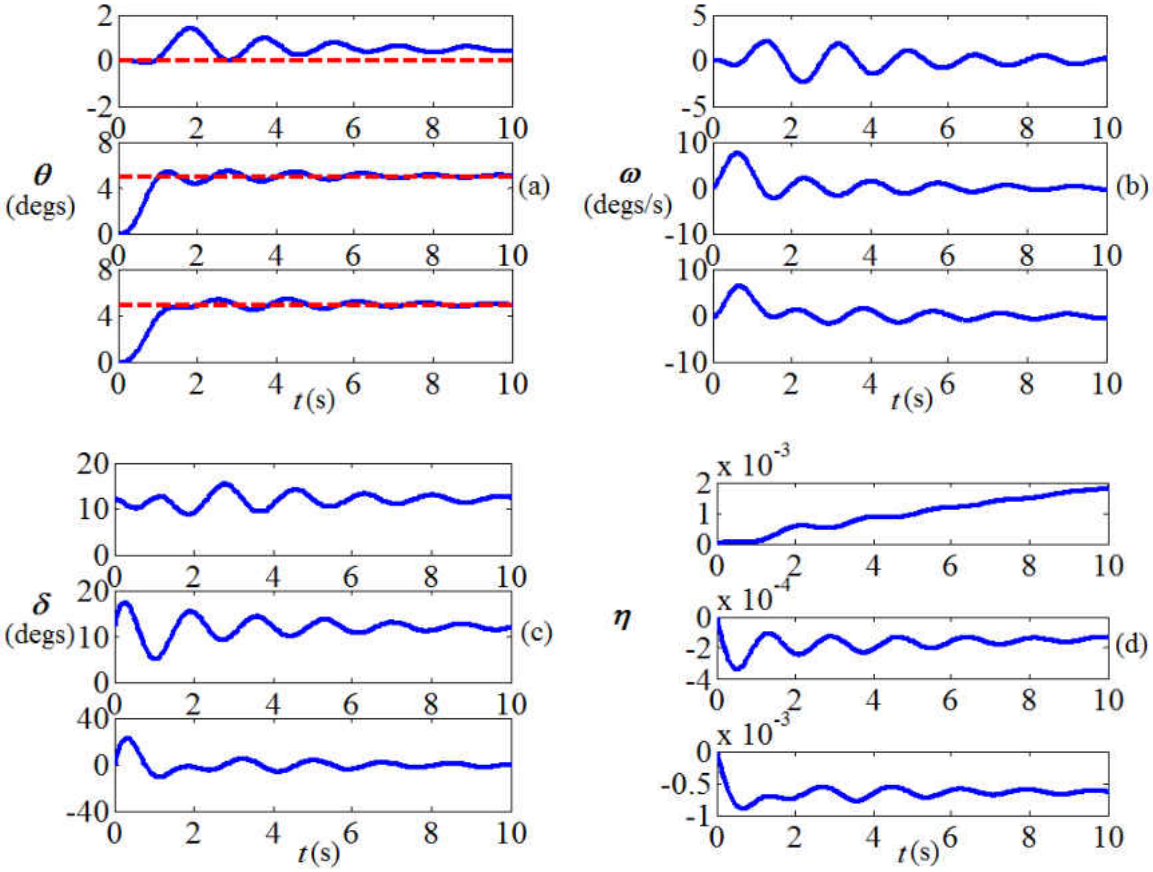

Figure 71 Case III, attitude control performance when all the sensor on the left wing are failed (a) attitude angles, (b) angular rates, (c) control angles, and (d) structure update parameters

In test IV, all the sensors are assumed to be failed, which means that there would be the moment calculated from the airflow measurements are zeros, which will result in a zeros calculated moment. It can be seen from the results in Figure 72 that the system is no longer stable. It also verified that the feedback of airflow information helps the micro air vehicle achieving better flight performance.

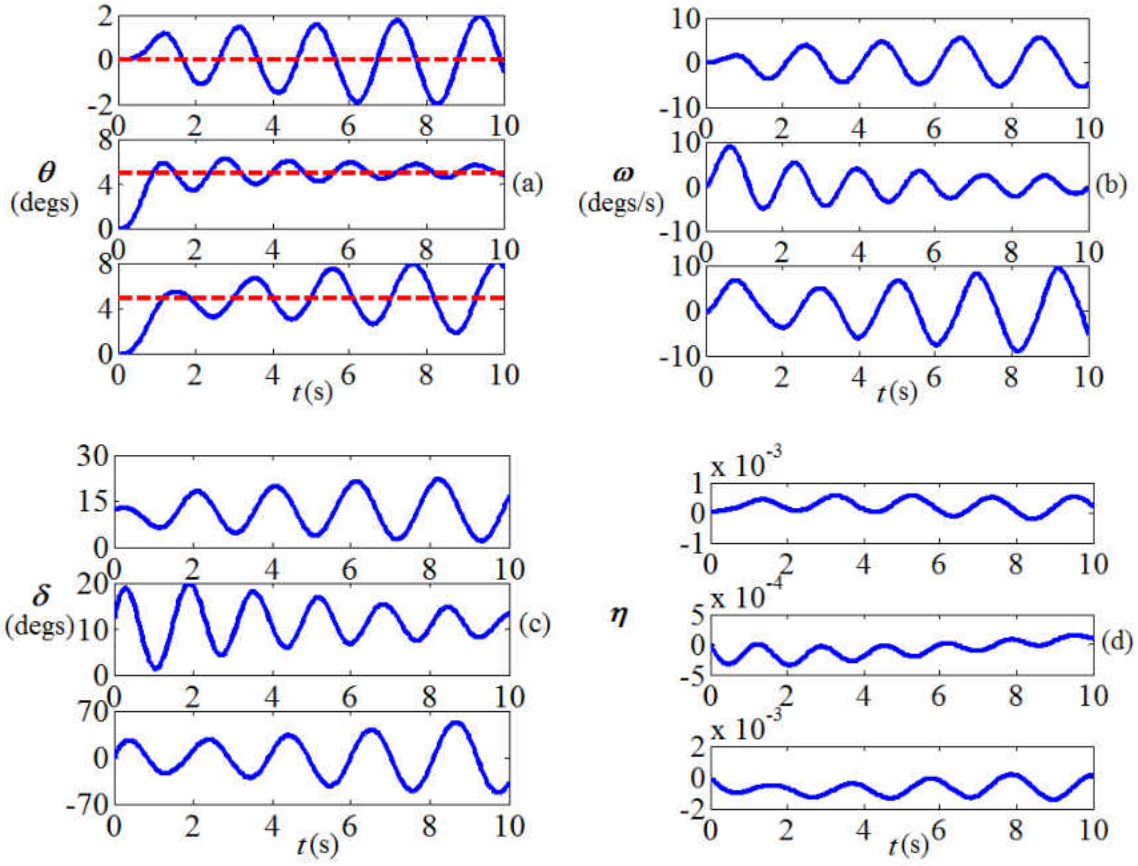

Figure 72 Case IV, attitude control performance when there is no sensor failure (a) attitude angles, (b) angular rates, (c) control angles, and (d) structure update parameters

Appendix A

Through changes of state variables $\begin{cases} \boldsymbol{x}_1 = \boldsymbol{e}_1 \\ \boldsymbol{x}_2 = \Gamma_1 \boldsymbol{e}_1 + \boldsymbol{f}_1(\boldsymbol{e}_1, \boldsymbol{e}_2) \end{cases}$, system in Eq. (86) $\begin{cases} \dot{\boldsymbol{e}}_1 = \boldsymbol{f}_1(\boldsymbol{e}_1, \boldsymbol{e}_2) \\ \dot{\boldsymbol{e}}_2 = \boldsymbol{f}_2(\boldsymbol{e}_1, \boldsymbol{e}_2) - J^{-1}\tilde{\boldsymbol{\eta}} + J^{-1}B\boldsymbol{u} \end{cases}$ can be written in the form in Eq. (88) as

$$\begin{cases} \dot{\boldsymbol{x}}_1 = -\Gamma_1 \boldsymbol{x}_1 + \boldsymbol{x}_2 \\ \dot{\boldsymbol{x}}_2 = -\Gamma_2 \boldsymbol{x}_2 - \Gamma_3 \int_{t_0}^{t} \boldsymbol{x}_1 dt + \boldsymbol{f}(\boldsymbol{x}_1, \boldsymbol{x}_2) + \boldsymbol{h}(\boldsymbol{x}_1, \boldsymbol{x}_2)\tilde{\boldsymbol{\eta}} + \boldsymbol{g}(\boldsymbol{x}_1, \boldsymbol{x}_2)\boldsymbol{u} \end{cases}.$$

Proof: (1) take derivative of the first equation $\boldsymbol{x}_1 = \boldsymbol{e}_1$, we have

$$\begin{aligned}\dot{\boldsymbol{x}}_1 = \dot{\boldsymbol{e}}_1 = \boldsymbol{f}_1(\boldsymbol{e}_1, \boldsymbol{e}_2) &= -\Gamma_1 \boldsymbol{x}_1 + \underbrace{\Gamma_1 \boldsymbol{x}_1 + \boldsymbol{f}_1(\boldsymbol{e}_1, \boldsymbol{e}_2)}_{\boldsymbol{x}_2} \\ &= -\Gamma_1 \boldsymbol{x}_1 + \boldsymbol{x}_2\end{aligned} \tag{104}$$

(2) take derivative of the second equation $\boldsymbol{x}_2 = \Gamma_1 \boldsymbol{e}_1 + \boldsymbol{f}_1(\boldsymbol{e}_1, \boldsymbol{e}_2)$

$$\begin{aligned}\dot{\boldsymbol{x}}_2 &= \Gamma_1 \dot{\boldsymbol{x}}_1 + \dot{\boldsymbol{f}}_1(\boldsymbol{e}_1, \boldsymbol{e}_2) = \Gamma_1 \dot{\boldsymbol{e}}_1 + \frac{\partial \boldsymbol{f}_1}{\partial \boldsymbol{e}_1}\dot{\boldsymbol{e}}_1 + \frac{\partial \boldsymbol{f}_1}{\partial \boldsymbol{e}_2}\dot{\boldsymbol{e}}_2 \\ &= \Gamma_1 \boldsymbol{f}_1 + \frac{\partial \boldsymbol{f}_1}{\partial \boldsymbol{e}_1}\boldsymbol{f}_1 + \frac{\partial \boldsymbol{f}_1}{\partial \boldsymbol{e}_2}\left(\boldsymbol{f}_2 - J^{-1}\tilde{\boldsymbol{\eta}} + J^{-1}B\boldsymbol{u}\right) \\ &= (-\Gamma_2 \boldsymbol{x}_2 - \Gamma_3 \int_{t_0}^{t} \boldsymbol{x}_1 dt) + (\Gamma_2 \boldsymbol{x}_2 + \Gamma_3 \int_{t_0}^{t} \boldsymbol{x}_1 dt) \\ &\quad + \Gamma_1 \boldsymbol{f}_1 + \frac{\partial \boldsymbol{f}_1}{\partial \boldsymbol{e}_1}\boldsymbol{f}_1 + \frac{\partial \boldsymbol{f}_1}{\partial \boldsymbol{e}_2}\left(\boldsymbol{f}_2 - J^{-1}\tilde{\boldsymbol{\eta}} + J^{-1}B\boldsymbol{u}\right) \\ &= -\Gamma_2 \boldsymbol{x}_2 - \Gamma_3 \int_{t_0}^{t} \boldsymbol{x}_1 dt + \underbrace{(\Gamma_2 \boldsymbol{x}_2 + \Gamma_3 \int_{t_0}^{t} \boldsymbol{x}_1 dt + \Gamma_1 \boldsymbol{f}_1 + \frac{\partial \boldsymbol{f}_1}{\partial \boldsymbol{e}_1}\boldsymbol{f}_1 + \frac{\partial \boldsymbol{f}_1}{\partial \boldsymbol{e}_2}\boldsymbol{f}_2)}_{\boldsymbol{f}(\boldsymbol{x}_1, \boldsymbol{x}_2)} \\ &\quad + \underbrace{(-\frac{\partial \boldsymbol{f}_1}{\partial \boldsymbol{e}_2}J^{-1})}_{\boldsymbol{h}(\boldsymbol{x}_1, \boldsymbol{x}_2)}\tilde{\boldsymbol{\eta}} + \underbrace{(\frac{\partial \boldsymbol{f}_1}{\partial \boldsymbol{e}_2}J^{-1}B)}_{\boldsymbol{g}(\boldsymbol{x}_1, \boldsymbol{x}_2)}\boldsymbol{u} \\ &= -\Gamma_2 \boldsymbol{x}_2 - \Gamma_3 \int_{t_0}^{t} \boldsymbol{x}_1 dt + \boldsymbol{f}(\boldsymbol{x}_1, \boldsymbol{x}_2) + \boldsymbol{h}(\boldsymbol{x}_1, \boldsymbol{x}_2)\tilde{\boldsymbol{\eta}} + \boldsymbol{g}(\boldsymbol{x}_1, \boldsymbol{x}_2)\boldsymbol{u}\end{aligned} \tag{105}$$

Combine (1) and (2), the equivalent system is proved.

CHAPTER SIX: CONCLUSIONS AND FUTURE WORK

Conclusions

Birds and bats utilize airflow information sensed by mechanoreceptors to achieve high performance flight. Inspired by this phenomenon, in my dissertation work, a new flight control system for micro aerial vehicles, using real-time airflow information measured from an array of airflow sensors, is studied. The answers to the following key questions have been investigated: (1) how to get accurate airflow information; (2) how to incorporate the airflow information into attitude motion modeling; and (3) how to design a fault tolerant control system to handle the scenarios with sensor failures.

To study the capability of the current sensing technology in airflow perception, a 28.25 cm straight wing with 9 sensors (6 on the upper surface and 3 on the lower surface) was designed and tested in the UCF low speed wind tunnel. The results show that the 9-sensors configuration can provide very good pressure distribution approximation on a straight wing with no control surfaces and the error in the lift calculation is about 10%. After that, pitching control using real-time measured pressure information is validated in the wind tunnel tests using a 22 cm straight wing (with an elveon) with 12 sensors (6 on the upper surface and 6 on the lower surface). Although the system operates at a low frequency of 2 Hz, this platform was able to achieve the desired commands with a rising time, settling time, and overshoot of about 2 seconds, 5 seconds and 10% respectively.

Since the sensor suite that can simultaneously measure pressure and shear stress with a suitable range, satisfactory size, weight, accuracy, and updating frequency is still under development, more advanced designs are carried out in simulation. The simulated environment is

programed in MATLAB, and both steady and turbulent flow conditions can be mimicked. A nonlinear robust control, considering parametric and functional uncertainties, is designed to test the pitching control of a straight wing with 20 pressure sensors and an elevon. It is shown that the closed loop system can achieve a stable performance with a rising time of, settling time, and overshoot of about 1 second, 1.5 seconds, and 6% respectively. Then, the research is extended to three-axes attitudes control problems. A delta-wing MAV with two elevons and a rudder is designed using AVL for the testing. With the robust controller, the close loop system can achieve stable results under various airflow conditions. With the system operates at 20 Hz, the rising time, settling time, overshoot can be of the closed-loop system performances are 2 seconds, 3 seconds, and 10%, respectively. The control performance is much better than that of the traditional attitude control system, which only uses rigid body information, especially under several wind turbulence.

Aside from the control of normal operated MAVs, the problem of how to control the system in case of some of the sensors fail during flight was also studied. Taking into consideration of the parametric uncertainties in the control input matrix and sensor failure induced error in moment calculation, a fault tolerant controller was designed. The controller is capable of achieving asymptotically stable results while adaptively compensating errors in moment calculations. The results show that, even if 50% (all the odd numbered sensors) of sensors fail, the system can still achieve a satisfying result with a rising time within 1.5 seconds, settling time of within 4 seconds, and overshoot of 10%.

Future Work

Much progress has been made in my study on designing an airflow sensor array empowered MAV flight control systems; however there are still many challenging problems need to be addressed to implement the system on the existing MAVs. Some of the emerging tasks are:

MAV Structural Design: Due to the volume, weight, and power constraints, the design of the sensor-rich control based MAV is quite different from traditional MAV designs. Configurations that are convenient to incorporate airflow sensing are preferred. Moreover, the arrangement of the sensors and supporting devices add more challenges to the design.

Sensor Technology: Up to now, there is not a sensor suite that can simultaneously measure pressure and shear stresses with a suitable range, satisfactory size, weight, accuracy, and updating frequency. We are collaborating with other sensor experts to investigate new sensors.

Sensing System Design: Since the sensor array is designed to read the data in serial, the system is constrained to operate at a low frequency of about 2 Hz, which is too low for advanced controller design. Parallel communication will be designed to increase the data reading frequency of the system, so that more advanced controllers can be applied.

LIST OF REFERENCES

[1] Petricca, L., Ohlckers, P., and Grinde, C., "Micro- and Nano-Air Vehicles: State of the Art," *International Journal of Aerospace Engineering*, Vol. 2011, 2011, Article 214549.

[2] Pines, D. J., and Bohorquez, F., "Challenges Facing Future Micro Air Vehicle Development," *Journal of Aircraft*, Vol. 43, No. 2, 2006, pp. 290-305.

[3] Davis, W. R., Kosicki, B. B., Boroson, D. M., and Kostishack, D. F., "Micro Air Vehicles for Optical Surveillance," *The Lincoln Laboratory Journal*, Vol. 9, No. 2, 1996, pp. 197-214.

[4] Golightly, I., and Jones, D., "Visual Control of an Unmanned Aerial Vehicle for Power Line Inspection," *12th International Conference on Advanced Robotics*, Seattle, WA, July 18-20, 2005.

[5] Hept, G. B., *Infrared Systems for Tactical Aviation: An Evolution in Military Affairs?*, Technical Report, Air University, Maxwell Air Force Base, Alabama, 2002.

[6] Huber, A. F. I., *Death by a Thousand Cuts: Micro-Air Vehicles in the Service of Air Force Missions*, Technical Report, Air University, Maxwell Air Force Base, Alabama, 2001.

[7] Grzywna, J. W., Plew, J., Nechyba, M. C., and Ifju, P. G., "Enabling autonomous MAV flight," *Procedings of 16th Florida Conference on Recent Advances in Robotics*, 2003.

[8] Torres, G., and Mueller, T. J., "Micro Aerial Vehicle Development: Design, Components, Fabrication, and Flight Testing," *the AUVSI Unmanned Systems Symposium and Exhibition*, Orlando, FL, July 11-13, 2000.

[9] Ifju, P. G., Jenkins, D. Ettinger, A., Lian, Y., Shyy, W., and Waszak, M. R., "Flexible-wing-based micro air vehicles," *Procedings of AIAA,* Paper No. 2002-0705, 2002.

[10] Mueller, T., Kellogg, J., Ifju, P., and Shkarayev, S., *Introduction to the Design of Fixed-Wing Micro Air Vehicles: Including Three Case Studies*, AIAA Education Series, 2007.

[11] Shyy, W., Lian, Y., Teng, J., Viieru, D., and Liu, H., *Aerodynamics of Low Reynolds Number Flyers*, Cambridge University Press, Cambridge, United Kingdom, 2008.

[12] Tian, X., Iriarte, J., Middleton, K., Galvao, R., Israeli, E., and Roemer, A., "Direct Measurements of the Kinematics and Dynamics of Bat Flight," *Bioinspiration & Bioinformatics*, Vol. 1, No. 4, 2006, pp. 10-18.

[13] Richardson, P. L., "How Do Albatrosses Fly around the World without Flapping Their Wings?" *Progress in Oceanography*, Vol. 88, No. 1-4, 2011, pp. 46-58.

[14] Brown, R. E., and Fedde, M. R., "Airflow Sensors in the Avian Wing," *Journal of Experimental Biology*, Vol. 179, No. 1, 1993, pp. 13 -30.

[15] Dickinson, B. T., Singler, J. R., and Batten, B. A., "Mathematical Modeling and Simulation of Biologically Inspired Hair Receptor Arrays in Laminar Unsteady Flow Separation," *Journal of Fluids and Structures*, Vol. 29, 2012, pp. 1-17.

[16] http://www.learner.org/jnorth/tm/eagle/WeatherBarometer.html, last access on Dec. 18, 2011.

[17] Grasmeyer, J. M. and Keennon, M. T., "Development of the black widow micro air vehicle," *Proceedings of the 39th AIAA Aerospace Sciences Meeting and Exhibit*, Paper No. 2001-0127, 2001.

[18] Gad-el-Hak, M., "Micro-air-vehicles: can they be controlled better?," *Journal of Aircraft,* Vol. 38, No. 3, 2001, pp. 419-429.

[19] Morris, S. J. and Holden, M., "Design of micro air vehicles and flight test validation," *Proceedings of Fixed, Flapping and Rotary Wing Vehicles at Very Low Reynolds Numbers*, 2000, pp. 153-176.

[20] Kellogg, J., Bovais, C., Dahlburg, J., Foch, R., Gardner, J., Gordon, D., Hartley, R.; Kamgar-Parsi, B., McFarlane, H., Pipitone, F., Ramamurti, R., Sciambi, A., Spears, W., Srull, D., and Sullivan, C., "The NRL MITE air vehicle," *Procedings of the 16th International Conference of Unmanned Air Vehicle Systems*, Bristol, UK, 2002, pp. 25.1-14.

[21] Salehipour, H., and Amiri, N., "Design of HOMA micro air vehicle at IUT," *Proceddings of the 3rd US-European Competition and Workshop on Micro Air Vehicle System (MAV07) & European Micro Air Vehicle Conference and Flight Competition (EMAV2007)*, Toulouse, France, 2007.

[22] Kanade, T., Amidi, O., and Ke, Q., "Real-time and 3D Vision for Autonomous Small and Micro Air Vehicles," *Processing of 43rd IEEE Conference on Decision and Control*, Atlantis, Paradise Island, Bahamas, December 14-17, 2004, pp. 1655-2216.

[23] Webb, T. P., Prazenica, R. J., Kurdila, A. J., and Lind, R., "Vision-based State Estimation for Autonomous Micro Air Vehicles," *Journal of Guidance, Control and Dynamics*, Vol. 30, No. 3, 2007, pp. 816-826.

[24] Gans, N. R., Dixon, W. E., Lind, R., and Kurdila, A., "A Hardware in the Loop Simulation Platform for Vision-based Control of Unmanned Air Vehicles," *Mechatronics*, Vol. 19, Issue 7, 2009, pp. 1043-1056.

[25] Ettinger, S. M., Nechyba, M. C., Ifju, P. G., and Waszak, M., "Vision-Guided Flight Stability and Control for Micro Air Vehicles," *IEEE/RSJ International Conference on*

Intelligent Robots and Systems, EPFL, Switzerland, September 30-October 4, 2002, pp. 2134-2140.

[26] Winkler, S., Buschmann, M., Kordes, T., Schulz, H. W., and Vörsmann, P., "MEMS-based IMU Development, Calibration and Testing for Autonomous MAV Navigation," *Proceedings of the 59th Annual Meeting of The Institute of Navigation and CIGTF 22nd Guidance Test Symposium*, Albuquerque, NM, 2003, pp. 128-134.

[27] Achtelik, M., Achtelik, M., Weiss, S., and Siegwart, R., "Onboard IMU and Monocular Vision based Control for MAVs in Unknown In and Outdoor Environment," *2011 IEEE International Conference on Robotics and Automation*, Shanghai, China, May 9-13, 2011,pp. 3056-3063.

[28] Davis, W. R., Kosicki, B. B., Boroson, D. M., and Kostishack, D. F., "Micro air vehicles for optical surveillance," *Lincoln Laboratory Journal,* Vol. 9, No. 2, 1996, pp. 197-214.

[29] Kanowitz, S. M., *Design and Implementation of a GPS Based Navigation System for Micro Air Vehicles*, M.S. Thesis, University of Florida, 2002.

[30] Taylor, B., Bil, C., Watkins, S., and Egan, G., "Horizon Sensing Attitude Stabilization: A VMC Autopilot," *the 18th International UAV systems Conference*, Bristol, UK, March 2003.

[31] Xu, Y., Jiang, F., Newbern, S., Huang, A., Ho, C. and Tai, Y., "Flexible Shear-stress Sensor Skin and Its Application to Unmanned Aerial Vehicles," *Sensors and Actuators A: Physical*, Vol. 105, 2003, pp. 321-329.

[32] Callegari, S., Zagnoni, M., Golfarelli, A., Tartagni, M., Talamelli, A., Proli, P., and Rossetti, A., "Experiments on Aircraft Flight Parameter Detection by On-skin Sensors," *Sensors and Actuators A: Physical*, Vol. 130–131, Aug. 2006, pp. 155–165.

[33] Fei, H., Zhu, R., Zhou, Z., and Wang, J., "Aircraft Flight Parameter Detection Based on a Neural Network Using Multiple Hot-film Flow Speed Sensors," *Smart Materials and Structures*, Vol. 16, No. 4, 2007, pp. 1239-1245.

[34] Vogel, J. M., and Kelkar, A. G., "Aircraft Control Augmentation and Health Monitoring Using Flush Air Data System Feedback," *26th AIAA Applied Aerodynamics Conference*, Aug. 2008, AIAA Paper 2008-7505.

[35] Guerreiro, N. M. and Hubbard, J. E., "Pressure Port Placement for Lift Distribution Measurement on a Model Aircraft with Optimized Trailing-Edge Flaps," *26th AIAA Applied Aerodynamics Conference*, Honolulu, Hawaii, August 18-20, 2008, AIAA-2008-7518.

[36] Keshavan, J., and Humbert, J. S., "MAV Stability Augmentation using Weighted Outputs from Distributed Hair Sensor Arrays," *2010 American Control Conference*, Baltimore, MD, June 30-July 02, 2010, pp. 4445-4450.

[37] Vyalkov, A. V., Zimenkov, E. V., Abashkin, A. M., and Pazhitnov, E. V., "Measurement of pressure distribution in a wind-tunnel experiment using electronic pressure commutators," *Measurement Techniques*, Vol. 37, No. 8, 1995, pp. 45-49.

[38] Fritsch, F. N., and Carlson, R. E., "Monotone Piecewise Cubic Interpolation," *SIAM Journal on Numerical Analysis*, Vol. 17, Issue 2, 1980, pp. 238-246.

[39] http://web.mit.edu/16.unified/www/FALL/fluids/Lectures/f03.pdf, last accessed on March 12, 2012.

[40] http://www.av8n.com/how/htm/4forces.html, last accessed on March 12, 2012.

[41] Cook, M. V., *Flight Dynamics Principles*, 2nd Edition, Elsevier Ltd., Burlington, MA, 2007.

[42] Xu, Y., "Chattering Free Robust Control for Nonlinear Systems," *IEEE Transaction on Control Systems Technology*, Vol. 16, No.6, 2008, pp.1352-1359.

[43] Bartolini, G., Ferrara, A., and Usai E., "Chattering Avoidance by Second-order Sliding Mode Control," *IEEE Transaction on Automatic Control*, Vol. 43, No. 2, 1998, pp. 241-246.

[44] Gessing, R., "Sliding Mode Control with Decreased Chattering-model and Simulations," *IEEE International Symposium on Computer-Aided Control System Design*, Anchorage, AK, September 25-27, 2000, pp. 273-278.

[45] Tseng, M., and Chen, M., "Chattering Reduction of Sliding Mode Control by Low-Pass Filtering the Control Signal," *Asian Journal of Control*, Vol. 12, Issue 3, 2010, pp. 392-398.

[46] Rafimanzelat, M. R., and Yazdanpanah, M. J., "A Novel Low Chattering Sliding Mode Controller," *5th Asian Control Conference*, Vol. 3, July 20-23, 2004, pp. 1958-1963.

[47] Slotine, J. J., and Li, W., *Applied Nonlinear Control*, Prentice Hall, 1991.

[48] Drela, M. and Youngren, H., *XFOIL: Subsonic Airfoil Development System*, http://raphael.mit.edu/xfoil/, 2000, last accessed on March 12, 2012.

[49] Bosch Sensortec, *BMP085 Digital Pressure Sensor Data Sheet*, Reutlingen, Germany, 2008.

[50] Shen, H., Xu, Y. and Remeikas, C., "Pitch Control of a Micro Aerial Vehicle with an Array of Micro Pressure Sensors," *Journal of Aircraft*, Vol. 50, No. 1, 2013, pp. 239-248.

[51] H. W, D. Sun, and Z. Zhou, "Micro Air Vehicle: Configuration, Analysis, Fabrication, and Test," *IEEE/ASME Transactions on Mechatronics*, Vol. 9, No. 1, 2004, pp. 108-117.

[52] Thipyopas, C.and Moschetta, J., "Micro Air Vehicle's drag reduction by biplane," *Span,* Vol. 44, 2007, pp. 1-12.

[53] Web: http://theknowledgeworld.com/world-of-aerospace/Aerodynamics-Softwares.htm, last accessed on December 20th, 2012.

[54] Drela, M. and Youngren, H., web: http://web.mit.edu/drela/Public/web/avl/, last accessed on January 20th, 2013.

[55] Ljung, L., "Linear System Identification as Curve Fitting," *Springer lecture notes on control and identification*, Vol. 286, 2003, pp. 203-215.

[56] Kohavi, R., "A study of cross-validation and bootstrap for accuracy estimation and model selection," *Proceedings the 14th International Joint Conference on Artificial Intelligenc*e, Vol. 2, 1995, pp. 1137-1143.

[57] Stengel, R. F., *Flight Dyanmics*. Princeton: Princeton University Press, 2004.

[58] Anderson, J. D., *Fundamentals of Aerodynamics*, McGraw-Hill Inc., New York, NY, 2005.

[59] Falkner, V. M., *The Accuracy of Calculations Based on Vortex Lattice Theory*, Technical Report, No. 9621, British Aeronautical Research Council, 1946.

[60] VN-100(T) Attitude and Heading Reference System User Manual, VectorNav Technologies, Richardson, TX, 2009.

[61] Shen, H., Xu, Y., Dickinson, T., "Micro Air Vehicle's Attitude Control Using Real-Time Pressure and Shear Information," *Journal of Aircraft*, Vol. 0, Issue 0, 2014, pp. 1-11.

[62] Xiang, Y., and Jin, J., "Hybrid Fault-Tolerant Flight Control System Design Against Partial Actuator Failures," *IEEE Transactions on Control Systems Technology*, Vol. 20, 2012, pp. 871-886.

[63] Eterno, J. S., Weiss, J. L., Looze, D. P., and Willsky, A., "Design Issues for Fault Tolerant-Restructurable Aircraft Control," IEEE Conference on Decision and Control, 1985, pp. 900-905.

[64] Cieslak, J., Henry, D., and Zolghadri, A., "Fault Tolerant Flight Control: From Theory to Piloted Flight Simulator Experiments," IET Control Theory & Applications, Vol. 4, 2010, pp. 1451-1461.

[65] Ioannou, P., and Fidan, B., *Adaptive Control Tutorial, Advances in Design and Control*, SIAM, PA, 2006.

[66] Khalil, H., *Nonlinear Systems (3rd Edition)*, Prentice Hall, 2001.

[67] Shen, H., Xu, Y., Remeikas, C., "Hardware Design and Validation of Pitching Control for Micro Air Vehicles Using Only Pressure Information," American Control Conference, Washington DC, 2013, pp. 5568-5573.